The Pennsylvania State University

The Graduate School

College of Engineering

A LANGMUIR PROBE INSTRUMENT

FOR RESEARCH IN THE TERRESTRIAL IONOSPHERE

A Thesis in

Electrical Engineering

by

Adam C. Escobar

Submitted in Partial Fulfillment
of the Requirements
for the Degree of

Master of Science

May 2009

The thesis of Adam C. Escobar was reviewed and approved* by the following:

Sven G. Bilén
Associate Professor of Engineering Design, Electrical Engineering, and Aerospace Engineering
Thesis Advisor

John D. Mitchell
Professor of Electrical Engineering

W. Kenneth Jenkins
Professor of Electrical Engineering
Head of the Department of Electrical Engineering

*Signatures are on file in the Graduate School

ABSTRACT

Langmuir probes have been used for plasma diagnostics on spacecraft ever since the first sounding rockets in the 1950s. As each decade passed, there have been improvements to the instrument design in order to obtain a more accurate solution to the plasma characteristics. In this thesis, a Langmuir probe instrument is designed and tested for use in the Earth's ionosphere. The design includes the probe and boom development, as well as the on-board electronics. The probe is cylindrical and sized using orbital-motion-limited theory. The on-board electronics include two electrometers, two calibration boards, a control and processing board, and a power regulation board. Raw data is sent to the on-board spacecraft computer, where the computer can process the data or send raw data down to the data downlink ground station. The instrument has the capability to clean the probe surface of contaminants, calibrate the electrometers, and operate in four different probe biasing modes.

TABLE OF CONTENTS

LIST OF FIGURES

LIST OF TABLES

ACKNOWLEDGMENTS

I first want to say thank you to my loving wife, Andrea, for supporting me in fulfilling my dreams. You are my princess, and I love you with all my heart. I would also like to acknowledge my parents, Ruben and Celia, for your continuing support throughout my life. I would not have been able to be the man I am today without your love and guidance. To my new in-laws, Ed and Betty, I am grateful to be a part of your family. Thank you for your kindness and support.

The Penn State faculty has helped make this instrument possible. Thank you, Tim Wheeler, for introducing me to the world of the space environment. Who would have thought when I came to you as a sophomore that I would further my education in this field? Professor Croskey, you are the one that initiated my designs for the Langmuir probe instrument six years ago, and encouraged me throughout the entire design process for ESPRIT. Professor Philbrick, thank you for instilling in me the roll of the "curious observer." From you, I have learned the different processes in the space environment. I will continue to pursue my quest for knowledge and aid the scientific community. Professor Mitchell, thank you for your help with the design of a Langmuir probe instrument and theory. Professor Urbina, thank you for your continuing assistance in my journey through my graduate education. Last but not least…to my advisor and good friend, Professor Sven Bilén, you have gone beyond the role of the advisor and helped me in all aspects of my academic career.

I would like to thank the Pennsylvania Space Grant Consortium for your financial support, and Dr. Paul Harris from Real Time Devices for providing some components for the instrument. To my former co-workers down at NASA Wallops Flight Facility, thank you for all your encouragement: Neil Shoemaker, Charlie Kupelian, Pat McPhail, Dave Jennings, Ron Kiefer, Jeff Benton, Dave Lang, Brian Tibbits, John Ozanne, Walt Costello, Terri Snyder, and Travis Murray. I have been blessed with so many people that have influenced my life, and I am so thankful of what God has given to me in order for me to place an imprint in the scientific community.

1 INTRODUCTION

Electrostatic probes have been utilized for over 90 years to measure plasma characteristics. These probes are called Langmuir probes due to the pioneering work done by Irving Langmuir in the 1920s. The basic theory of operation is to apply a voltage bias on a conductor immersed in a plasma. Depending on the voltage bias, a current develops and can be measured. Knowing the geometry of the conductor, the current response to the specific voltage bias, and plasma theory, several characteristics of the plasma can be determined: electron density, electron temperature, ion density, plasma potential, and floating potential. In order to obtain all of these parameters, the function describing the collected current with respect to the voltage bias is important. These parameters are described in greater detail in Chapter 2.

This chapter presents the general theory required for determining the plasma characteristics listed above, as well as the development of an instrument for spacecraft (i.e. sounding rockets and satellites) in order to monitor the Earth's ionosphere. The effort includes the development of the probe and on-board electronics. The end result is to provide a reference to the scientific community and an off-the-shelf instrument for use by The Pennsylvania State University's Communications and Space Sciences Laboratory (CSSL).

1.1 Overview

In order to design a Langmuir probe instrument for operation in the Earth's ionosphere, the thesis begins with a brief discussion about DC sheaths in plasma and the intricacies of the ionosphere to prepare the reader for the instrument development. With the general understanding of the processes involved in ionospheric plasma, Langmuir probe theory is applied to determine the necessary requirements of the instrument in order to determine the plasma characteristics: plasma potential, electron density, electron temperature, and ion density. The knowledge of the ranges for the plasma characteristics defines the probe design and electronics design.

For this thesis, the specific mission operations were defined in order for simulations of the ionospheric plasma to be properly developed. Three models from the International Reference Ionosphere (IRI), Mass Spectrometer Incoherent Scatter (MSIS), and International Geomagnetic Reference Field (IGRF) models generate the four simulations conducted. The simulations are: presheath/sheath thickness calculations, current collection, probe induced potential, and pressure profile. There are six mission operational modes, which include: probe clean, electrometer calibration, and four data collection modes. The simulations provide the high level requirements for the probe and electronics implementation. The probe was designed according to orbital-motion-limited (OML) theory, while taking into account the effects of the space environment. The probe design takes into account the photoelectric effect, surface patchiness, chemical interactions, electric field fringing, and the geomagnetic field. To support the functions of the probe, there are four electronic boards: the electrometer, the calibration board, the control and processing board, and the power regulation board. The electrometer converts the current collected by the probe to a voltage that is measured. The electrometer is calibrated by the calibration board, which relates the value of current at the input of the electrometer to the output of the electrometer and signal conditioning circuitry in the control and processing board. The control and processing board contains the signal conditioning circuitry and the processor that samples the analog data, provides the bias voltage for the probe, and communicates to both the

flight computer and ground support equipment. The final board is the power regulation board, which creates the necessary DC power supplies.

There have been three test plans developed in order to validate the proper operation of the instrument. The first test is to verify the functionality of each of the boards. These tests include all the processes necessary for the mission operations. The next test is environmental testing to determine if the instrument can perform in a vacuum with the densities and temperatures expected in the specific mission. The last test is to test the instrument in a laboratory based plasma. The characteristics of the plasma follow the parameters of the ionospheric plasma. The best method for testing is to fly the instrument on a spacecraft.

Practical design techniques are discussed that optimizes the capability of the instrument. These practical design techniques include low noise design, thermal considerations, and mechanical interfaces. There are also certain spacecraft constraints that are necessary in order for the instrument to function properly. In designing all the components, the ESPRIT sounding rocket mission provides a foundation for the development of this improved Langmuir probe instrument. ESPRIT was a Pennsylvania State University mission investigating the high latitude ionosphere, during a time when noctilucent clouds (NLCs), polar mesospheric summer echoes (PMSEs), and sporadic-*E* layers were present. ESPRIT launched successfully on July 1, 2006, from Andøya Rocket Range, and the Langmuir probe experiment results were presented at the 18th ESA symposium on European Rocket and Balloon Programmes and Related Research.

1.2 DC Sheaths

Plasma consists of free charged particles, namely electrons and ions. The ions can have a positive or negative charge, but there is more to plasma than just positively and negatively charged particles. Plasma as defined by Chen [2006] is a "quasi-neutral gas of charged and neutral particles which exhibits collective behavior." "Quasi-neutrality" is defined as the plasma medium having collectively neutral charge, where the density of electrons and negative ions is equal to the density of the positive ions, while electromagnetic forces influence the nature of this medium. This is where one property of plasma is defined: a plasma on average always remains charge neutral. The plasma investigated in the Earth's ionosphere is defined as a weakly ionized plasma, in which the plasma contains both charged and neutral particles. The charged species still have equal densities in order to remain charge neutral.

In order to develop the understanding of electrostatic probes, a brief description of DC sheaths is necessary. A probe biased to a certain potential generates an electric field, and the plasma interacts with this electric field by adjusting to "shield" this potential from the bulk plasma. If the probe was biased with a negative potential, then positive ions are attracted and shield the electric field from the bulk plasma; the opposite occurs with a positively biased probe, where electrons provide the shielding (see Figure 1.1). This shielding region is called the sheath, where charge neutrality does not exist.

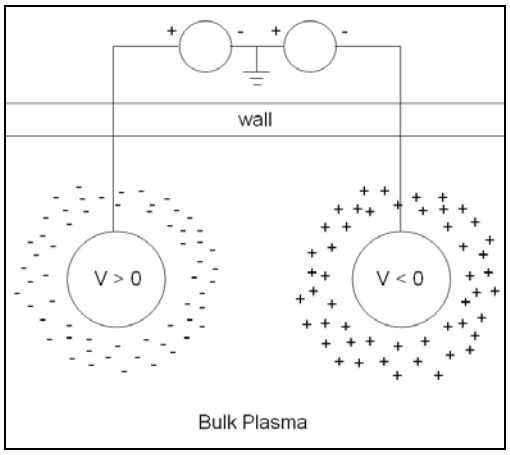

Figure 1.1 - Demonstrating the shielding characteristic of plasma.

There are actually two regions that define this shielding region: the sheath and presheath. Figure 1.2 depicts a qualitative view of a wall that is set at a negative potential relative to the plasma potential. The figure illustrates the plasma density and potential as a function of distance from the probe. The boundary between the two regions is defined as the distance where the potential is zero. To find the thickness of these regions, there are three assumptions required: (1) the plasma has a Maxwellian distribution, (2) the sheath region is collisionless, and (3) there are no external stimuli (e.g. magnetic field to cause drifts). The equation of motion (sum of forces) is used to describe the motion of particles (electrons or ions) in the plasma,

$$mn\left[\frac{\partial \vec{v}}{\partial t} + \vec{v}\cdot\nabla\vec{v}\right] = qn\left(\vec{E} + \vec{v}\times\vec{B}\right) - \nabla p - mn\upsilon\vec{v}\,, \qquad \textbf{EQ1- 1}$$

where m is the mass of the particle; n is the density of the specific species; $\vec{v}$ is the velocity vector; q is the elementary charge constant; $\vec{E}$ is the electric field; $\vec{B}$ is the magnetic field; ∇p is the pressure gradient; and the final term, $mn\upsilon\vec{v}$, is the collision term with υ as the collision frequency. The left side of the equation stems from Newton's second law and includes the mass and density multiplying a term called the convective derivative. The convective derivative provides the rate of change at a fixed point as well as the rate of change of velocity of the flow of plasma (this is also called the inertial term). The right side of the equation sums all the forces acting on the particles. The first term on the right is the Lorentz force; the second term is the pressure gradient, and the third term is a collisional term. Using this equation to calculate the sheath thickness, the assumptions will now be applied. For the right side, there is no magnetic field and no collisions, so those terms are eliminated. The left side of the equation can be approximated as zero since the acceleration is small with small potentials (there is an approximation noted later in the derivation), and the convective term is even smaller than the acceleration term; therefore, the equation simplifies to

$$0 = qn\vec{E} - \nabla p\,, \qquad \textbf{EQ1- 2}$$

where

$$\vec{E} = -\nabla\Phi$$

and the equation of state

$$\nabla p = kT\nabla n\,.$$

Dividing each term by the density of the specific species and integrating provides the Boltzmann relation

$$n = n_0 e^{\frac{q\Phi(r)}{kT}}. \qquad \textbf{EQ1- 3}$$

The negatively biased wall in Figure 1.2 is modeled to determine this sheath distance. Starting with Poisson's equation:

$$\nabla^2 \Phi = -\frac{\rho}{\varepsilon_0}, \qquad \textbf{EQ1- 4}$$

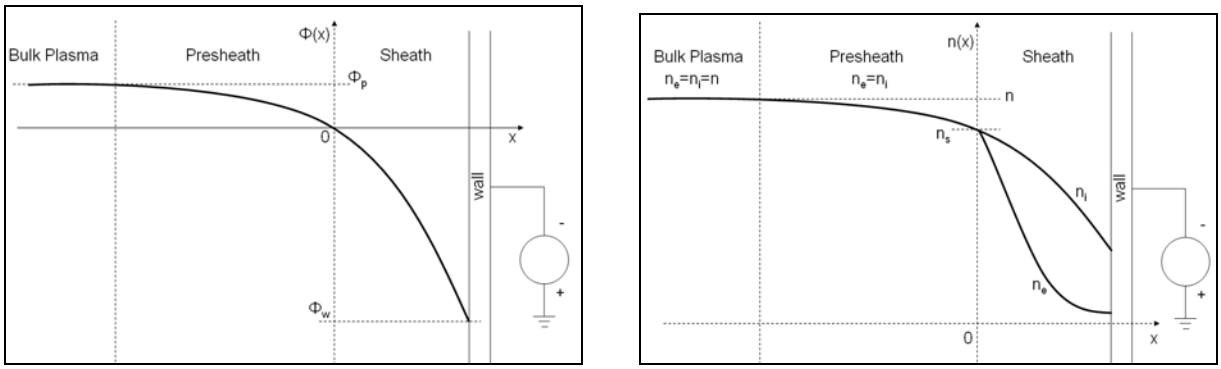

Figure 1.2 - Both figures display the sheath and presheath regions. a) Potential, $\Phi(x)$, is displayed as a function of distance with $x = 0$ at the presheath–sheath interface. b) Relative density, $n(x)$, due to Φ_w.

with charge density equaling

$$\rho = q\left(n_e - n_i\right). \qquad \textbf{EQ1- 5}$$

With the negative wall, there are fewer electrons in the sheath than ions; therefore, the Boltzmann relation is used for n_e and n_i is initially equal to the bulk density, $n_i = n_0$. The wall can assumed to be very large to approximate a one-dimensional system. With these relationships, Poisson's equation becomes

$$\frac{d^2\Phi}{dx^2} = \frac{qn_0}{\varepsilon_0}\left(e^{\frac{q\Phi}{kT}} - 1\right). \qquad \textbf{EQ1- 6}$$

A further assumption can be applied before solving this differential equation. If the exponential term is expanded in a Taylor series, i.e.,

$$\frac{d^2\Phi}{dx^2} = \frac{qn_0}{\varepsilon_0}\left[\frac{q\Phi}{kT_e} + \frac{1}{2}\left(\frac{q\Phi}{kT_e}\right)^2 + \cdots\right],$$

and it is assumed that the magnitude of the potential is much lower than the electron temperature (i.e., $\left|q\Phi / kT_e\right| << 1$), then the equation can be approximated as

$$\frac{d^2\Phi}{dx^2} = \frac{q^2 n_0}{kT_e}\Phi.$$

Solving this equation provides the following relationship,

$$\Phi(r) = \Phi_0 e^{-r\sqrt{\frac{qn_0}{\varepsilon_0 T_e}}}. \qquad \textbf{EQ1- 7}$$

Here r has been substituted for x and Φ_0 is the potential of the wall. This relationship also defines the Debye length of the plasma, which is the characteristic scale length in a plasma

$$\lambda_D = \sqrt{\frac{\varepsilon_o kT_e}{q^2 n_o}}. \qquad \textbf{EQ1- 8}$$

This measurement of the sheath thickness is not completely accurate, but provides a good approximation. To obtain the correct solution, the ion flux in the sheath region needs to be taken into account, and the Poisson equation cannot be linearized. Starting with the equation of energy conservation for ions:

$$\frac{1}{2} m_i u^2(x) = \frac{1}{2} m_i u_s^2 - q\Phi(x). \qquad \textbf{EQ1- 9}$$

The term on the left is the kinetic energy term, and the right side includes the initial kinetic energy term at the presheath–sheath boundary and the energy that comes from the wall potential. There is the continuity of ion flux to be taken into consideration as well. The ion flux does not change in the sheath providing the following relationship

$$n_i(x)u(x) = n_{is}u_s. \qquad \textbf{EQ1- 10}$$

With the continuity of ion flux substituted into the energy conservation equation, the ion density relationship is determined as

$$n_i = n_{is}\left(1 - \frac{2q\Phi}{m_i u_s^2}\right)^{-1/2}. \qquad \textbf{EQ1- 11}$$

The Boltzmann relation derived via ion

$$n = n_0 e^{\frac{q\Phi(r)}{kT}}. \qquad \textbf{EQ1- 3}$$

defines the density of the electrons, and using the Poisson equation once again, the nonlinear sheath potential equation can be written

$$\frac{d^2\Phi}{dx^2} = \frac{qn_s}{\varepsilon_0}\left[e^{\frac{q\Phi}{kT_e}} - \left(1 - \frac{2q\Phi}{m_i u_s^2}\right)^{-1/2}\right]. \qquad \textbf{EQ1- 12}$$

This expression is much more complex to solve. To simplify this further, each side is multiplied by $d\Phi/dx$ and integrated over x. This provides the following relationship,

$$\frac{1}{2}\left(\frac{d\Phi}{dx}\right)^2 = \frac{qn_s}{\varepsilon_o}\left[\frac{kT_e}{q}e^{\frac{q\Phi}{kT_e}} - \frac{kT_e}{q} + m_i u_s^2\left(1 - \frac{2q\Phi}{m_i u_s^2}\right)^{1/2} - m_i u_s^2\right]. \qquad \textbf{EQ1- 13}$$

In order to solve this equation for $\Phi(x)$, numerical integration techniques are necessary. This derivation was provided to show the reader the process for determining the exact potential in the sheath region. The linearized approximation is simple and can be used to approximate the thickness of the sheath and presheath; however, others have determined a simple relationship using numerical techniques that are more accurate. These sheath thicknesses solved by numerical simulations are mentioned in detail in Chapter 2.

1.3 The Earth's Ionosphere

1.3.1 Vertical Profile of the Atmosphere

Before defining the Earth's ionosphere, the different layers of the atmosphere are discussed. The atmosphere can be divided according to two different classifications: temperature or state of mixing. For divisions by temperature, there are four major divisions. Figure 1.3 outlines the temperature variations of the atmosphere. Starting from the Earth's

surface, there is a troposphere, where there is a lapse rate in temperature with respect to altitude. The lapse rate is [*Wallace and Hobbs*, 2006]

$$\Gamma = \frac{dT}{dz} \approx 6.5 \text{ °C}.$$

The temperature decreases until the tropopause, which is located about 10–17 km in altitude. The temperature at this height ranges from –40 °C to –80 °C depending on the location on the Earth. The temperature of the tropopause is much lower in the equatorial regions. Figure 1.4 illustrates the temperature variations according to latitude and altitude. After the tropopause, there is heating in a region called the stratosphere. The heating is due to the absorption of ultraviolet radiation from the sun by ozone. The temperature increases until the stratopause at about 50 km. Above the stratopause is the mesosphere, where the temperature decreases to the lowest in the atmosphere. The minimum temperature occurs at the mesopause at about 80 km to 85 km with a temperature of –90 °C to –110 °C. The thermosphere is the next layer, and here the temperature increases greatly due to solar radiation causing dissociation and ionization of the molecules in this region. This dissociation and ionization creates the ionosphere.

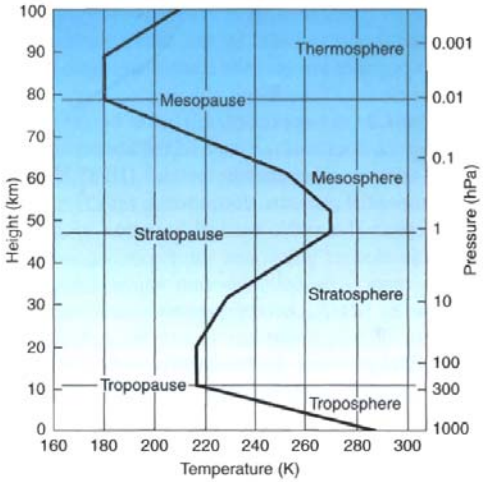

Figure 1.3 - Temperature profile of the atmosphere [*Wallace and Hobbs*, 2006].

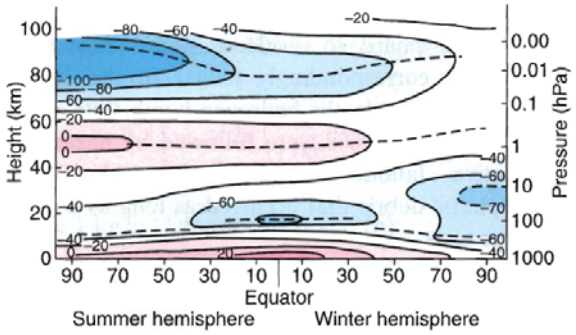

Figure 1.4 - Temperature variations during summer and winter [*Wallace and Hobbs*, 2006].

As mentioned previously, the second classification of the atmosphere is done by the state of mixing. The atmosphere is separated into two regions: the homosphere and the heterosphere. The homosphere, also called the turbosphere, is the lower region where the atmosphere is well

mixed. The upper region is called the heterosphere with the region between the two layers called the turbopause. The turbopause is located at approximately 100 km [*Hunsucker and Hargreaves*, 2003]. The heterosphere does not contain the same mixing due to the positive temperature gradient. Each type of gas is separated by composition relative to altitude (see Figure 1.5). Notice that the heavier molecules have greater densities at the lower altitudes, and at the higher altitudes hydrogen and helium dominate. The heterosphere defines some of the unique properties in the ionosphere.

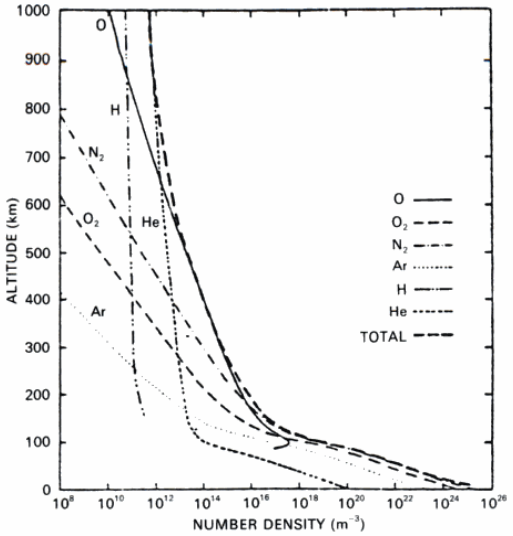

Figure 1.5 - Neutral atmosphere density [*Hunsucker and Hargreaves*, 2003].

1.3.2 Ionosphere Overview

The ionosphere is a region of the atmosphere composed of charged particles, mainly electrons and positive ions, that comprise a weakly ionized plasma. These charged particles are formed from two primary sources: the electromagnetic radiation from the Sun and the collision of energetic particles from the Sun with the neutral atmosphere. The particles continuously dissociate and recombine, going from being a neutral to a charged particle, and vice versa. The geomagnetic field controls the motions of these particles. There are drifts associated with the particles, where the geomagnetic field has a great effect.

On the global scale, the ionosphere can be divided into three regions according to geomagnetic latitude: equatorial, mid-latitudes, and high latitudes. In the equatorial region the magnetic field is roughly parallel to the ground. The distinctive features of the equatorial region ionosphere span ±20° latitude. The high latitude region is often referred to as the polar cap and auroral zone. The features of the processes in the high latitude ionosphere are primarily marked by the Arctic or Antarctic circles. The processes of the auroral region ionosphere are the most complex out of the three regions. The region in between the auroral and equatorial regions is the mid-latitude region, which is the most understood region of the ionosphere.

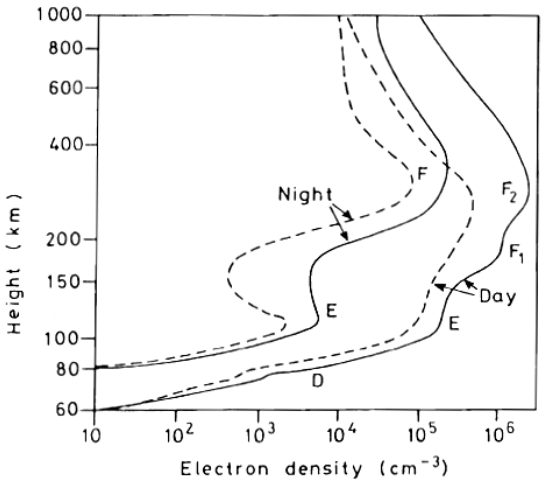

Figure 1.6 - Electron density profile of the ionosphere [*Hunsucker and Hargreaves*, 2003].

The typical ionospheric layers are classified by the vertical plasma density profile. There are three of these layers called the Chapman layers: *D*, *E*, and *F* regions (see Figure 1.6). The plasma density increases with height until the *F*-region; therefore, the *F*-region has the greatest plasma density. The total density and pressure, however, is higher at lower altitudes. For instance, 99.9% of the earth's atmosphere is below 50 km [*Wallace and Hobbs*, 2006]; this means that the *D*-region is the most dense and chemically complex of the ionospheric layers. Ionized particles are continuously colliding with each other and the surrounding neutrals.

1.3.3 Ionization in the Ionosphere

Before providing the explanation of each Chapman layer, the ionization process is explained first. As mentioned previously, there are two primary sources for ionization: electromagnetic radiation and energetic particle precipitation. The electromagnetic radiation ranges from X-ray to extreme ultra-violet (EUV) emissions. The X-ray emissions range from 0.1–17 nm (or 1–170 Å), and the EUV emissions range from 17–175 nm (or 170–1750 Å). Table 1.1 provides a list of gas molecule/atom specie found in the ionosphere with its associated ionization potential in eV. This energy is found using the following relationship:

$$E = hf = \frac{hc}{\lambda} \ [\mathrm{J}] = \frac{hc}{q\lambda} \ [\mathrm{eV}], \qquad \textbf{EQ1- 14}$$

where h is Planck's constant, c is the speed of light in a vacuum, q is elementary charge, and λ is the wavelength of the electromagnetic wave. The ionization potential in the table lists the minimum energy required for ionization with the associated maximum wavelength for ionization. Wavelengths smaller than the maximum wavelength are able to ionize the specific specie. In regards to the ionosphere profile, Mathews created a relationship between the penetration depth and wavelength in Figure 1.7. The primary molecules/atoms in the ionosphere are also listed on the graph indicating the maximum wavelength for ionization. The figure also displays the wavelengths responsible for ionization with respect to the associated Chapman layer.

Table 1.1 - Ionization Potentials for Different Atmospheric Gases [*Hunsucker and Hargreaves*, 2003]

Species	Ionization Potential [eV]	Maximum Wavelength [Å (nm)]
NO	9.25	1340 (134.0)
O_2	12.08	1027 (102.7)
H_2O	12.60	985 (98.5)
O_3	12.80	970 (97.0)
H	13.59	912 (91.2)
O	13.61	911 (91.1)
CO_2	13.79	899 (89.9)
N	14.54	853 (85.3)
H_2	15.41	804 (80.4)
N_2	15.58	796 (79.6)
He	24.58	504 (50.4)

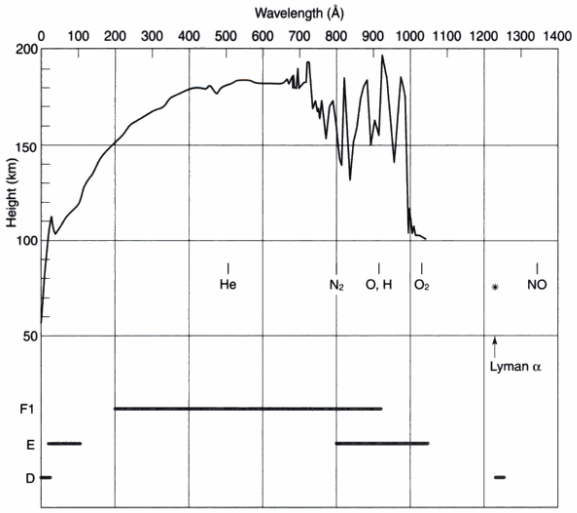

Figure 1.7 - Penetration depth for X-ray and EUV with relation to Chapman Layers [*Mathews*, private communication].

The second source of ionization is from energetic particles colliding with the earth's atmosphere. The equatorial and mid-latitudes are not affected greatly by these energetic particles. These particles flow along the magnetic field lines, since they are charged particles; therefore, the high latitude ionosphere is greatly influenced by these particles. During intense solar activity, there are times when the energetic particle precipitation is the main source of ionization. The primary particles involved are energetic electrons and protons (hydrogen ions, H^+). There are alpha particles and heavier particles emitted, but these particles amount to less than 6% of the solar wind (during solar maximum, however, there have been measurements of alpha particles composing of 20% of the solar wind) [*Hunsucker and Hargreaves*, 2003]. Figure 1.8 displays the penetration depths relative to production rate for ionization for energetic electrons and energetic protons respectively. Each figure has different energies plotted and, as expected, the higher the energy of the particle then the deeper the penetration.

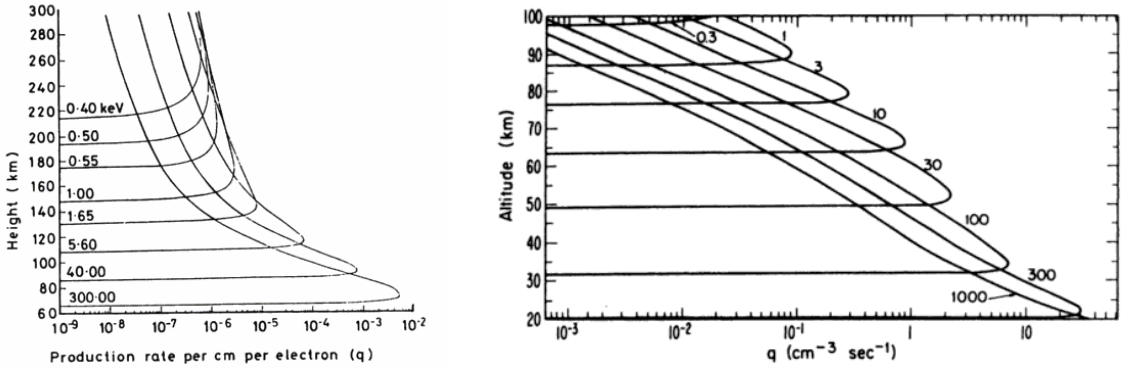

(a) **(b)**

Figure 1.8 - a) Penetration depth for energetic electrons. b) Penetration depth for energetic protons [*Hunsucker and Hargreaves*, 2003].

If the energetic electrons have a high enough energy, then when the electron collides with a neutral gas particle, a Bremsstrahlung X-ray is emitted. These X-rays can cause further ionization; however, the production rate is a few orders of magnitude less than the production rate coming directly from electron–neutral collisions (see Table 1.2). The Bremsstrahlung X-rays are able to penetrate deeper in the atmosphere though. Using Table 1.2, for an electron having energy of 100 keV, an X-ray is able to penetrate down to 37 km for maximum production. There have been high altitude balloon missions with X-ray detectors to detect the Bremsstrahlung X-ray emission at an altitude of 30–40 km.

Table 1.2 - Ionization by Energetic Particle Collisions and Bremsstrahlung X-rays [*Hunsucker and Hargreaves*, 2003].

Particle Energy [keV]	Height of Maximum Production [km]		Ionization Rate [ion pairs cm^{-3} per e^{-}]	
	Collisions	X-ray	Collisions	X-ray
3	126	88	2.5×10^{-5}	5.9×10^{-10}
10	108	70	1.4×10^{-4}	1.3×10^{-8}
30	94	48	5.6×10^{-4}	2.3×10^{-7}
100	84	37	1.9×10^{-3}	1.3×10^{-5}

1.3.4 The Chapman Layers

With the sources of ionization defined, the Chapman layers are now explained in detail. The lowest and most dense (total density) region of the ionosphere is the *D*-region. The *D*-region is usually only present during daytime hours; however, during enhanced ionization by energetic particles in the high latitude ionosphere, the *D*-region can be noticeable during the night. This region does not include a maximum, but is defined as a separate region from the *E*-region due to the different chemical processes associated in each region. The *D*-region spans the region of the ionosphere below 95 km. Nitrogen and oxygen provide the main source of ionized particles in this region. The three primary ions generated are nitric oxide ion (NO^+), molecular oxygen ion (O_2^+), and molecular nitrogen ion (N_2^+); however, the molecular nitrogen ions are usually converted to a molecular oxygen ion plus a neutral nitrogen molecule ($N_2^+ + O_2 \rightarrow O_2^+ + N_2$) creating NO^+ and O_2^+ as the dominant ion species. The negative charge in the *D*-region is composed not only of free electrons but also negative ions. At times these

negative ions can dominate the negative charge. The ionization in this region is generally due to X-ray and Lyman-α (1215 Å) emissions from the sun. Depending on the solar radiation activity, the X-ray component of ionization may be the major or minor ionization stimulus. The solar cycle affects ionization in all layers of the ionosphere, and explained in more detail in Section 1.2.5. Solar zenith angle is also another function of ionization for all regions of the ionosphere. *Friedrich et al.* [1992] plotted a relationship of *D*-region electron density profiles in Figure 1.9. With a higher zenith angle, the more ionization occurs. This provides seasonal variations, where the solar zenith angle is smaller in the summer and larger in the winter.

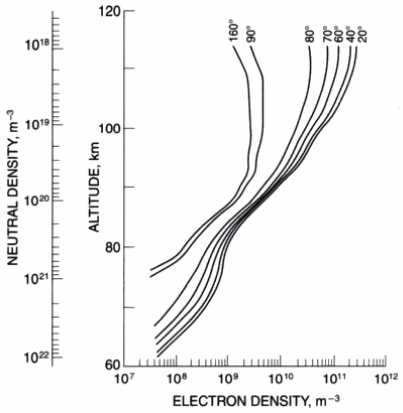

Figure 1.9 - Electron density profiles at different solar zenith angles [*Friedrich et al.*, 1992].

When one of these density enhancements takes place, radio wave absorption is a problem for communications. Since the *D*-region is more dense than the other Chapman layers, the collision frequency is higher, even though the plasma density is lower. This high collision frequency is the cause of the radio wave absorption. The free electrons oscillate in response to the radio wave, and then these oscillating electrons collide with the heavier particles (neutrals or ions). These collisions are where the power of the radio wave gets absorbed.

The *E*-region contains a peak between 105 and 110 km. The dominant ions are the same as the *D*-region (NO^+ and O_2^+); however, other ions are produced: molecular nitrogen ion (N_2^+) and atomic oxygen ion (O^+). The primary source of ionization in the EUV spectrum is between 800 and 1027 Å. During the nighttime, the *E*-region is still present, unlike the *D*-region. Sporadic-*E* is an anomaly that occurs in the *E*-region. Sporadic-*E* is an enhancement in ionization in the *E*-region. Sometimes this enhancement can be greater than the *F*-region peak. The generation of Sporadic-*E* differs at the different geomagnetic regions. In the equatorial and mid-latitude regions, the ionization enhancement for Sporadic-*E* is attributed to wind shear and meteor ionization. *Malhotra et al.* [2008] determined that the particles of Sporadic-*E* enhancements are due to meteors with data from Jicamarca Radio Observatory (JRO) dated August 10, 2006. In the high latitudes, Sporadic-*E* is attributed to ionization by energetic particles with energies for 1-10 keV [*Hunsucker and Hargreaves*, 2003]. Figure 1.10 displays this form of Sporadic-*E*. The data was taken during the Penn State ESPRIT sounding rocket mission on July 1, 2006, at 06:30 UTC from Andøya Rocket Range (ARR).

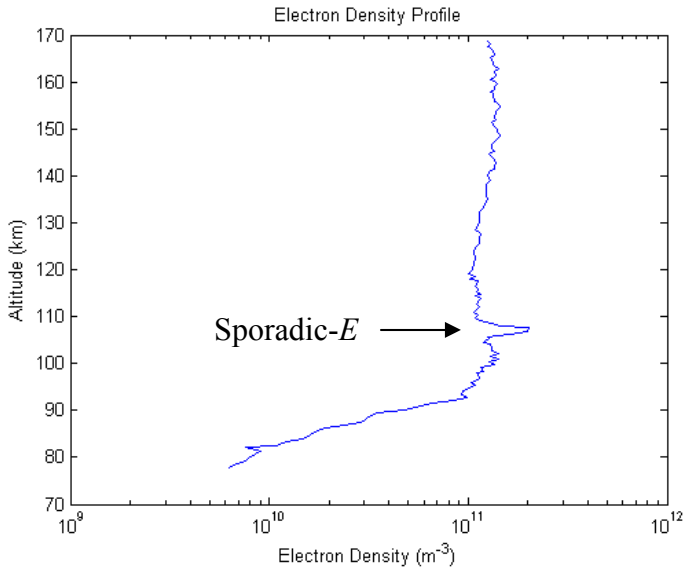

Figure 1.10 - Upleg electron density profile during the ESPRIT mission [*Escobar et al.*, 2007].

The *F*-region ionosphere consists of three layers: the *F*1, *F*2, and topside-*F* layers. The *F*1 region is ionized by the 200 to 900 Å spectrum, where NO^+ and O_2^+ are the dominant ions; however, other ions are produced: molecular nitrogen ion (N_2^+), atomic oxygen ion (O^+), atomic helium ion (He^+), and atomic nitrogen ion (N^+). The *F*1 peak is located between 160 and 180 km and is absent at night and sometimes during the daytime. The *F*1 layer is more pronounced during summer at solar minimum and not as much during winter and solar maximum. The *F*2 region peaks between 200 and 400 km. In this region the atomic oxygen ions (O^+) become dominant. The *F*2 layer is present at all hours of the day, but decreases in density at night. The plasma density for the topside *F*-region decreases with altitude. Eventually hydrogen and helium become dominant, and the predominant ion becomes hydrogen (H^+), which defines the protonosphere.

The *F*-region also contains several anomalies. In relation to the time of day, the density variation for the *F*-region is not symmetrical about noon as it is for the *E*-region. There are also seasonal variations, where the *F*-region peak is greater in the winter than the summer. Along with these variations, there are semi-annual variations where the density is larger during the equinoxes. Another interesting anomaly occurs every day in the *F*-region, where plasma irregularities form throughout this layer and sometimes down to the *E*-region. Large dense plasma "patches" and "blobs" form to create these irregularities. These irregularities are an issue for communications, where due to diffraction of the radio wave, the irregularities cause a phenomenon called scintillation. Scintillation includes variations in amplitude and phase of the propagating radio wave. Table 1.3 provides a summary of the composition for each Chapman layer.

Table 1.3 - Summary of the Chapman Layers [*Jursa*, 1985]

Chapman Layer	Typical Altitude Range [km]	Primary Constituents
D	70–95	NO^+, O_2^+
E	95–140	NO^+, O_2^+
F1	140–200	NO^+, O_2^+, O^+
F2	200–400	O^+, N^+
Topside *F*	> 400	O^+
Protonosphere	> 1200	H^+

1.3.5 Solar Cycle

Solar radiation affects the ionosphere greatly with a cycle of varying solar activity. The solar cycle has a period of about 11 years (see Figure 1.11). The increase of solar activity includes an increase in sunspot number, coronal mass ejections, and solar flares. The National Oceanic and Atmospheric Administration (NOAA) maintains an archive of previous solar cycles as well as predictions for the next solar cycle. Figure 1.11 displays this prediction for the next solar maximum. The increase in solar activity increases the plasma density and electron and ion temperatures. There are also diurnal variations with the daytime having more activity than the nighttime ionosphere; however, if there is energetic particle precipitation, especially during solar maximum, there is high activity even during the nighttime ionosphere. This enhancement in the ionosphere may cause several problems, such as radio blackouts.

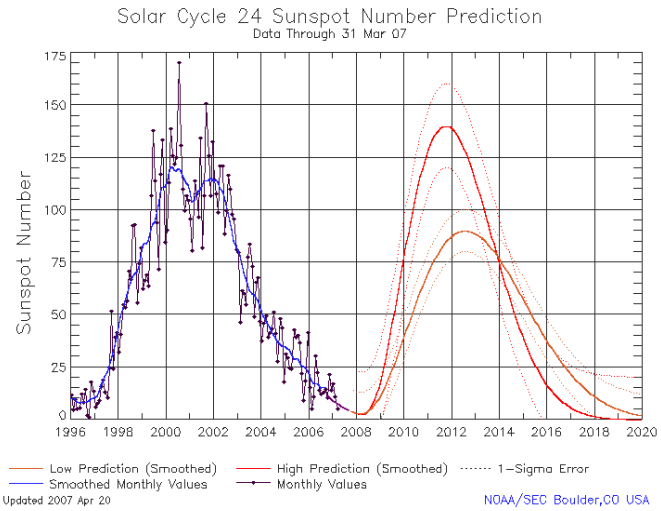

Figure 1.11 - Last solar cycle data and prediction for next cycle [*Space Weather Prediction Center*, 2009].

1.3.6 Ionosphere Models

There are computer-based models that provide information of the Earth's atmosphere and geomagnetic field. The ionosphere model discussed in this section is used for determining any plasma parameters in the subsequent sections. The International Reference Ionosphere (IRI) developed by *Bilitza* [2009] and the Mass Spectrometer Incoherent Scatter model (MSIS) developed by *Hedin* [2009] provide the atmospheric composition relative to altitude. The IRI version used is the IRI–2007, which provides electron density, electron and ion temperature, and percentage of positive ion composition. The MSIS model used is the MSIS–E–90, which provides the neutral atmosphere density composition and neutral temperature. For each model

the location of interest is State College, Pennsylvania, USA, (40.783 °N, 77.85 °W) and the date of June 21, 2002, at 12:00 local time (18:00 UTC). This year was the last solar maximum. Figure 1.12a displays the charged particle and Figure 1.12b displays the neutral densities, while Figure 1.12c displays the temperatures. The model utilized for the geomagnetic field is the International Geomagnetic Reference Field model (IGRF) version IGRF–10, which provides the magnetic field value as a function of altitude. The same location and time information was entered into the model to produce the output pictured in Figure 1.12d. These models provide a reference for calculating certain plasma parameters in this thesis. The relative values calculated and simulated later provide the reader with a reference for typical values found in practical applications.

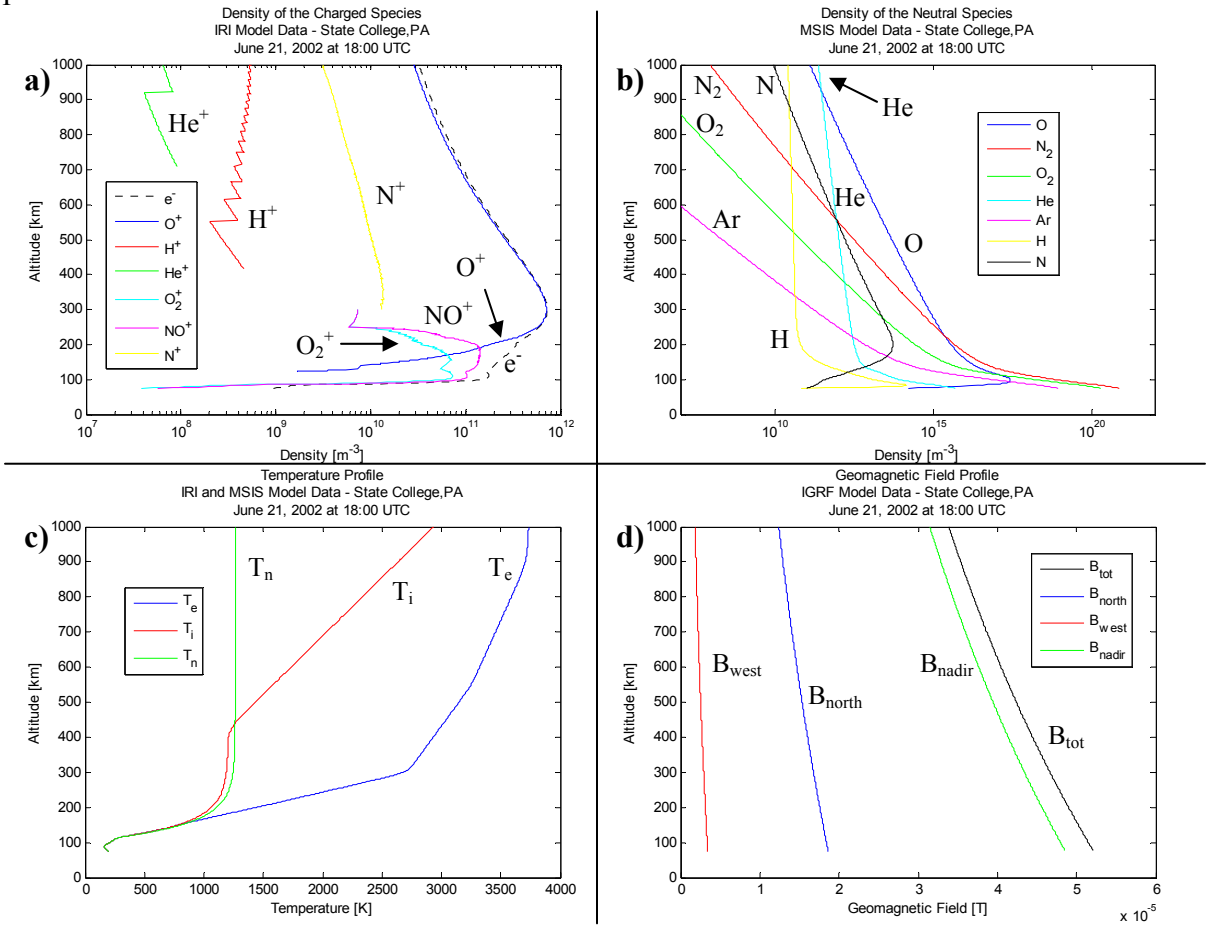

Figure 1.12 - Reference models utilized in this publication. All models are referenced at State College, PA, at 18:00 UTC. a) Charged particle densities from the IRI [*Balitza*, 2009]. b) Neutral particle density from MSIS [*Hedin*, 2009]. c) Particle temperatures from IRI and MSIS. d) Geomagnetic field model from IGRF [*Macmillan*, 2009].

2 LANGMUIR PROBE THEORY

The two most prevalent methods for determining the plasma characteristics are orbital-motion-limited (OML) theory and the Child–Langmuir law of space-charge-limited current in a plane diode. The difference between the two theories is the result of the different probe geometries. For OML, the probe radius must be less than the Debye length of the plasma ($r << \lambda_D$). The opposite is the case for the Child–Langmuir law, where the probe radius must be greater than the Debye length ($r >> \lambda_D$). For the derivations of current relationship, the probe geometry is taken to be a cylinder. The reason for choosing the cylindrical geometry is stated in the probe design section in Chapter 4.

2.1 Orbital-Motion-Limited Theory

For OML theory, the probe radius is smaller than the Debye length, λ_{De}. The Debye length is given in **EQ1-8**. Mott–Smith and Langmuir formulated this theory in 1926. Figure 2.1 depicts a particle trajectory to the probe. The sheath distance is given by *a*, and the probe radius is given by *r*. The sheath thickness, $a - r$, is shown to be larger than the probe radius. This is the limiting factor to utilize OML theory.

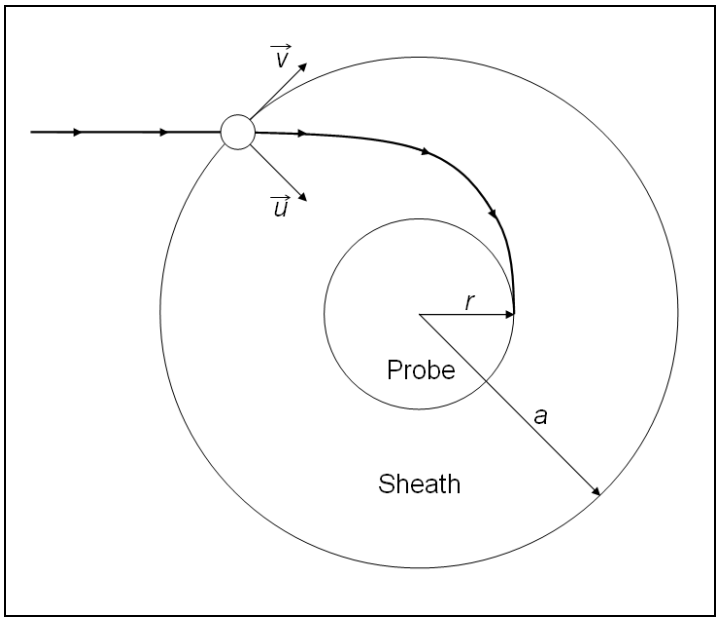

Figure 2.1 - Particle trajectory for orbital-motion-limited theory.

2.1.1 Plasma Parameters

Figure 2.2 provides the *I–V* relationship displaying three regions of operation and two notable potentials. The plasma potential, Φ_p, is located at the inflection point of the curve, where the probe voltage is the same as the plasma potential. For bias potentials greater than the plasma potential ($V_{\text{probe}} > \Phi_p$), the current eventually saturates to collect only electrons or negative ions. This region is called the electron saturation region. In the electron saturation region, the electron density, n_e, of the plasma is able to be calculated.

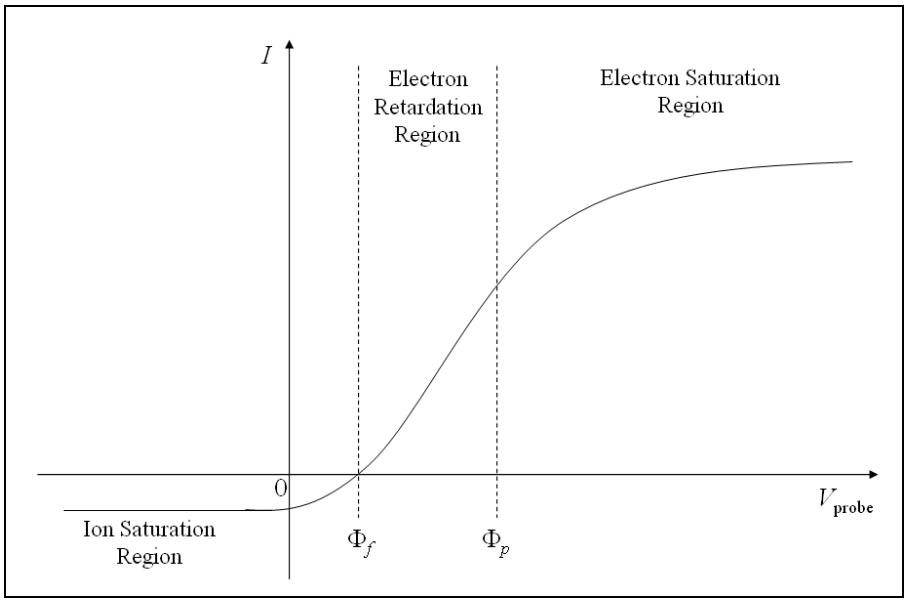

Figure 2.2 - The current to voltage relationship.

For potentials that are less than the plasma potential ($V_{probe} < \Phi_p$), electrons are repelled according to the Boltzmann relation (See **EQ1-3**). Current collection from electrons in this region is due to thermal motion. When the current of the electrons equals the current of the positive ions, then the net current is zero ($I = 0$), and this bias potential is called the floating potential, Φ_f. This region is called the electron retardation region, where the electron temperature, T_e, can be determined.

When the bias potential is less than the floating potential ($V_{probe} < \Phi_f$), there are no electrons collected, and only positive ions provide the current. As the probe bias is driven more negative, the positive ion current eventually saturates, and this region on the *I–V* curve is called the ion saturation region, where the positive ion current is found to determine the positive ion density, n_i.

2.1.2 Current Collection Relationships

From Mott–Smith and Langmuir (1926), the generalized current relationship as a function of the distribution function is

$$I = nq\int_0^\infty \int_{-\infty}^\infty uf(u,v)dvdu\,, \qquad \textbf{EQ2- 1}$$

where u and v are the radial and tangential components of velocity (See Figure 2.1). Assuming that there is a Maxwellian distribution for the particle velocities, the distribution function is given as

$$f(u,v) = n\left(\frac{m}{2\pi kT}\right)^{3/2} e^{\frac{-m\left(u^2+v^2\right)}{2kT}}. \qquad \textbf{EQ2- 2}$$

An expression for the current in the electron saturation region, I_e, is solved first. For the cylindrical probe, the end effects of the electric field can be neglected for this calculation. The design of the probe has this taken into account (see Chapter 4). Mott–Smith and Langmuir (1926) continued this derivation, to eventually come to the following solution,

$$I_e = 2\pi rlI\frac{2}{\sqrt{\pi}}\sqrt{1+\eta}\,, \qquad \textbf{EQ2- 3}$$

where

$$I = nq\sqrt{\frac{kT}{2\pi m}} \qquad \textbf{EQ2- 4}$$

and

$$\eta = \frac{qV}{kT}. \qquad \textbf{EQ2- 5}$$

I is the current due to the thermal motion of the electrons, and η is the term that defines the current due to the potential, where the potential, V, is respect to the plasma potential, Φ_p. Note that this expression is for a bias potential that is greater than the plasma potential to approximate the current in the electron saturation region of the *I–V* curve. To simplify this current to an expression that can be used to find the electron density, n_e, the surface area of the probe, A, is defined as $A = 2\pi rl$, hence

$$I_e = An_e q\frac{2}{\sqrt{\pi}}\sqrt{\frac{kT_e}{2\pi m_e}}\sqrt{1+\frac{qV}{kT_e}}. \qquad \textbf{EQ2- 6}$$

Since the current relationship is in the electron saturation region, it can be assumed further that $qV >> kT_e$. With this relationship, the electron density, n_e, is determined without knowledge of the electron temperature, T_e, i.e.,

$$I_e = An_e q\frac{2}{\sqrt{\pi}}\sqrt{\frac{qV}{2\pi m_e}}\,, \qquad \textbf{EQ2- 7}$$

and finally,

$$n_e = \frac{\pi I_e}{Aq}\sqrt{\frac{m_e}{2qV}} \qquad [\mathrm{m}^{-3}] \qquad \textbf{EQ2- 8}$$

Finding the current relationship in the electron retardation region determines the electron temperature, T_e. Using the generalized current definition in **EQ1-2**, the limits for integration differ from the derivation for the electron retardation region, where the current is due to only the thermal motion of the electrons. The current relationship in the electron retardation region is

$$I_e = Aqn_e\sqrt{\frac{kT_e}{2\pi m_e}}e^{\frac{qV}{kT_e}}. \qquad \textbf{EQ2- 9}$$

Taking the natural logarithm and differentiating with respect to the probe voltage, V_{probe}, gives

$$T_e = \frac{q}{k}\cdot\frac{1}{\frac{d}{dV_{\mathrm{probe}}}\left[\ln\left(I_e\left(V_{\mathrm{probe}}\right)\right)\right]} \qquad [\mathrm{K}]. \qquad \textbf{EQ2- 10}$$

Before applying this equation to the *I–V* curve, two truncations of the data are applied: 1) all values below the floating potential, Φ_f, (negative current values removed) and 2) all values above the plasma potential, Φ_p. With this data removed, the electron temperature is able to be found. Closer inspection to this expression shows that this is just the inverse of the slope of the line, and a simpler expression for T_e can be found, i.e.,

$$T_e = \frac{q}{k} \cdot \frac{V_2 - V_1}{\ln(I_2) - \ln(I_1)} \qquad [\mathrm{K}] \qquad \textbf{EQ2- 11}$$

where (I_2, V_2) and (I_1, V_1) are two points on the *I–V* curve that is in the electron retardation region.

Langmuir theory alone cannot be used to find the positive ion density, because the thermal ion velocity is comparable to the spacecraft velocity. Therefore, *Hoegy and Wharton* [1973] developed a relationship to include the spacecraft velocity with the probe axis perpendicular to the velocity vector,

$$I_i = Aqn_i v_i \frac{1}{\sqrt{\pi}} \sqrt{1 + \frac{kT_i}{m_i v_i^2} + \frac{2qV}{m_i v_i^2}}, \qquad \textbf{EQ2- 12}$$

hence

$$n_i = \frac{\pi I_i}{qA} \sqrt{\frac{m_i}{m_i v_i^2 + kT_i + 2qV}}, \qquad \textbf{EQ2- 13}$$

where n_i is the positive ion density, v_i is the ion velocity with respect to the spacecraft, and T_i is the ion temperature. There are three components that sum up the entire positive ion collection current: spacecraft velocity, ion thermal motion, and probe potential. Again, there are a few assumptions that can be made to simplify the ion collection current expression. Given a Maxwellian distribution of velocities, most of the current generated from this expression is going to be from the spacecraft velocity term; therefore, an assumption can be made that $v_i \approx v_{\text{spacecraft}}$. The ion temperature, T_i, can be set equal to the electron temperature, T_e, for only low altitudes of the ionosphere. Other substitutions for the ion temperature should come from an outside source. The final approximation is for the ion mass, m_i. The ion mass value is the average of the dominant species of ions in the specific region of the ionosphere. These dominant species can be found via a number of methods: on-board mass spectrometer, ionosphere models (e.g. International Reference Ionosphere, IRI), ground based instrumentation, or (for a rough estimate) the dominant species for each region can be utilized.

2.2 Sheath Thickness

An approximation for the sheath thickness was derived in Chapter 1; however, this thickness was derived assuming an infinite wall driven to a negative potential. When an exact closed form solution was to be determined, a complex integral solution was found that can only be solved through numerical techniques. The Child–Langmuir Law (1913) provides a simple expression for the sheath thickness, but requires certain assumptions. These assumptions have limited the use of this theory; however, the sheath thickness found here provides a good approximation. The six assumptions include:

1. Ions are assumed to be cold, $T_i \sim 0$
2. The sheath is collisionless
3. $kT_e < qV$
4. $E = 0$ at the sheath edge
5. No electrons in sheath region
6. Quasi-neutrality in presheath

Applying these assumptions provide the following expression for sheath thickness,

$$s = \frac{\sqrt{2}}{3}\left(\frac{2qV}{kT_e}\right)^{3/4}. \qquad \textbf{EQ2- 14}$$

Because of these limitations, the sheath thickness is not as accurate. As mentioned in Chapter 1, numerical integration is required to solve the complex differential equation. *Wang and Wendt* [1999] developed a computer program to develop a solution for a more accurate sheath thickness. The expression utilized in **EQ1-13** is similar to the approximation in the following

$$\frac{d\Phi}{dx} \approx \frac{kT_e}{q}\left[2\left(1-0.73\left(\frac{\lambda_D}{\lambda}\right)^{4/3}\right)\left(e^{\frac{qV}{kT_e}}-1\right)+2\left(1-2\frac{qV}{kT_e}\right)^{1/2}-2+\left(1.2\left(\frac{\lambda_D}{\lambda}\right)^{7/10}+0.018\right)^2\right]^{1/2} \qquad \textbf{EQ2- 15}$$

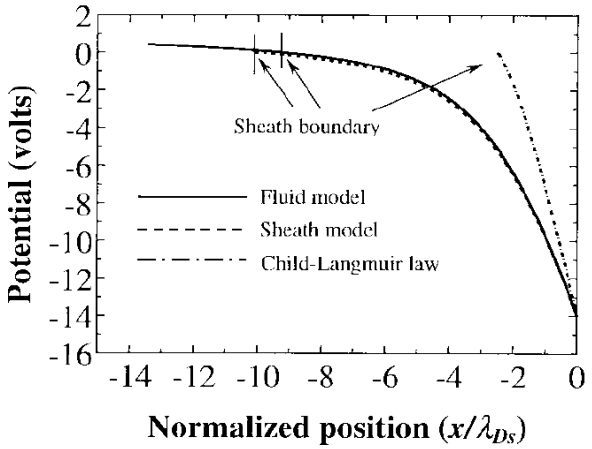

Figure 2.3 - Comparison of sheath thickness of a computer model developed by Wang and Wendt and the Child–Langmuir Law [*Wang and Wendt*, 1999].

The sheath thickness found by this expression still requires numerical integration. Figure 2.3 displays the difference of the sheath thickness found by the expression above and the Child–Langmuir Law. The sheath thickness found by the above expression is slightly larger than the thickness found by the Child–Langmuir Law. This new relationship can be applied to collisionless and weakly collisional sheaths; however, this expression still does not offer a simple relationship to determine an approximate value for the sheath thickness. Other researchers have found other solutions using numerical techniques, such as *Benilov* [2003]. For a simpler, more accurate calculation of the sheath thickness, *Bettinger and Walker* [1965] determined a relationship using computer calculations for the radius of the sheath around a cylindrical probe. *Bettinger and Walker* developed two expressions for the cylindrical probe sheath thickness dependent on the ratio between sheath thickness, *s*, and probe radius, *r*; however, their conclusion was that only one solution is necessary for the different ratios i.e.,

$$a = 1.66\lambda_D\left(\frac{qV}{kT_e}\right)^{3/4} + r. \qquad \textbf{EQ2- 16}$$

This relationship contains the same proportional relationship as in the Child–Langmuir Law, $a - r \propto \left(qV/(kT_e)\right)^{3/4}$; however, the multiplying coefficient differs. A closer look at the assumption made by *Bettinger and Walker* shows that the approximation to utilize **EQ2-16** for both cases does not satisfy all OML cases. This equation was actually derived for cases with the

probe radius larger than the sheath thickness, $r > s$. Deriving from the charge conservation in the sheath, for the sheath thickness greater than the probe radius, $s > r$, the approximated sheath thickness is

$$s_0 = \sqrt{\frac{\pi\sqrt{2/3}}{\ln(s_o/\rho)}}\Psi_s^{3/4}, \qquad \textbf{EQ2- 17}$$

where s_0 is the normalized sheath thickness with respect to the Debye length, i.e.,

$$s_0 = \frac{s}{\lambda_D} = \frac{a-r}{\lambda_D}. \qquad \textbf{EQ2- 18}$$

ρ is the normalized probe radius to the Debye length, i.e.,

$$\rho = \frac{r}{\lambda_D}. \qquad \textbf{EQ2- 19}$$

Ψ_s is the normalized probe voltage (with respect to the plasma potential, Φ_p) to the electron thermal energy

$$\Psi_s = \frac{qV}{kT_e}. \qquad \textbf{EQ2- 20}$$

This expression has an additional factor of $\ln(s_0/\rho)$. *Bettinger and Walker* made the assumption that this expression does not affect the sheath thickness for any probe radius, but in fact it does. A simpler expression was derived for a cylindrical probe with a radius larger than the Debye length, and this is what *Bettinger and Walker* stated to be used for all cases of radii; however, by way of simulation, these two equations produced great differences in approximating the sheath thickness.

In the simulations, there is no specific solution for the sheath thickness expression in **EQ2-17**. The sheath thickness has to be solved with recursive iterations in a computer program. This has been done with the following assumptions:

1. Voltage is greater than electron thermal energy, $qV > kT_e$
2. Voltage is set to $V = 1$ V
3. Probe radius is $r = 1/16$ in. $= 0.0015875$ m
4. Electron temperature, T_e, is from the model of the ionosphere
5. Debye length, λ_D, is calculated from the model of the ionosphere

Figure 2.4 plots the three different sheath thicknesses, comparing the Child–Langmuir law sheath and the two sheath thickness expressions developed by *Bettinger and Walker*. Notice that the Child–Langmuir law sheath thicknesses are smaller than the other two, except in the *D*-region ionosphere. The *Bettinger and Walker* equation for $r > s$ has a sheath thickness much greater than the other two calculated. All calculated sheath thicknesses are greatest in the *D*-region and smallest in the *F*-region. The reason for these extremes is primarily due to the Debye length. The electron temperature term in the normalized probe voltage term also contributes a factor to the large sheath thickness in the *D*-region, because the temperature is very low at the Mesopause, where the temperature is the coldest. The Debye length is also larger in the *D*-region, because the electron density is at the lowest in this region. The Debye length is very small for the *F*-region, and this is the reason for the smaller sheath thickness. This is due to the higher electron densities in this region. Figure 2.4b displays the entire sheath thickness range. Note that the Child–Langmuir law sheath is less than the Bettinger and Walker sheath with $s > r$ everywhere

except in the *D*-region. The Bettinger and Walker sheath with $s > r$ provides an improved and simple sheath thickness calculation, and this approximation is used for the sheath calculations for

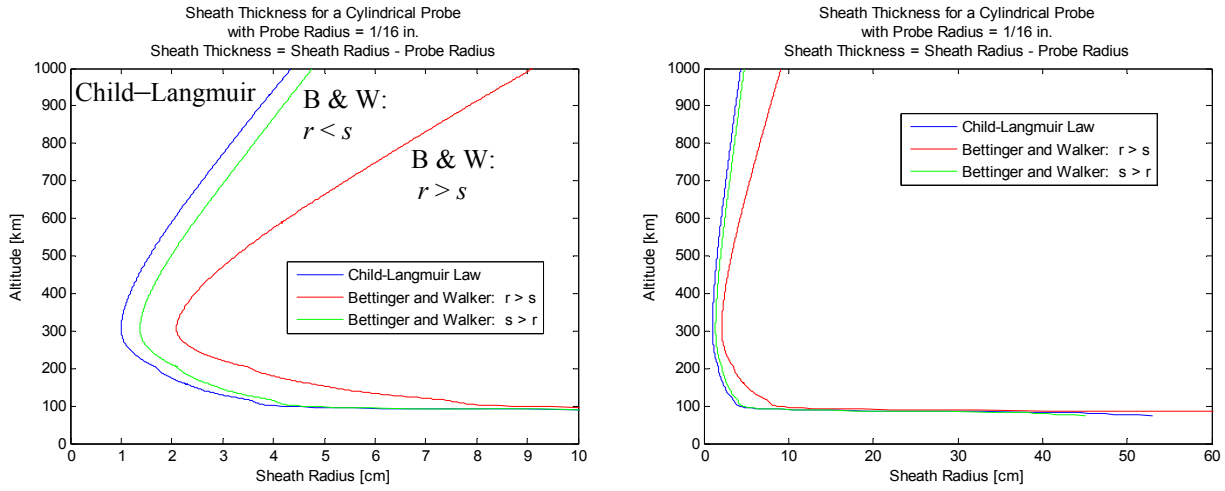

Figure 2.4 - Calculations of the sheath thickness using the Child-Langmuir law and two expressions from *Bettinger and Walker* [1965]. The probe is biased +1 V with respect to the plasma potential for these simulations. a) Closer view of the smaller values of sheath thicknesses, s < 10 cm. b) Entire range of sheath thicknesses.

the requirements in the design of the instrument. With this stated, the maximum sheath thickness in the *D*-region is at 17.7 in. (45 cm), and the minimum in the *F*-region is at 0.6 in. (1.5 cm). The sheath thickness increases in the topside *F*-region due to the decrease in electron density. At 1000 km in altitude, the sheath thickness increases to 1.9 in. (4.75 cm). From these results, the sheath thickness for the lower altitudes of the ionosphere may be incorrect, because of the high neutral density in this region. This high density gives a higher collision frequency; therefore, particle collisions in the sheath region should affect the sheath thickness. From the work from *Wang and Wendt* [1999], a weakly collisional sheath has a larger sheath thickness than that provided by the collisionless sheath of the Child–Langmuir law. Assuming this is the case, the sheath thickness in the *D*-region ionosphere is larger than the calculations presented in Figure 2.4. The opposite is true for the other regions of the ionosphere, where the collision frequency is less; therefore, the sheath thicknesses found for these regions are a good approximation.

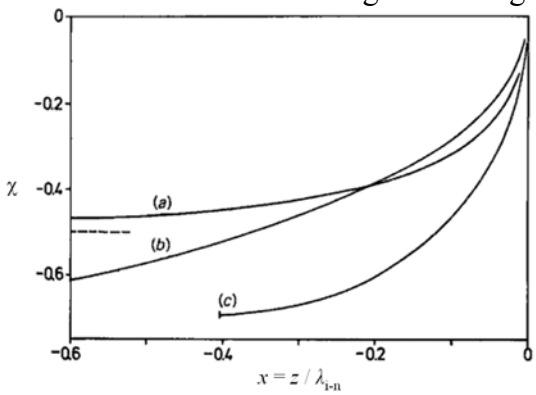

Figure 2.5 - Qualitative view for the three different kinds of presheaths. a) Spherical collisionless presheath. b) Planar collisional presheath. c) Planar ionization presheath. [*Riemmann*, 1991]

The previous sheath calculations do not take into account the presheath region. *Riemann* [1991] developed several relationships for the presheath approximation. The three approximations are for 1) a collisionless geometric presheath, 2) a collisional presheath, and 3) an ionizing presheath. Figure 2.5 displays a qualitative relationship between these three types of sheaths. Two types of sheaths are derived with both having a cylindrical geometry: 1) a presheath with collisions and 2) a presheath with no collisions. The reason for these two derivations is to utilize the expression using collisions for the lower ionosphere with the high collision frequency. The collisionless presheath is derived for use in the other parts of the ionosphere, where the collision frequency is very small. The relationships are found through the following system of differential equations

$$\begin{cases} \frac{1}{2y}\frac{dy}{dx} - \frac{d\chi}{dx} = \frac{\sigma}{j_i} - \frac{1}{A(x)}\frac{d}{dx}A(x) \\ \frac{dy}{dx} - \frac{d\chi}{dx} = -2y\left(q + \frac{\sigma}{j_i}\right) \end{cases}, \qquad \textbf{EQ2- 21}$$

where x is the distance from the sheath–presheath boundary; y is the normalized kinetic energy to the electron thermal energy,

$$y = \frac{m_i v^2}{2kT_e}, \qquad \textbf{EQ2- 22}$$

χ is the normalized potential energy to the electron thermal energy, and this is slightly different from before, because of a negative sign,

$$\chi = -\frac{qV}{kT_e}, \qquad \textbf{EQ2- 23}$$

σ / j_i is an ionization term, and $A(x)$ is the geometry term for the probe,

$$A(x) = (1-x)^{\beta}, \qquad \textbf{EQ2- 24}$$

where β is 0 for a planar surface, 1 for a cylinder, and 2 for a sphere. x is normalized to the ion–neutral mean free path, and z is the physical distance,

$$x = \frac{z}{\lambda_{i-n}}. \qquad \textbf{EQ2- 25}$$

The mean free path can be calculated from $\lambda = 1/(n_n\sigma)$, where n_n is the neutral density and σ is the hard sphere cross section. Solving the system of equations with collisions and cylindrical probe geometry yields

$$x = \frac{z}{\lambda_{i-n}} = 1 - e^{2\chi}(1+2\chi)^{-1/2}. \qquad \textbf{EQ2- 26}$$

For the second case with no collisions, the expression is

$$x = \frac{z}{\lambda_{i-n}} = 1 - e^{-\chi}(1+2\chi)^{1/2}. \qquad \textbf{EQ2- 27}$$

2.3 Child–Langmuir Law

The Child-Langmuir Law is utilized for probes that are said to be "space charge limited", where the probe radius is larger than the Debye length. This section is kept brief, because the instrument developed utilizes the OML theory. This section explains the generalized current collection. In the sheath, the allowable particle trajectories are shorter than the trajectories for OML. As before, the sheath radius is a, and the probe radius is r, except for this case, $a - r$ is smaller than the probe radius.

Using the assumptions mentioned in the previous section, an expression for the current collected is able to be found. *Child and Langmuir* [1913] found this current relationship, but *Langmuir and Blodgett* [1923] expanded this solution to find the relationship for a cylindrical probe, i.e.,

$$I_a = \frac{2\sqrt{2}}{9}\sqrt{\frac{q}{m}}\frac{V^{3/2}}{a\beta^2}. \qquad \textbf{EQ2- 28}$$

This expression relates current per unit length along the radial axis. To obtain the total current,

$$I = \frac{\sqrt{2}}{9\pi}\sqrt{\frac{q}{m}}\frac{V^{3/2}}{ar\beta^2} \qquad \textbf{EQ2- 29}$$

is used, where r is the radius of the probe and a is the sheath radius. β is a function of the two radii, $\beta = f(a/r)$ and is a series that is solved for different ratios in the 1923 publication. In summary, to utilize this current relationship, the sheath thickness should also be kept small, where $a/r > 1$, and as mentioned previously, the probe radius should be greater than the Debye length, $r > \lambda_D$.

3 OPERATIONAL MODES

With an understanding of the ionosphere plasma environment and Langmuir theory, the Langmuir probe instrument can be designed. Before designing any hardware, the instrument requirements need to be formulated. The high level requirements for this instrument are to determine the parameters listed in Section 2.1.1. From these requirements, the operational modes are determined, which this chapter explains.

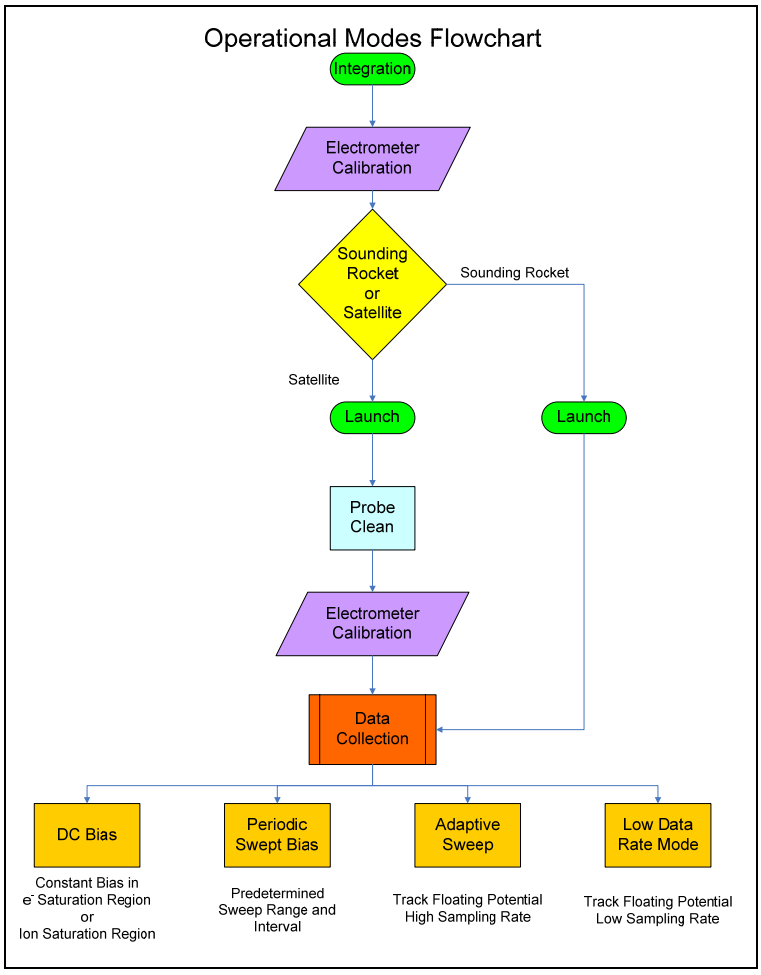

Figure 3.1 - Operational Modes Diagram.

There are six different modes of operation for the instrument. Figure 3.1 displays an operational modes diagram for a typical mission. Table 3.1 displays the operational modes in a table format. After boom deployment, instrument mission operations begin. The first operational mode is the probe clean mode, where a high voltage bias attracts particles to bombard the surface of the probe, thus removing any contaminants. This mode, of course, is not used on sounding rocket missions due to the short mission time. The second operational mode is the electrometer calibration mode, where the electrometer(s) are calibrated to reference Victoreen resistors. This mode provides the reference for input-current-to-output-voltage relationship. The third operational mode is the data collection mode, where there are four different operations depending on mission requirements. The four operational modes are: 1) DC

bias, 2) periodic swept bias, 3) adaptive swept bias modes, and 4) low data rate mode. Each mode is utilized for a specific mission operation.

Table 3.1 - Operational Modes Table

Index	Operational Mode
1	Probe Clean
2	Electrometer Calibration
3	DC Bias
4	Periodic Swept Bias
5	Adaptive Swept Bias
6	Low Data Rate Mode

*This is for a 28 V input into the power board

3.1 Probe Clean

The probe clean mode is necessary because contaminates may be present on the probe surface impeding the collection of the expected current. This contamination may be due to the integration phase, launch phase, or on-orbit outgassing. Recent articles on probe contamination point toward water as the primary contaminant during the integration or launch phase [*Piel*, 2001]. *Piel et al.* [2001] modeled the contamination as a layer that provides a resistance and capacitance to the bulk plasma (See Figure 3.2). This contamination affects false readings of the *I–V* relationship, everywhere except the ion saturation region. Figure 3.3 displays the difference in the curves of a probe with no contamination and two with contamination. There are two curves for contamination, because the bias voltage swept with a positive slope with respect to time called the upramp, and then swept with a negative slope called the downramp. Notice in the electron retardation region that the upleg swept data follows the uncontaminated probe closely, while the downramp is far from this value. This is due to the time constant generated by the RC equivalent contaminant.

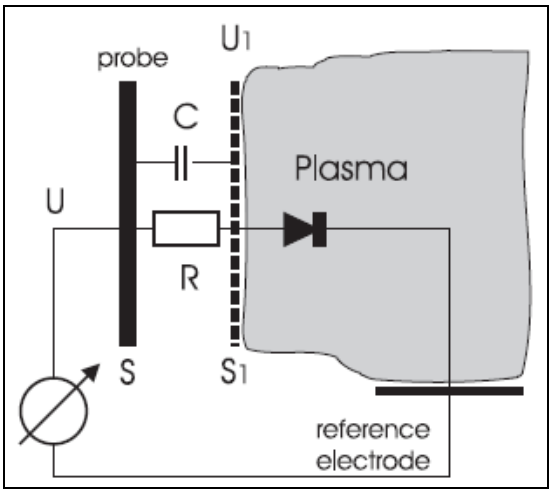

Figure 3.2 - Simulation of contaminant on probe surface [*Piel et al.*, 2001].

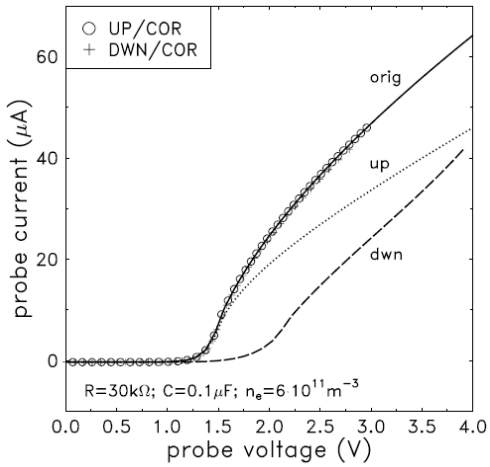

Figure 3.3 - Clean probe data labeled "orig" and two data sets with probe contamination. "up" labels the upramp bias, and "dwn" labels the downramp bias [*Piel et al.*, 2001].

There have been two known methods to remove this contaminant layer. The first method is to "bake" the probe, meaning heat it up to high temperatures, which removes the contaminant layer. The probe would have to be heated to temperatures greater than 300 °C. The first probe-clean designs included a single filament within the probe that heated the probe to high temperatures. Figure 3.4 displays electron temperature data with respect to probe temperature [*Amatucci*, 1993]. The ideal electron temperature is marked by the dashed line. As temperature of the probe is increased to 300 °C, the data converges to the ideal electron temperature. The problem with this method is the high power required to implement the bake-out. Figure 3.5 shows that in order to heat the probe to 300 °C or higher, the power required has to be 7.5 W or greater. *Amatucci et al.* [1993] developed a probe design that utilizes only 2.5 W of power, improving upon the thermal conduction of the filament in order to improve the heat efficiency (see Figure 3.6). This low power probe clean design only has been utilized for laboratory setting, and not for a space flight instrument. For many small satellite missions, this 2.5 W of power is still too high; therefore, the second probe cleaning method was developed.

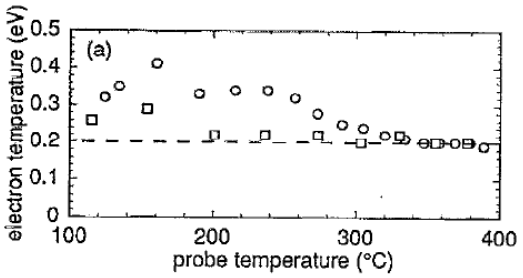

Figure 3.4 - Electron temperature data with respect to probe temperature. The dashed line marks the ideal electron temperature. [*Amatucci et al.*, 1993]

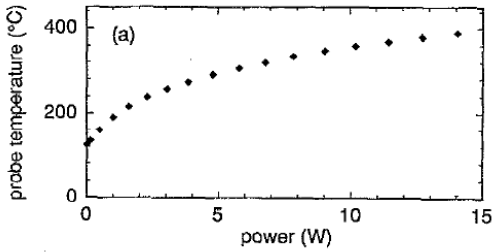

Figure 3.5 - Probe temperature versus required power [*Amatucci et al.*, 1993].

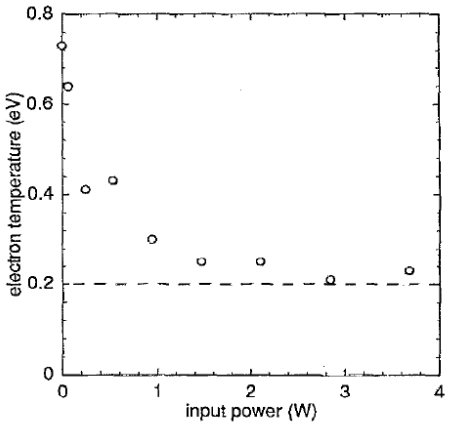

Figure 3.6 - Electron temperature data versus input power for new developed probe [*Amatucci et al.*, 1993].

The second method is to bias the probe with a high potential, such that the oppositely charged particles would bombard the probe surface and remove the contaminant layer. *Brace* [1998] developed this method for the Dynamic Explorer-2 mission. There were two probes on

the spacecraft, and only one probe contained the probe cleaning capability. Six days into the mission, the one probe was biased with the high voltage, and the data never displayed any signs of a contaminant layer before or after the clean. The probe was biased with high voltage for one complete orbit. This probe clean method was done early in the mission so that the effects of the space environment (e.g., exposure to the solar EUV, atomic oxygen, O, and atomic oxygen ion, O^+) did not change any characteristics of the composition of the probe. There was a probe clean procedure again later in the mission, but there was no change in the data, which suggests that only one probe clean procedure is necessary at the beginning of the mission.

For this instrument, the probe clean operational mode only occurs for long duration satellite missions due to the necessary clean time. This mode is required to be in operation for at least one orbit (approximately 90 min.) after one week the satellite is in orbit. This would ensure that the spacecraft would have finished outgassing, while still early in the mission so that the effects of the atomic oxygen do not react to the contaminants on the probe surface. If the spacecraft continues to outgass, then the probe clean mode needs to be in operation periodically until no more contaminants are present on the probe surface.

To define the requirements for the probe clean electronics, the current generated from the high voltage bias needs to be determined. Utilizing the OML equations, the current collected by the probe is found via **EQ2-7**. To determine the exact current, the probe surface area needs to be found first, which is determined in Section 4.2. Using the geometry found in that section, the maximum current collected using a density of 1×10^{12} m^{-3} (typical F-region peak) is

$$I_e = 381.2 \ \ \mu A .$$

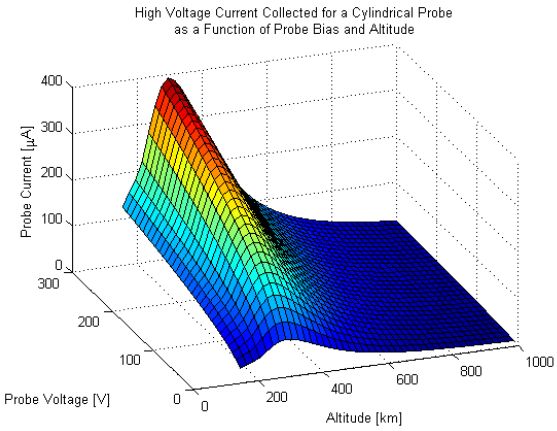

Figure 3.7 - Current collected during probe clean mode as a function of probe voltage and altitude for the typical ionosphere.

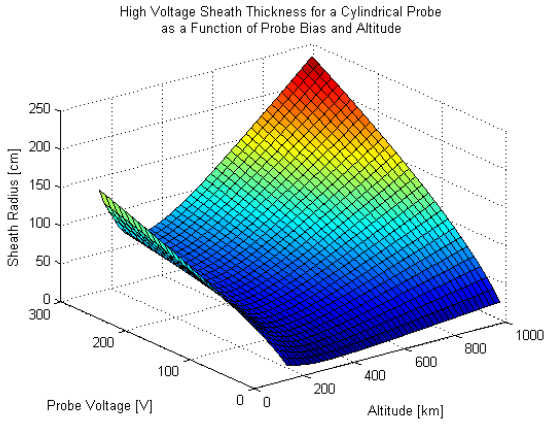

Figure 3.8 - Sheath thickness during probe clean mode as a function of probe bias and altitude for the typical ionosphere.

Figure 3.7 displays the ranges of currents for the typical ionosphere model (prescaled in Section 1.2.6) for the high voltage bias. The high voltage circuitry is required to be able to handle this current. Another interesting parameter to investigate is the sheath created by the high voltage bias. Figure 3.8 displays the sheath thickness for a range of voltages and altitude. If the current found above is true, then the sheath should not be perturbed by any outside influence. This is not the case, though, because there are fringing fields at the guard connected to the boom. The simulation does provide an approximation of the current collected. Figure 3.9 and Figure 3.10 display the current collected and sheath thickness for a probe biased to 150 V. The plot of the current is plotted linearly, and if the plot were a log plot it would have the same shape as the

density profile of the ionosphere, since the current and density are proportional to each other (see Equation **EQ2-7**).

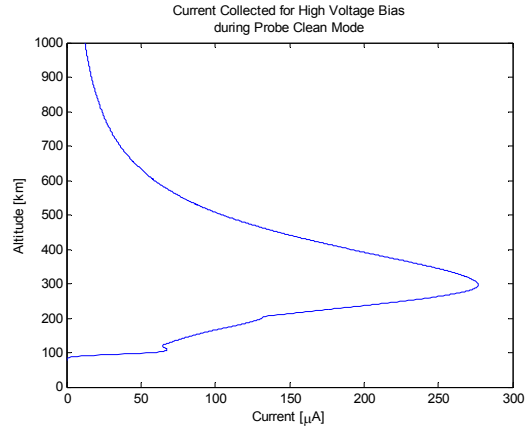

Figure 3.9 - Current collected during probe clean mode for a probe that is biased with 150 V as a function of altitude for the typical ionosphere.

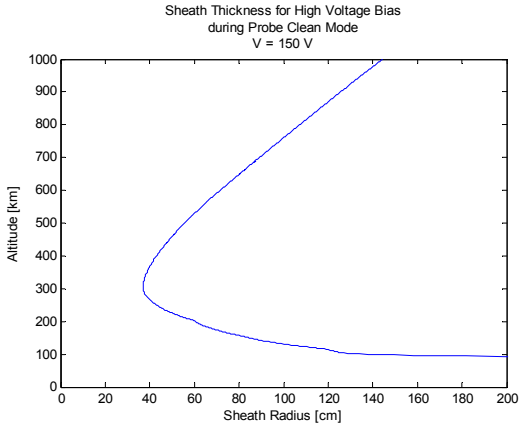

Figure 3.10 - Sheath thickness during probe clean mode for a probe that is biased with 150 V as a function of altitude for the typical ionosphere.

3.2 Electrometer Calibration

The electrometer is the primary electronic component, and calibration of the input current to the output voltage is usually done prior to the mission. For sounding rocket missions, the mission time is very short and there is no need to calibrate during the flight. The electrometer is usually calibrated before placement in the payload. For longer duration missions on satellites, the electrometer may experience temperature changes, and this may affect the output of the electrometer. Sounding rocket missions are able to use on-board calibration as well, so that the experimenter may have calibration data while the payload is on the rail right before the launch.

With regard to the operational modes, the electrometer calibration mode occurs while the payload is on the rail for sounding rocket missions and satellite missions and prior to each instrument operation for satellite missions. This electrometer calibration not only provides a relationship to the current drawn but also tests whether or not if the electrometer is operating properly or if there has been any change in operation. To accomplish on-board calibration, a board with a series of relays and high resistance low temperature drift resistors were used (see Section 4.4).

3.3 DC Bias

The DC bias mode is one of the three data collection operational modes. In this mode, the probe is biased to a constant potential, and the current is measured to attain high resolution density measurements. The probe can be either biased to a high negative potential or positive potential that would ensure the current collection to be in ion saturation or electron saturation, respectively. The current is proportional to the plasma density; therefore, if a reference density is known, then the density measurements can be fitted. If the mission requires high resolution relative density measurements, then this mode should be used. Some missions require only data of high resolution density fluctuations, where this instrument is called a DC probe, since the probe only operates in this mode.

3.4 Periodic Swept Bias

The periodic swept bias mode uses a specific voltage function that is repeated. In the past this voltage function has taken three different forms: sawtooth, triangle, and stepped function. Each voltage function is swept at a low frequency, i.e., at a few Hz. The sawtooth waveform biases the probe with a potential that is swept from either a negative voltage to a positive voltage or vice versa, then the function repeats (see Figure 3.11a). The triangle waveform is as it states, the potential bias is swept from a negative voltage to a positive voltage, but instead of repeating as in the sawtooth waveform case, the slope is opposite and the potential bias goes from a positive to negative voltage (See Figure 3.11b). The last waveform is the stepped function, where a constant voltage is applied for a certain time then the voltage is stepped up or down for the same amount of time until the desired maximum voltage is reached, as in Figure 3.11c. If using a digital-to-analog converter to generate these waveforms, then all waveforms are technically a step function; however, the step function only has a resolution of a few bits, meaning that the fewer bias voltages are applied for a longer duration of time than the other two functions.

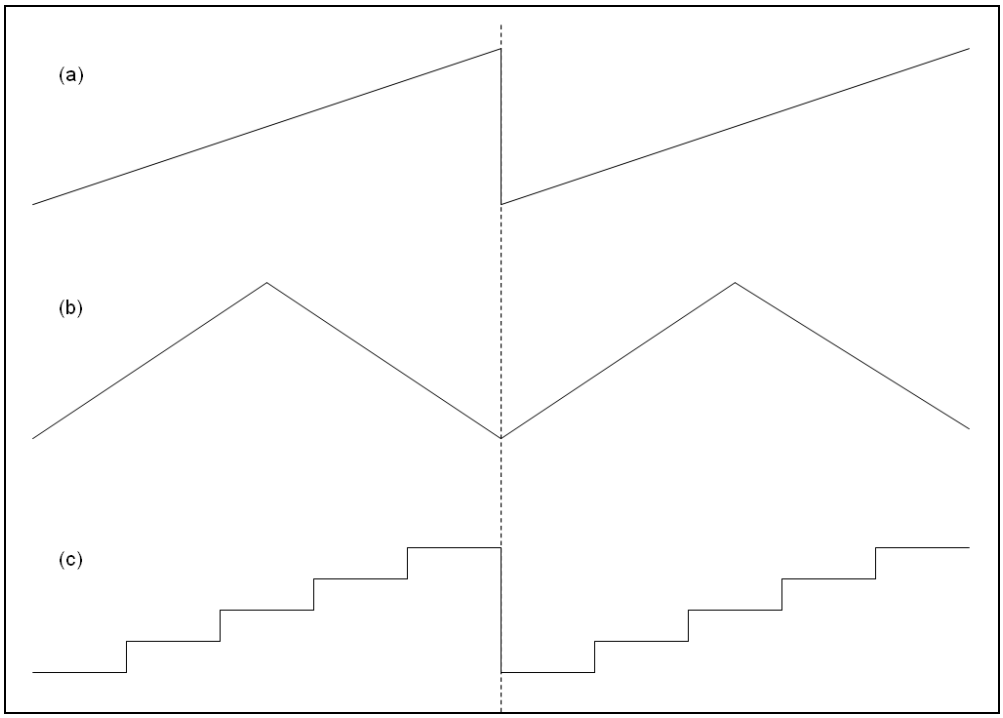

Figure 3.11 - Three different probe bias functions. (a) the sawtooth waveform, (b) the triangle waveform, and (c) step function.

For the flight instrument, the default periodic swept bias is the sawtooth waveform with a positive slope at a frequency of 1 Hz. This frequency provides a spatial resolution of about 1 km per sweep for sounding rocket missions and 7–8 km for one sweep for low earth orbit satellite missions. The Dynamic Explorer 2 (DE-2) mission used a sweep of 2 Hz; this higher frequency rate can be accomplished, but would require a higher data rate to attain the same resolution for the *I–V* curves. To save on data bandwidth, the swept rate of 1 Hz was specified as the default rate; however, this can be changed to 2 Hz if required by the mission. Another issue with the previous concept about the sawtooth waveform is a discontinuity that appears when the period repeats. To solve this issue, 10% of the swept period should be a constant voltage at the

extremes, as shown in Figure 3.12, in order to attain reliable stable data at the maximum and minimum biases. The positive slope was chosen over the negative slope, because if the probe surface were to become contaminated, accurate measurements for the electron temperature can still be made [*Piel et al.*, 2001]. The range of the sweep should also not be too large, because sweeping a large range would change the reference ground and provide faulty measurements. This was seen during the ESPRIT sounding rocket mission. Figure 3.13 displays the fixed biased probe data. The swept bias probe altered the spacecraft reference; therefore, there were measurement errors for when the swept bias voltage was much greater than the plasma potential. During this mission, the voltage was swept from –10 V to +10 V; therefore, the voltage bias should not be near this magnitude.

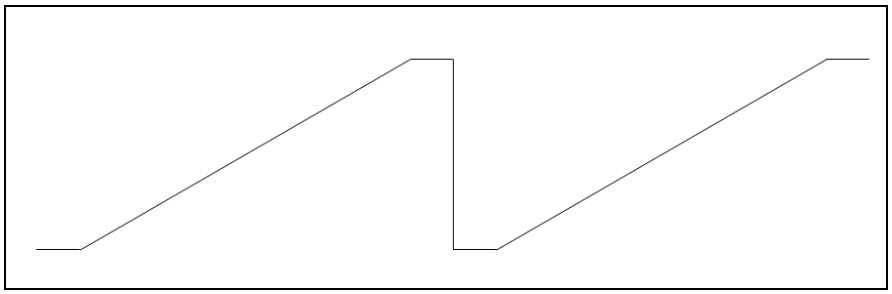

Figure 3.12 - Improved sawtooth waveform bias. This bias function includes the constant voltage bias at the minimum and maximum values that are each 10% of the period in duration.

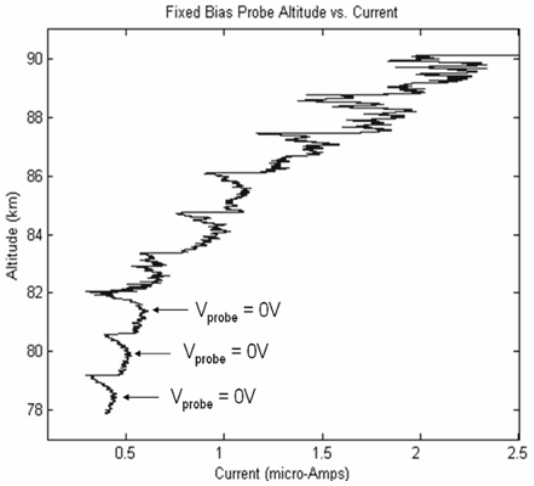

Figure 3.13 - Current collected by the fixed biased probe for the ESPRIT mission during the beginning part of the upleg illustrating the swept biased probe's effect on the current collection. The arrows mark wehere the probe voltage is 0 V with respect to the plasma potential [*Escobar et al.*, 2007].

3.5 Adaptive Swept Bias

The adaptive swept bias is similar to the periodic swept bias, except that the sweep is referenced to a certain parameter. One usual reference is the plasma potential, where the sweep changes due to this potential. Another reference is the floating potential, which sweeps about

this value. There are also adaptive sweeps that alter the sweep range relative to the electron temperature. For high temperatures, the slope of the electron retardation region is less and a wider range is necessary to obtain all three regions of the *I–V* curve. The opposite is true for lower electron temperatures. The DE-2 mission adjusted the swept bias such that the output of the electrometer created the same *I–V* curve for each sweep. This adjustment to the probe bias included the sweep range and location. The sweep started at –8.5 V with respect to the spacecraft ground, and the electrometer gain was adjusted such that the electrometer output was –3.3 V. Then the probe was swept to $8kT_e$ greater than this value to give an electrometer output of 9.5 V; therefore, the goal of the electrometer output was always in the range of –3.3 V and 9.5 V. There are other missions that have an adaptive sweep similar to this algorithm but with different reference voltages and values.

The instrument developed includes a simple algorithm for the adaptive sweep mode. The probe is swept with reference to the floating potential, which is similar to the Floating Potential Measurement Unit (FPMU) developed by *Swenson et al.* [2003]. The FPMU included four different instruments: floating potential probe, narrow swept Langmuir probe, wide swept Langmuir probe, and an impedance probe. The FPMU is utilized on the International Space Station (ISS) to monitor the plasma characteristics, especially the ISS potential relative to the plasma. The narrow swept Langmuir probe sweeps the voltage bias ±5 V from the floating potential. Then the raw data is sent to ground to be processed. A similar concept is employed for our instrument. The floating potential is found by a previous sweep (the first sweep is called the acquisition sweep), and the voltage bias is swept ±5 V around this potential with 10% of the period with a potential bias of the maximum and minimum value as in the periodic sweep. The acquisition sweep has the probe being biased ±5 V with the 10% rest period for the maximum and minimum as stated previously. Raw data is then sent to the on-board data handler for transmission to the ground station.

3.6 Low Data Rate Mode

Each of the previous bias modes send out raw data. A satellite mission may only require low resolution measurements, where processed data can be determined. The DE-2 mission adopted a similar concept, providing 0.5-second resolution data using the probe bias and gain adjustment technique stated in the previous section. The data set included one sample of ion density, electron density, electron temperature, and plasma potential.

For the Langmuir probe instrument designed, the probe is swept in a period of 0.4 seconds (2.5 Hz) with 0.1 seconds for processing time. The micro-controller does not need 0.1 seconds of processing time; however, this period is used to allow any overhead in data processing and/or communication. This would provide a 0.5-second time resolution, and about a 3.5 km to 4 km spatial resolution for low earth orbit.

First, an acquisition sweep is necessary; therefore, the probe is biased ±5 V with respect to the spacecraft ground over a period of 0.4 seconds, which includes the 10% constant bias at the minimum and maximum values, –5 V and +5-V respectively. Figure 3.14 displays the algorithm flowchart. The electrometer output is sampled at a rate of 1040 samples/second, and then averaged to 52 samples evenly spaced per sweep. This would provide 8 raw samples averaged for one averaged sample. Next, the plasma parameters are determined. The floating potential is the first parameter to be found. This is found simply by finding when the current is zero.

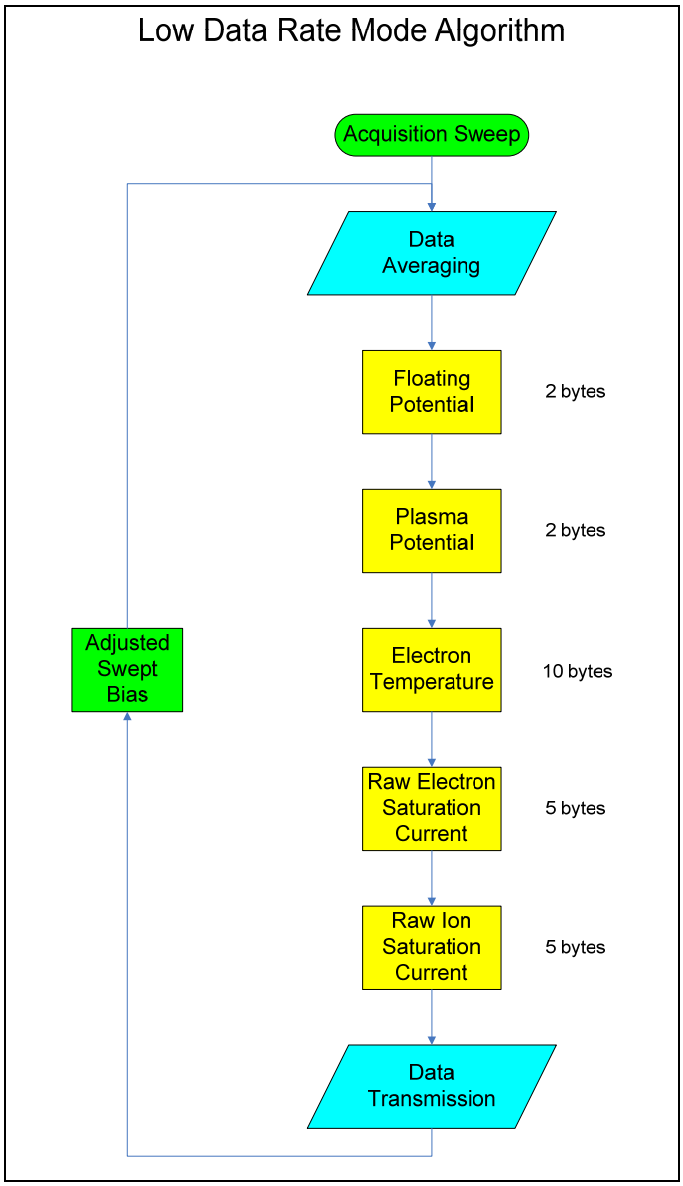

Figure 3.14 - Low data rate mode algorithm.

Second, the plasma potential is found by a simple method of comparing the slope of the *I–V* curve starting from the floating potential. Next, the slope between two consecutive points is found starting from the floating potential. Then, once the slope starts to decrease on an average, the first decrease in the slope marks the plasma potential. The two potentials are sent by two bytes each. With the floating potential and plasma potential known, two averaged data points on the *I–V* curve between these two values are taken and sent as an output. These two points provides the information necessary for determining the electron temperature. The total number of bytes for the electron temperature data is five bytes per sample, which gives 10 bytes to transfer. Then, two samples of raw data are sent for the electron and ion density. These samples are taken from the ends of the linear region, which is the start of the rest periods. These samples for the density are five bytes each. The total data volume per sweep is 24 bytes, which provides a total data volume of 48 bytes per second. With the on-board data analysis discussed, the next probe bias needs to be determined, and this is the same as the adaptive sweep section, where the

swept bias is adjusted according to the adaptive sweep. If there are two probes in operation with the low data rate and fixed bias modes, then the instrument is able to provide high spatial density measurements with the fixed bias probe and periodic ion density, electron temperature, and plasma potential relationships.

4 INSTRUMENT DESIGN

This chapter explains the flight instrument in detail. There are five main components for the flight instrument: probe and boom; electrometer; calibration and probe clean circuitry; signal conditioning and processing board; and the power board. The instrument design is based on the previous work conducted on the Penn State undergraduate sounding rocket mission ESPRIT. The mission goal for ESPRIT was to investigate numerous phenomena in the *D*-region and *E*-region high-latitude ionosphere. There are improvements from this design in all of the five components listed in this section. There are references to the instrument flown on ESPRIT throughout this section that mention these improvements.

4.1 Interface Diagrams

4.1.1 Electrical Interface Diagram

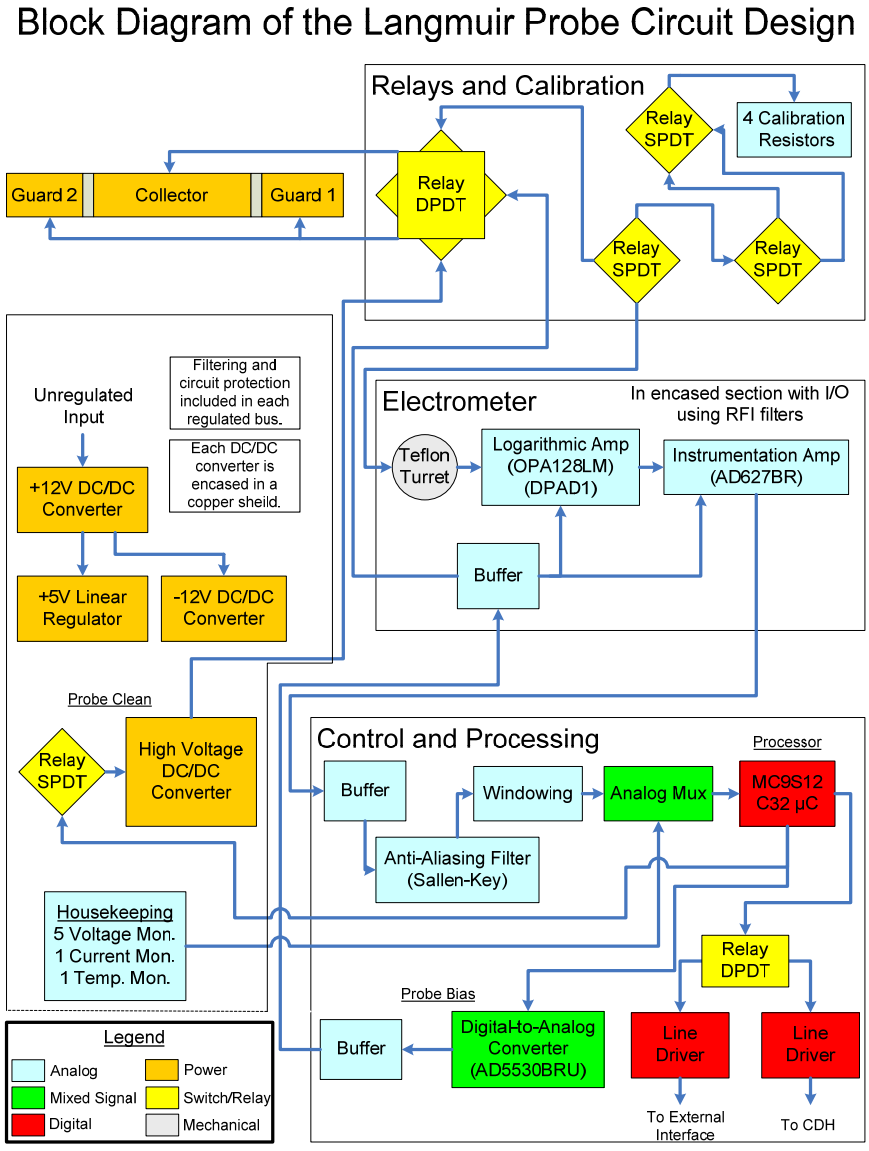

Figure 4.1 – Detailed internal electrical interface diagram. If two probes are used in a mission, then there will be two relay/calibration boards and two electrometers.

There are two types of electrical interface diagrams: internal detailed diagram and an external instrument connection diagram. Figure 4.1 depicts the internal components of the instrument. There are four boards listed in the diagram. The figure only represents the electronics for one probe. If two probes are used, then there is another electrometer and calibration board. The following sections in this chapter discuss the design of each of the boards in the figure. Figure 4.2 illustrates the external connections of the instrument. This diagram defines the connector types and purposes. There are two circuit boxes for the entire instrument, which are stacked up onto each other. The electrometer, calibration board, and control and processing board are located in box 1, while the power regulation board is located in box 2.

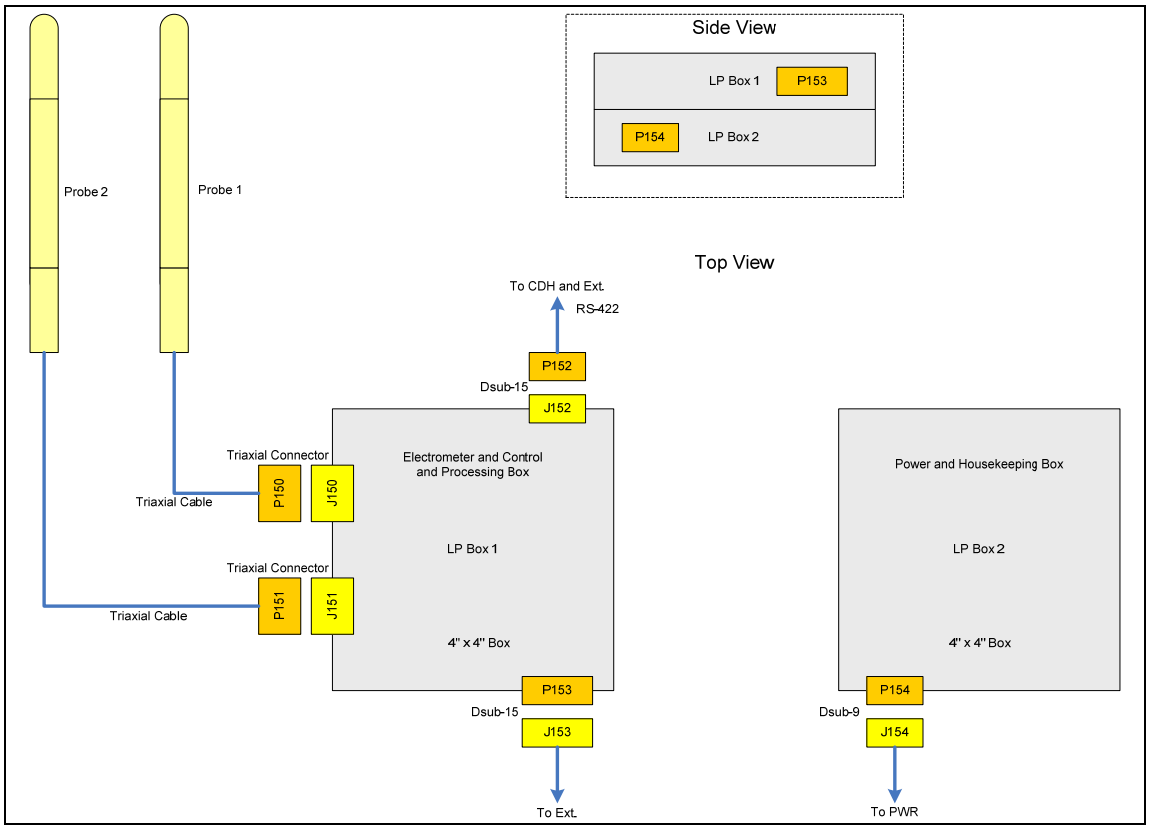

Figure 4.2 - Electrical interface diagram displaying instrument connections.

4.1.2 Mechanical Interface Diagram

There are four mechanical interface diagrams listed. The first diagram is an overview of the two boxes showing connector placement and box orientation (see Figure 4.3). Next, Figure 4.4 depicts the internal compartments for each of the boards. There are three compartments in box 1 and no divisions in box 2. The electrometer and calibration board share a compartment with one compartment per probe. A permanent divider separates the two compartments, and a removable slot separates these two compartments from the control and processing board. This removable slot contains mounting holes for the bolt-in filters (see Figure 4.5). The last diagram illustrates the components utilized for board to board connection. There are two female headers and one male header to provide the interface between the two boxes (see Figure 4.6).

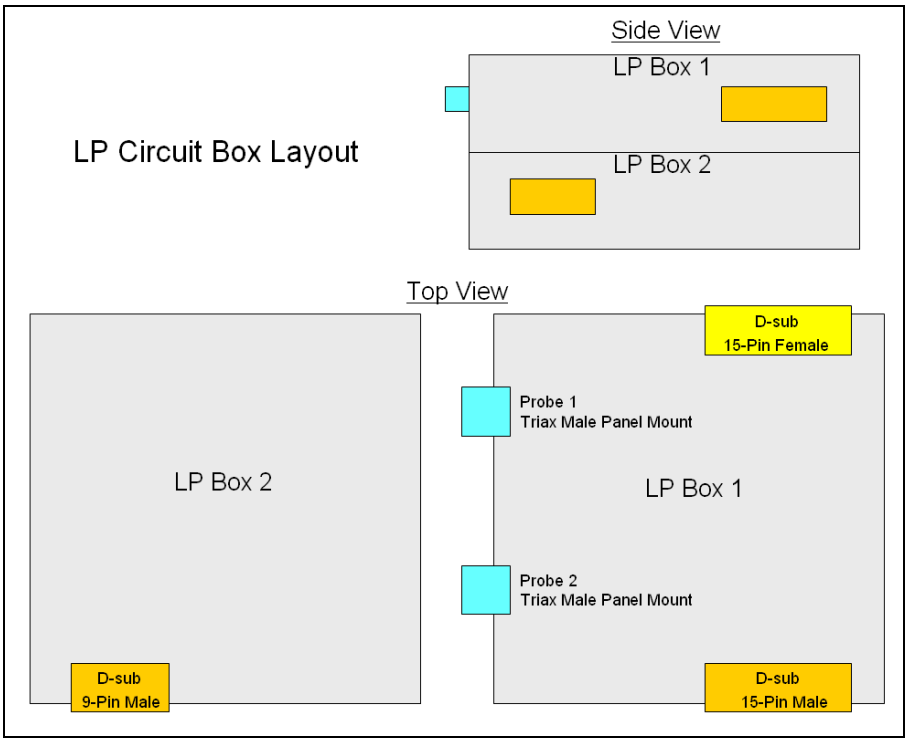

Figure 4.3 - Langmuir Probe (LP) circuit box and connector layout.

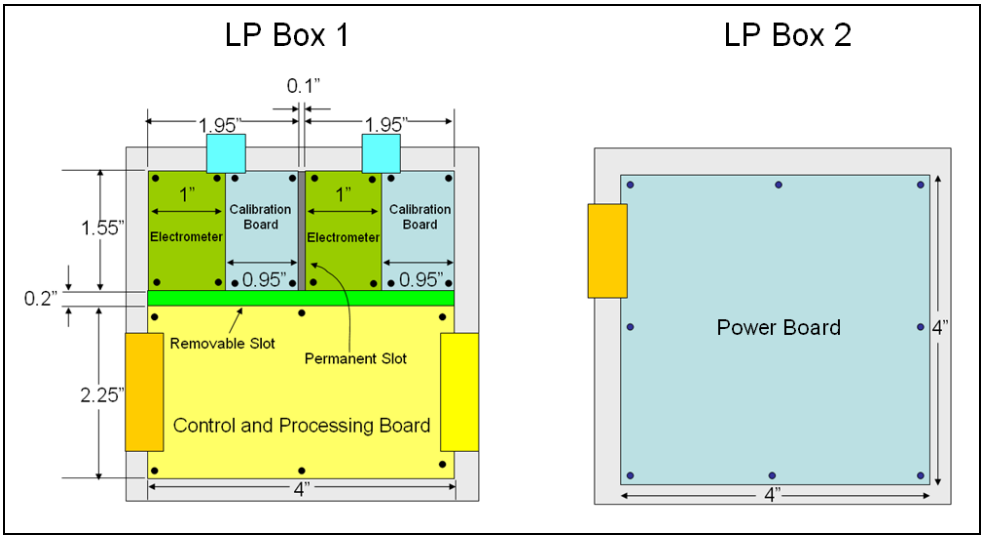

Figure 4.4 - Internal board dimensions and layout for each of the boxes.

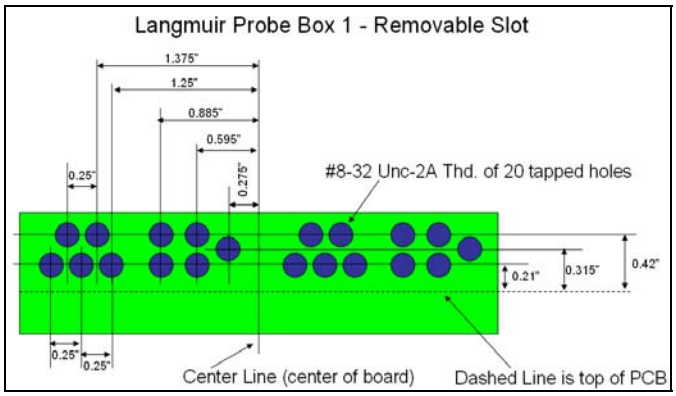

Figure 4.5 - Removable slot for LP box 1.

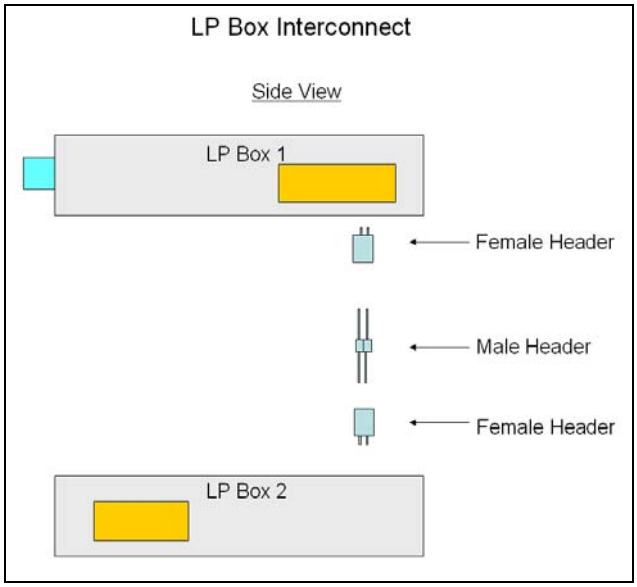

Figure 4.6 - Circuit box interconnect diagram.

4.2 Probe and Boom Design

OML theory is applied for the design of the probe, because it minimizes probe size and due to previous Penn State sounding rocket missions. The probe has to be able to operate in the space plasma environment taking into account the photoelectric effect, surface patchiness, chemical interactions, electric field fringing, and the geomagnetic field.

4.2.1 Probe Material Composition

The composition of the probe is an important factor in the design of the experiment, because of its interaction with the surrounding environment. The photoelectric effect, surface patchiness, and chemical interactions all impose constraints on the composition of the probe. Several different types of materials and coatings have been used in order to mitigate these effects of the space environment.

Three materials with high work functions were compared: gold, nickel, and platinum (see Table 4.1). DE-2 utilized rhenium probes; however, this material is not found in nature as a pure element and is very expensive to manufacture; therefore, rhenium is not a top candidate in this trade study due to its excessive cost.

Table 4.1 - Probe Composition Trade Study

Material	Work Function [eV]	Conductivity [S/cm]	Oxidation	Price*
Gold	5.10	0.45	no	2
Nickel	5.01	0.14	yes	1
Platinum	6.35	0.10	no	3

*Price is ranked from lowest (1) to highest (3) in cost per unit weight

Gold is selected as the best element to use. This element has the second best work function, highest conductivity, non-oxidizing property, and is the second cheapest. Platinum is another ideal material and has been used on other flights; however, the cost is too high when weighed against its performance. Nickel will degrade due to exposure to atomic oxygen in the ionosphere. Gold has been used on the ESPRIT mission, and the preliminary data analysis has shown similar results to the ground based measurements from EISCAT.

A problem with using gold, though, is that it is expensive and stock of the desired diameter is hard to find. Therefore, plating gold over a cheaper and more available material is the best solution. ESPRIT used brass as the material for the primary structure of the probe. Brass provides good mechanical support and conductivity. There are two issues found with gold plating any copper alloy: degrades hardness and non-oxidizing properties. The copper diffuses into the gold. If the probe oxidizes, this allows for particles to leave the surface and an oxidation layer will be form on the surface of the probe. This creates surface patchiness and errors in the measurement. To preserve the properties of gold, the brass is plated with electroless nickel then gold. The nickel layer keeps the gold layer from interacting chemically with the brass.

4.2.2 Probe Geometry

Electrostatic probe design has historically employed two primary geometries, spherical and cylindrical. Early missions had long thin wires that acted as their probes. This probe did not offer the best accuracy for reasons that are provided later in this section. For this flight instrument, the cylindrical geometry was chosen, since the probe radius must be smaller than the Debye length of the local plasma while still having enough surface area to collect enough current to be detected by the electrometer. The Debye length is dependent on the electron temperature and electron density; however, the electron density has a much greater effect in the Debye length. The smallest Debye length is found in the *F*-region peak. The maximum density and corresponding temperature as stated in Section 3.1 is 1×10^{12} m^{-3} and 3000 K. This provides a Debye length of

$$\lambda_D = 3.7798 \ \text{mm} = 0.14881 \ \text{in}.$$

The probe radius must be much less than this value. A stock diameter of 1/8 in. (0.3175 cm) brass was chosen for ease of manufacturing the probe. One could argue that a thin piece of wire would suffice as a cylindrical probe. This may be true for high density laboratory plasmas, where current collection may be enough for a short length, but with the ionospheric plasma, a much longer piece of wire is necessary in order to collect the same amount of current. There is one major issue where a potential difference in the probe is created due to the geomagnetic field and the velocity of the spacecraft. This potential is calculated later; let this fact be a priori that is proved later, so that the calculation of the collector dimensions continue with the 1/8 in. diameter brass cylinder. To determine the necessary length, the minimum plasma density as well as the minimum current detectable by the electrometer needs to be known. The ion density measurements generate the smallest currents relative to the electron density and temperature

measurements. The minimum density to be detected is 1 x 10^9 m^{-3}. Knowing device capabilities and previous knowledge of the ESPRIT electrometer, the minimum discernible current is 1 pA; however, these measurements are very susceptible to electromagnetic interference (EMI). Therefore, a higher current is used to provide a margin to the minimum discernible current, and this minimum current is

$$I_{\min} = 100 \ \text{pA}.$$

Using the above parameters and Equation **EQ2-13**, other parameters still need to be defined to find the length: the mean ion mass (m_i), the spacecraft velocity (v_i), ion temperature (T_i), and probe voltage with respect to the plasma (V). These parameters are to be derived for the D-region ionosphere, because this region has the lowest density, lowest temperature, and only can be reached by sounding rocket missions. These parameters are

$$m_i = \frac{m_{NO^+} + m_{O_2^+}}{2} = 23 \ \text{amu},$$

$$v_i = 1.5 \ \text{km/s},$$

$$T_i = 100 \ \text{K}, \text{and}$$

$$V = 5 \ \text{V}.$$

The mean ion mass is taken to be the average mass of the nitric oxide ion (NO^+) and the molecular oxygen ion (O^+). Using these values, the required minimum length of the collector should be

$$L_{\min} = 1.167 \ \text{in}.$$

The minimum length of the collector with a diameter of 1/8 in. was set to:

$$\boxed{L = 2 \ \text{in}. = 5.08 \ \text{cm}}.$$

The derived collector length accounts for even current collection throughout the entire surface of the probe. If the collector were only a blunt cylinder with the above dimensions, then the electric field distribution about the probe would not be evenly distributed due to fringing fields at the boom connection and probe tip. To mitigate the fringing electric fields, probe designs include "guard" pieces that are biased to the same potential as the collector. These guards allow the electric field around the collector to be normal to the entire surface area. The DE-2 and ESPRIT missions had a probe with a single guard at the boom connection and a cylindrical collector with a rounded spherical tip (See Figure 4.7a). *Brace* [1998], however, still found a problem with this geometry, where the probe "…tended to have large end effects," meaning that the end of the collector furthest from the boom collected more electrons than the rest of the collector.

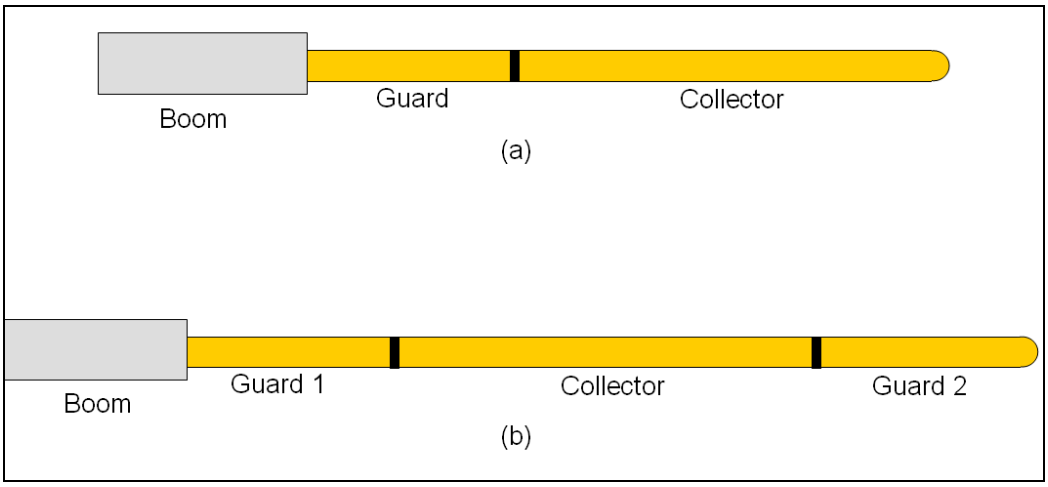

Figure 4.7 - a) Probe design used on ESPRIT and DE-2 missions. b) Newly developed probe design with two guards on either side of the collector.

The final probe design includes two guards: one at the boom–collector connection and one at the probe tip. This allows the collector to be only a cylinder (see Figure 4.7b). The guard at the boom–collector interface is a cylinder as well, and the guard at the probe tip is a cylinder with a rounded spherical tip. With the qualitative relationship presented, the dimensions of the guards can be found. *Brace* [1998] determined that a guard length of at least 1 in. (2.54 cm) is suitable to allow the collector to have no fringing fields; therefore, the guards are 1 in. in length, and the guard at the probe tip has an extra length of the spherical tip, which is the radius of the probe. The probe dimensions are summarized in Table 4.2. The guards and collector have to be isolated from each other, and this is accomplished by using thin Teflon spacers. To see the entire manufacturing process, see Section 4.2.3.

Table 4.2 - Probe Dimensions

Dimension	Value [in. (cm)]
Diameter	0.125 (0.3175)
Guard 1 Length (exposed length)	1 (2.54)
Guard 2 Length	1.0625 (2.6988)
Collector Length	2 (5.08)
Spacer Thickness	0.01 (0.0254)

As mentioned previously, the geomagnetic field effect on the probe is also important; hence, it is derived here. Due to the velocity of the spacecraft the geomagnetic field induces a potential difference along the probe due to the Lorentz force. The Lorentz force due to an ambient magnetic field is

$$F = q\vec{v} \times \vec{B}\,. \qquad \textbf{EQ4-1}$$

To find the potential created from this force, the work (energy) per Coulomb is needed. This is accomplished by dividing by the charge of an electron and multiplying the maximum distance electrons can move on the collector, which would be the length, L. The relationship becomes

$$\Phi_B = L\vec{v} \times \vec{B}\,. \qquad \textbf{EQ4- 2}$$

This relationship provides the reason why long thin wires cannot be used as collectors. There have been satellites that have aligned the probe axis with the magnetic field, such that there is no induced potential; however, this creates a more complex problem for the attitude control system. The design of this probe does not rely on the orientation with respect to the magnetic field; therefore, the maximum potential induced should be calculated to make sure that the collector length is short enough. The maximum potential induced is just the length, spacecraft velocity, and geomagnetic field all multiplied together. Using the ionosphere models found and a LEO satellite velocity of 7.8 km/s, the greatest induced potential is

$$\Phi_{B\max} \approx 20 \ \ \text{mV}.$$

This potential is small enough to not create errors in calculations. Figure 4.8 displays the induced potentials with varying geomagnetic field and satellite velocities as a function of altitude. The satellite velocities were derived by using the velocity calculated by circular orbits

$$v = \sqrt{\frac{3.986 \times 10^5}{r_{\text{Earth}} + a}}. \qquad \textbf{EQ4- 3}$$

where r_{Earth} is the radius of the earth and a is the altitude [*Tribble*, 2003]. The larger potentials in the *D* and *E*-regions can be disregarded, because there are no satellite orbits at these altitudes.

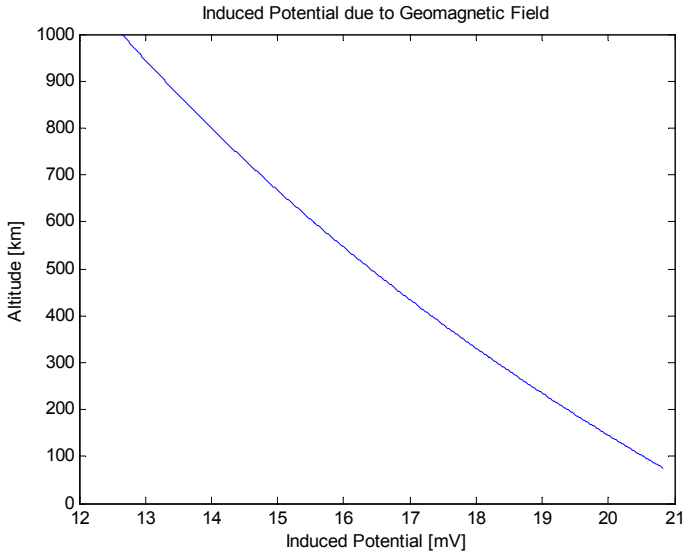

Figure 4.8 - Induced potential due to the geomagnetic field as a function of altitude, where the specific altitude corresponds to a satellite velocity for a circular orbit.

4.2.3 Boom and Probe Fabrication

The boom and probe fabrication process was kept simple as possible. The requirements of the boom were to be non-conducting, long enough to place the probe in the undisturbed plasma, durable enough to survive the launch vibration, and able to interface to the probe. The material used during the ESPRIT mission was a carbon fiber composite tube; however, the tube utilized only accounted for tensile force and not any shear force. Deployment tests for spin stabilized sounding rockets have been done at NASA Wallops Flight Facility, where the booms broke due to shear force; therefore, a carbon fiber boom with a "pre-preg" pattern that accounts for tensile and shear forces should be used. There are companies that manufacture these types of

tubes, especially for space applications. The length of the boom is derived from the sheath thickness created by the spacecraft. The voltage of the spacecraft ranges from –0.5 V to –1.0 V with respect to the plasma. The sheath thickness was derived for a planar surface in Section 2.2 by the Child–Langmuir Law with 1 V. The largest sheath thickness is found to be in the *D*-region ionosphere, and longer booms are required unless the probe is placed in the ram (i.e., tip probes). For LEO satellite missions, a boom length of at least 12 in. (~30 cm) should be sufficient. For higher altitude orbital missions, the booms need to be longer due to the larger sheath thicknesses. The diameter of the boom is constrained by the diameter of the probe interface, which is discussed next.

The previous section defined the probe length and diameter. here, the assembly procedure is discussed. There are 17 distinct parts that make up the probe. The three primary pieces are the collector and two guards. Besides these three pieces, there is a central titanium rod that acts as a "backbone" for the probe. There is also a silver plated copper braid that acts as an interface to the collector. Teflon spacers and Kapton tape act as insulators for the pieces, and there are a few nuts, washers, and a terminal for electrical connection. Table 4.3 provides a complete materials list for the probe.

Table 4.3 - Probe Materials List

Qty.	Part	Composition
1	Guard 1	Nickel / Gold Plated Brass
1	Guard 2	Nickel / Gold Plated Brass
1	Collector	Nickel / Gold Plated Brass
1	Inner Braid	Silver Plated Copper
1	Central Rod	Titanium
2	Spacers	Teflon
2	Collector Inner Insulator	Kapton Tape
1	Probe Interface to Boom	Teflon
4	0-80 Nut	Stainless Steel
2	0-80 Lock Washer	Stainless Steel
1	0-80 Ring Terminal	Stainless Steel
4	4-40 Screw	Nylon
1	Epoxy	Epoxy Resin
1	Sealant	Silicone

The three primary pieces (2 guards and collector) are composed of Brass 260 alloy. The guard between the boom and the collector is labeled as Guard 1, and the guard furthest from the collector is labeled as Guard 2 (see Figure 4.7b). Guard 2 is a solid brass rod of 1/8 in. diameter, where the center of one end is tapped to a size 0-80 screw, and the other end is rounded by use of a 1/16 in. radius concave endmill. The total length of Guard 2 is 1.0625 in., where the piece is a cylinder for 1 in. plus a hemisphere for the radius of the probe (0.0625 in.) at the tip. The collector is a brass tube with 1/8 in. outer diameter and 0.097 in. inner diameter. This is a stock item and did not have any extra machining other than being cut to length. Guard 1 is a brass tube with 1/8 in. outer diameter and 0.104 in. inner diameter. The stock piece has an inner diameter of 0.097 in. and has to be drilled out with a size 37 drill bit (this should be done on a lathe). Next, each piece is first plated with nickel (electroless) and then gold plated with type III (99.9%) gold with 50 μin. thickness.

Next, the interior parts that act as the mechanical support and electrical interface need to be made. The titanium rod has a diameter of 1/16 in. and is 5.625 in. in length. The rod is threaded with 0-80 die on each end for at least ¼ in. Then, the titanium rod is wrapped by Kapton tape between the two threaded sections. The Kapton tape is 0.0027 in. thick and wrapped 1–2 times at any one location. The titanium rod is then screwed into Guard 2. Next, a Teflon spacer is made by using an 1/8 in. round punchout and a 1/16 in. round punchout on a Teflon sheet of 0.010 in. thickness. This spacer is then slid down the Kapton wrapped titanium rod until it is flush with Guard 2. Then, the silver-plated copper braid is placed over the Kapton-wrapped section of the titanium rod. Next, the collector is slid over the silver plated copper braid and is set flush against the Teflon spacer and Guard 2. Then, the silver plated copper braid is wrapped by Kapton tape for the rest of the exposed section except for the last ¼ in. Another Teflon spacer is made with an outer diameter of 1/8 in. and inner diameter of 0.1 in. and is slid over the Kapton-wrapped silver plated copper braid. Then, Guard 1 is slid into place. A 1 in. section for a Teflon spacer is placed over Guard 1, leaving only 1 in. of exposed length. The Teflon spacer has an outer diameter of 0.25 in. and inner diameter of 1/8 in. This Teflon spacer acts as the mechanical interface to the boom. This piece has epoxy placed at the Guard 1–Teflon interface and at the Teflon–boom interface. Before the probe is adhered to the boom, the electrical interface to the triaxial cable is needed. The nuts, washers, and terminals need to be aligned as shown in step 8 in Figure 4.9. The terminal provides access to the two guards, and the exposed silver-plated copper braid provides access to the collector. These junctions are soldered to the triaxial cable with the center conductor soldered to the silver plated copper braid and the inner shield soldered to the guard. The outer conductor of the triaxial cable is left floating at the probe end and tied to ground at the opposite connection at the electrometer. The triaxial cable is cut to a length required to provide an interface from the probe to the electrometer. Next, the traixial cable is fed through the boom, and a male triaxial cable connector is attached at the end to be connected to the electrometer. To attach the probe to the boom, RTV 3145 is used to isolate the electrical connections, and then durable epoxy is placed on the outside of the 1 in. Teflon piece to adhere to the boom. Since the probe is fully assembled, the collector and Guard 2 can be removed to prevent any contaminants from going onto the surface during the integration phase of the payload. These pieces can be attached right before launch. Figure 4.9 illustrates the step-by-step guide. Figure 4.10 is a photograph of the final probe assembly.

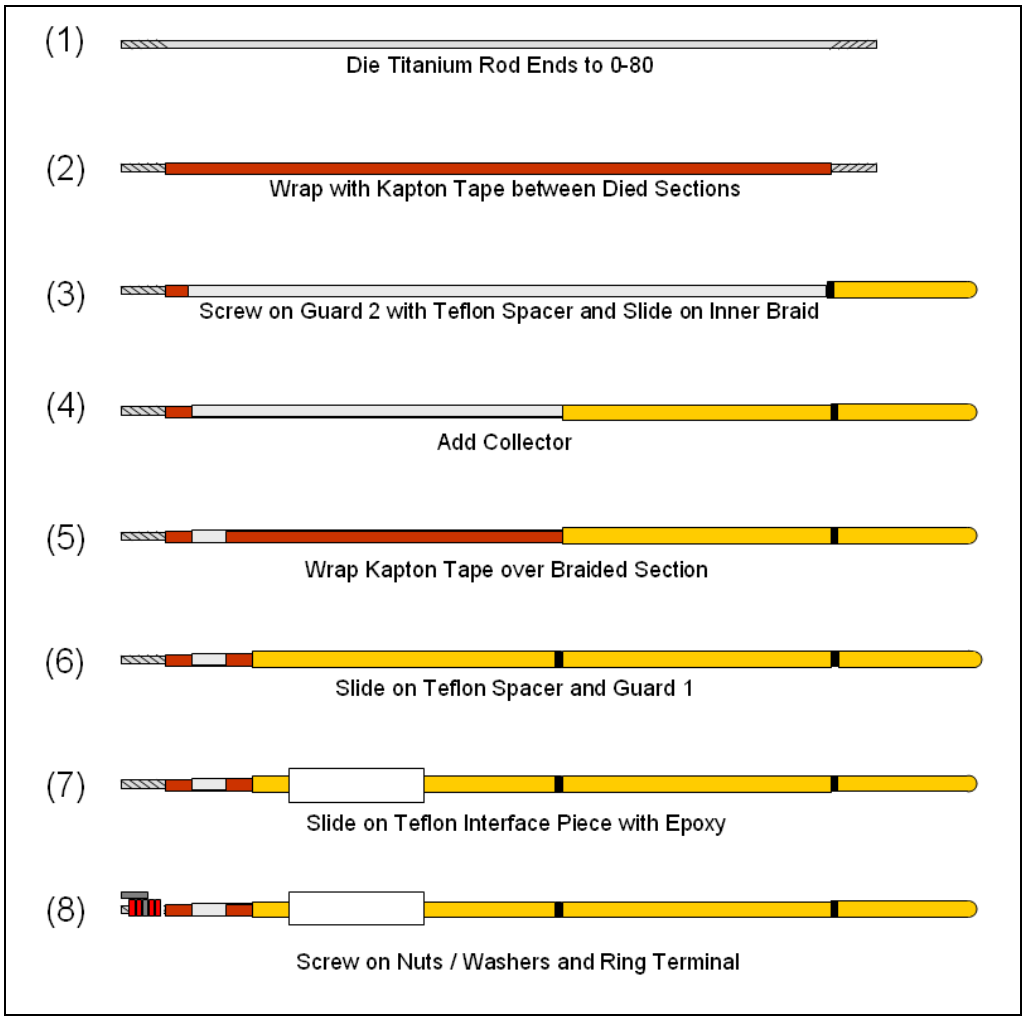

Figure 4.9 - Probe assembly procedure.

Figure 4.10 - Photograph of Langmuir probe.

4.3 Electrometer

As stated previously, the electrometer is the primary electronic component for measurement, and the electrometer is very susceptible to electromagnetic interference. The design of the electrometer takes into account the filtering and shielding necessary in order to provide accurate measurements. The heart of the electrometer is the OPA-128LM, which is an electrometer-grade radiation-hardened op-amp. Input bias and offset currents are on the order of tens of femto-amps.

The electrometer designed is a logarithmic amplifier accomplished by a pair of feedback diodes. The logarithmic amplifier allows a large range of currents to measure many different ionopheric plasma densities. The feedback diodes are required to have low leakage currents as well; therefore, the DPAD1 was chosen from Vishay Siliconix. The OPA-128LM is biased at the non-inverting terminal, and this allows the probe to be at the same bias potential. This

configuration allows the current collected to be drawn through the feedback diode; however, this design alone may convert the current to a voltage, but if the output were to be sampled single-ended, then there is little noticeable change in the current collected.

In order to provide higher resolution and less interference to the signal, an instrumentation amplifier is used at the output to the logarithmic amplifier, to which the probe bias is the differential pair. Having a differential input to an amplifier lowers differential mode and common mode noise. The amplifier was chosen to have a high common mode rejection ratio. The Analog Devices AD627BR was selected, which has a minimum common mode rejection ratio of 83 dB with a typical value that is 10 dB greater. The AD627BR also has rail-to-rail output, thus allowing a larger range of collected current.

The requirement for the current collection range drives the gain setting of the electrometer. The probe geometry and plasma densities define the requirements of the current collection range. The minimum current collected is stated to be 100 pA in the previous section, due to the lowest plasma densities in the *D*-region ionosphere. The maximum current collected needs to be calculated in a similar manner. The maximum currents occur in the electron saturation region, and the electron density and probe bias potential are the factor in the magnitude of the collected current. As mentioned before, the maximum density would be at the *F*-region peak with a density of 1×10^{12} m^{-3}. Using equation **EQ2-7** and assuming a +5-V bias potential relative to the plasma potential, the maximum current drawn is

$$I_e = 69.613 \ \ \mu\text{A}\,.$$

To determine the output of the log-amp, the forward biased diode equation should be used

$$I_d = I_S\left(e^{qV/(nkT)} - 1\right), \qquad \textbf{EQ4-4}$$

where I_S is the saturation current, V is the voltage drop across the diode, q is the charge of an electron, k is Boltzmann's constant, T is the absolute temperature, and n is a constant due to the fabrication of the diode's material and physical structure. The saturation current, I_s, is a function of cross-sectional area and temperature. The saturation current is on the order of femto-amps (10^{-15} A). In the exponential term, kT/q is known as the thermal voltage, v_{th}. The typical value of the thermal voltage is 25 mV. The constant n ranges in value between 1 and 2. The above diode equation can be approximated further as

$$I_d = I_S e^{V/(nv_{\text{th}})}, \qquad \textbf{EQ4-5}$$

assuming that the diode current is much larger than the saturation current ($I_d >> I_S$). In this case, the diode current is over 10 orders of magnitude greater than the approximated saturation current. The approximated voltage across the diode is

$$V = nv_{\text{th}} \ln\left(\frac{I_d}{I_S}\right), \text{ or} \qquad \textbf{EQ4-6}$$

$$V = (1.5)(0.025)\ln\left(\frac{69.613\times10^{-6}}{10^{-15}}\right) = 0.936 \ \ \text{V}\,.$$

This voltage cannot be used as an exact indication of the voltage drop across the diode, but can be used as an approximation to determine the first value of the gain stage following the OPA128LM. The value found is within the range of the forward voltage drop specification in the datasheet of typically 0.8 V to 1.5 V max. With the above voltage, the maximum gain allowed within a ±12 V power system is G = 12.82 V/V. From here the gain of the instrumentation amplifier is set by choosing a specific resistor value. The actual gain required for this electrometer design was found experimentally for the ESPRIT mission. For the peak

current above, a gain of G = 18 V/V would suffice. The ESPRIT instrument utilized a gain of 20 V/V since the apogee of the rocket was to be less than the F2-Region. Figure 4.11 displays a photograph of the inside and outside of the electrometer used in ESPRIT. Figure 4.12 provides a generalized schematic of the electrometer electronics. The general design for the ESPRIT electrometer and the newly developed electrometer are the same. The difference is in the board layouts. The ESPRIT electrometer board layout is made for a stand-alone box, and the newly designed electrometer board is to be included into one 4 in. x 4 in. box with calibration board and control and signal processing board.

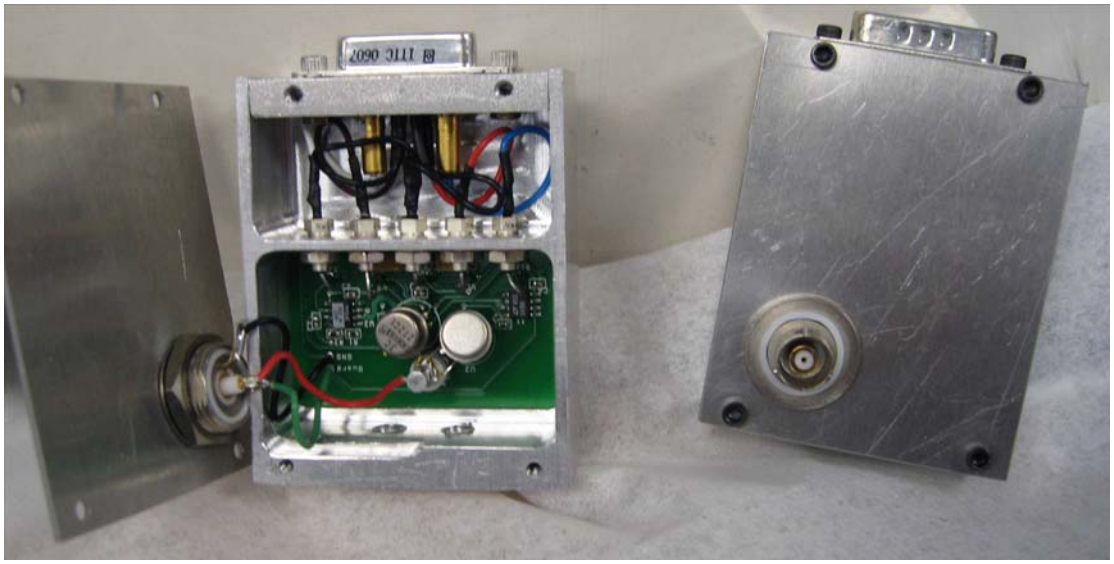

Figure 4.11 - Photograph of two of the electrometers used for ESPRIT.

In an ideal world, the above electrometer design alone would operate correctly; however, there are several factors to prevent electromagnetic interference that need to be discussed. First, the collected currents are extremely small, and this current can be affected by inductive and capacitive crosstalk from external sources. The collected current connection should be shielded, except a coaxial cable with the outer conductor grounded cannot provide the necessary shielding. Using a coaxial cable, there is capacitance between the center conductor and the outer conductor that affects the ideal current to be measured; therefore, a triaxial cable is used to interface between the probe and the electrometer with the inner braid set at the same potential as the center conductor. The same concept is applied internal to the electrometer. Low noise techniques should be applied to the interface of the OPA128LM. There are two recommended design methods. The input signal should not be placed on a printed circuit board, and should be connected to the electrometer by way of an isolated Teflon standoff. In the design of the LP instrument, the electrometer has to interface to the probe, the high voltage probe clean circuitry, and the calibration circuitry. Small electro-mechanical relays provide the switching, and the interfacing between components is done through wire-to-wire connections. Each electro-mechanical relay case is connected to the probe bias as well. Lastly, each input and output to the electrometer electronics and probe clean and calibration board utilizes a radio-frequency interference (RFI) filter. The filters used are the 1250-003 bolt-in filters from Spectrum Control. These filters are placed in a removable slot to interface between the control and processing board and each of the electrometers and probe clean and calibration boards (see Figure 4.4 and Figure

4.5). Utilizing these bolt-in filters provides optimum isolation from the control and processing board and any outside interference.

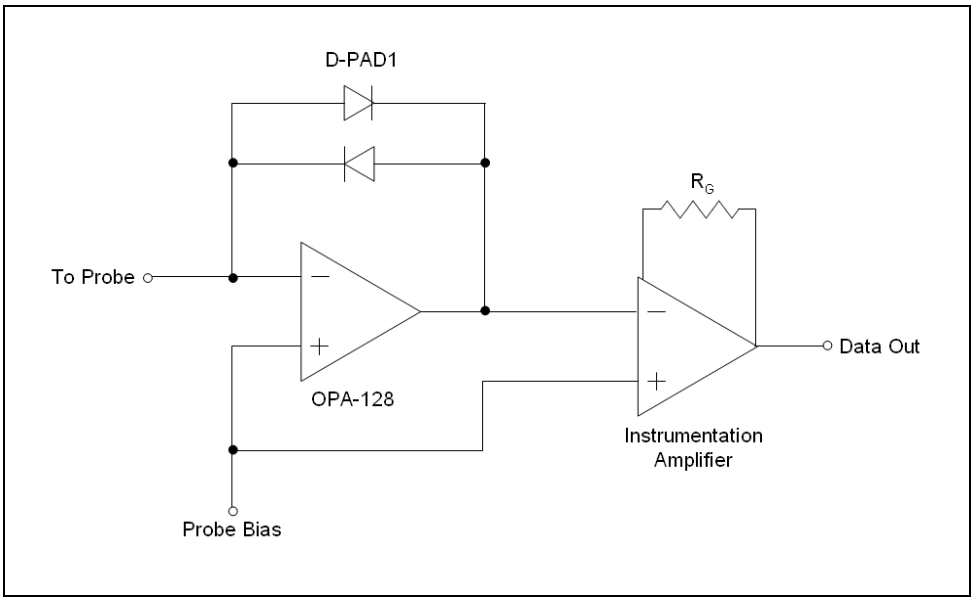

Figure 4.12 - Generalized schematic of the electrometer.

4.4 Probe Clean and Calibration Board

The probe clean and calibration board provides the interface between the electrometer, the probe, the probe clean circuitry, and the electrometer calibration circuitry. This board does not contain the probe clean circuitry; it just interfaces the probe clean circuitry from the power regulation board to the probe. Since the currents are on the order of pico-amps and micro-amps, solid-state relays cannot be used. Instead, small electro-mechanical relays from Teledyne Relay are used. The specific relays implemented are the 136C DPDT relays, which include a digital MOSFFET interface to allow a +5-V signal to activate the coil. The relays are capable of handling 30 g's in sine vibration to 3000 Hz and a shock of 75 g's. The maximum acceleration stated in the datasheet is 50 g's. These specifications meet the vibration environment requirements for the sounding rocket and satellite missions.

Four relays provide the switching interface to the four components. As mentioned in the previous section, the case of each relay is connected to the guard probe bias. Each interconnect is accomplished by using a small coaxial cable with the outer shield connected to the guard bias. This interconnection ensures the isolation between terminals and any interference effects.

The calibration resistors are also included on this board. These resistors are high resistance and high precision with 1% tolerance. The resistor series is the Victoreen resistors developed by Ohmite. The traditional Victoreen resistors are long glass encapsulated; however, there have been advances in technology that allow smaller packages with similar operating characteristics. The MOX400 series of resistors were chosen for implementation, because of their small size, high precision, and small temperature coefficients. The resistors have a typical temperature coefficient of 50–100 ppm/˚C. The four resistances used are 10 MΩ, 100 MΩ, 1 GΩ, and 10 GΩ.

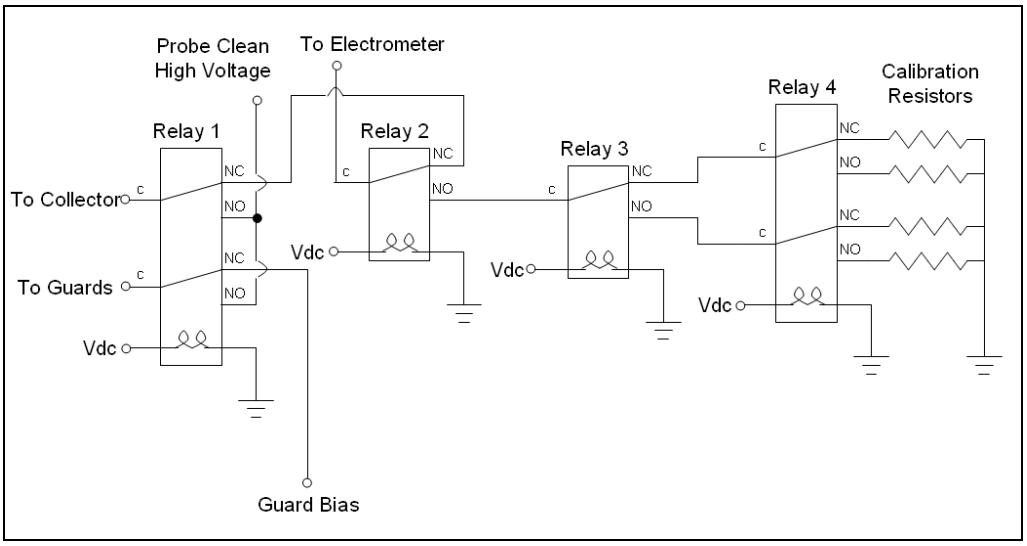

Figure 4.13 - Generalized design of the probe clean and calibration board.

With the device description stated, the board operation can be explained. The first relay (relay 1) switches between the electrometer relay (relay 2) and the high voltage bias. When the input signal is high, then relay 1 switches the probe clean high voltage to the probe and guards, while isolating the electrometer. The second relay has the electrometer as the common and switches between relay 1 and the second calibration relay (relay 3). The third relay allows the switching between the two sets of four calibration resistors through relay 4. The final relay (relay 4) switches between the four resistors. Figure 4.13 displays the schematic of the relays. Each logic input to the relay has a pull down resistor, so that if the input were to be floating, then the voltage to the gate would remain less than the threshold voltage. To minimize EMI, each input is isolated from the control and processing board by the same RFI bolt-in filters mentioned in the previous section. The bolt-in filters are fastened to the same removable slot as well.

4.5 Control and Processing Board

The control and processing board contains the signal conditioning for the electrometer output, the bias circuitry, the microcontroller, and communication line drivers. The electrical interface diagram in Figure 4.1 illustrates all these components. This board is capable of supporting two probes simultaneously. The microcontroller has an on-board analog-to-digital converter (ADC) that samples the output of the signal-conditioning circuitry. The processor also sends the data to a digital-to-analog converter (DAC) to create the voltage bias for the probe. Communications is accomplished by the serial communication interface on the microcontroller to line drivers. The board is capable of communicating via two different types of asynchronous protocols: RS-232 or RS-422.

4.5.1 Signal Conditioning

The signal conditioning circuitry creates higher resolution of the data output from the electrometer to be sampled by the microcontroller. There are two main parts in the signal conditioning circuitry. The first converts the entire output range of the electrometer to a 0–5 V signal that can be sampled by the microcontroller. The second provides is windowing stages. There are four different windowing ranges into which the output of the electrometer is divided.

These divisions allow the different sections of the *I–V* curve to be examined closely. Figure 4.14 depicts the signal conditioning flow chart in detail.

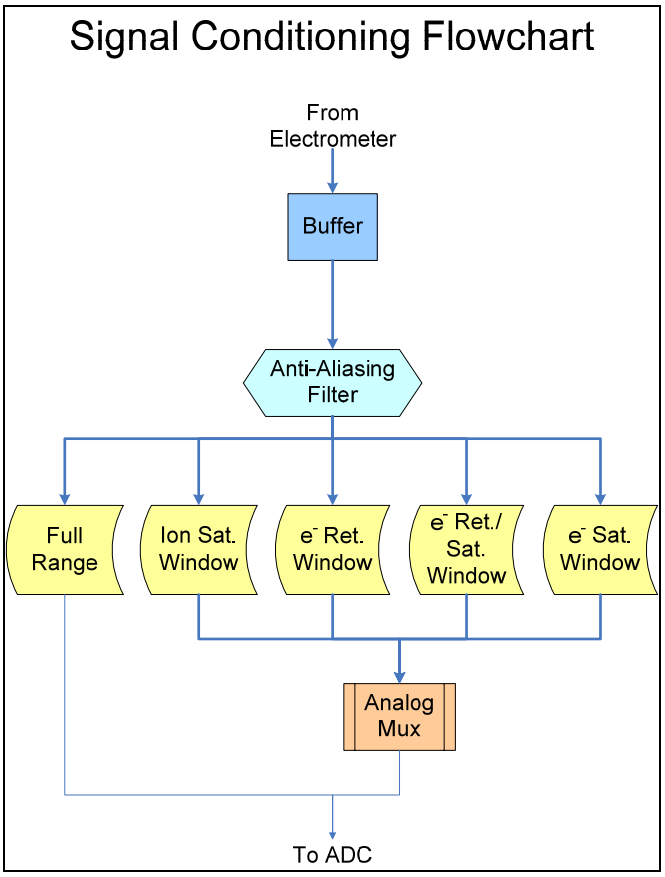

Figure 4.14 - Signal Conditioning Flowchart.

Before the gain stages, there is an input buffer and an anti-aliasing filter. The input buffer provides high input impedance prior to the gain stages. This buffer is accomplished by implementing a simple voltage follower. The anti-aliasing filter is a 2-pole Sallen–Key active filter. The minimum sampling rate is set to be 1000 Hz, where the gain of the filter is set to be a –20 dB at the Nyquist frequency (see Figure 4.15). With this configuration, the cutoff frequency of the filter is 100 Hz. The inline resistance to the non-inverting terminal of the op-amp is kept small in order to reduce the effect of the input bias currents. The resistance is not made too small, because the capacitance then needs to be larger. High value capacitors are not common for small surface mount packages. The values for the components are listed in Table 4.4. The circuit is pictured in Figure 4.16, and the transfer function is

$$\frac{v_o}{v_i} = \frac{1}{s^2 R_1 R_2 C_1 C_2 + s\left(R_1 C_1 + R_2 C_1\right) + 1}. \qquad \textbf{EQ4-7}$$

Figure 4.15 shows the Bode plot for this transfer function with the different frequencies of interest mentioned previously.

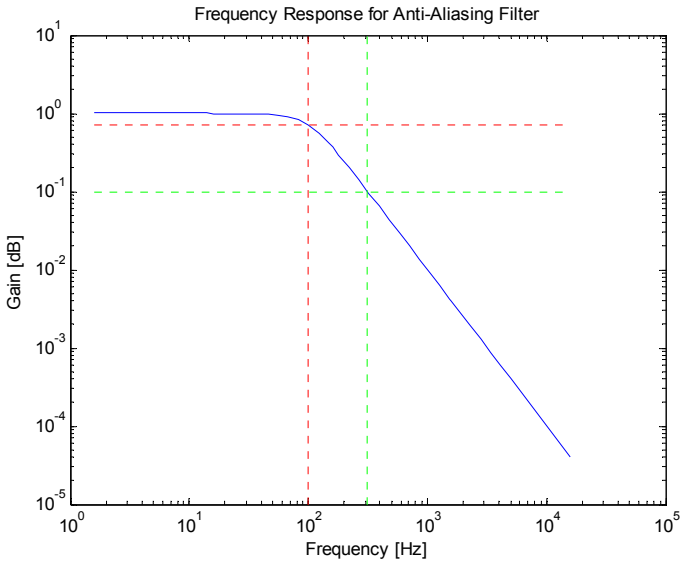

Figure 4.15 - Frequency response for the anti-aliasing filter. The dashed red crosshair marks the –3 dB gain at 100 Hz, and the green dashed crosshair marks a gain of –20 dB at the minimum Nyquist frequency of 316 Hz.

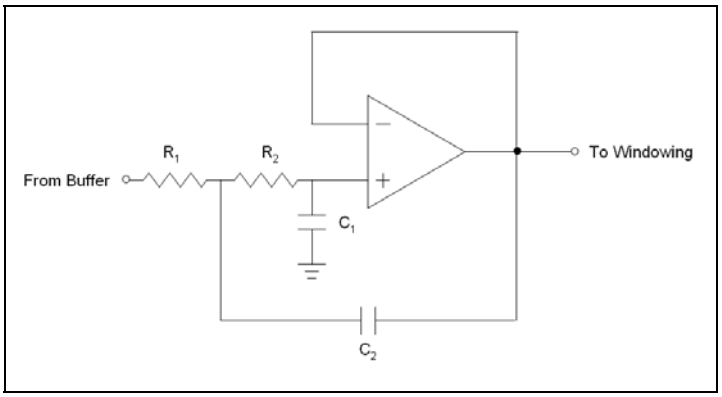

Figure 4.16 - 2-pole Sallen–Key anti-aliasing filter design.

Table 4.4 - Anti-Aliasing Filter Component Values

Component	Value	Unit
R_1	274	Ω
R_2	1960	Ω
C_1	1	µF
C_2	4.7	µF

The full range and windowing amplifiers are after the anti-aliasing filter. Each amplifier stage has one of the following configurations: inverting, summing, or difference. These configurations were chosen because of the amplification and linear relationship between the input and output. Figure 4.17 displays the general configuration of each type. As mentioned previously, the full range captures the entire range of the electrometer output and compresses the signal between 0 V and 5 V, because this is the allowable range of input to the analog-to-digital

converter on the microcontroller; therefore, each windowing stage requires a 0 V to 5 V output. The other windowing stages expand different sections of the electrometer output.

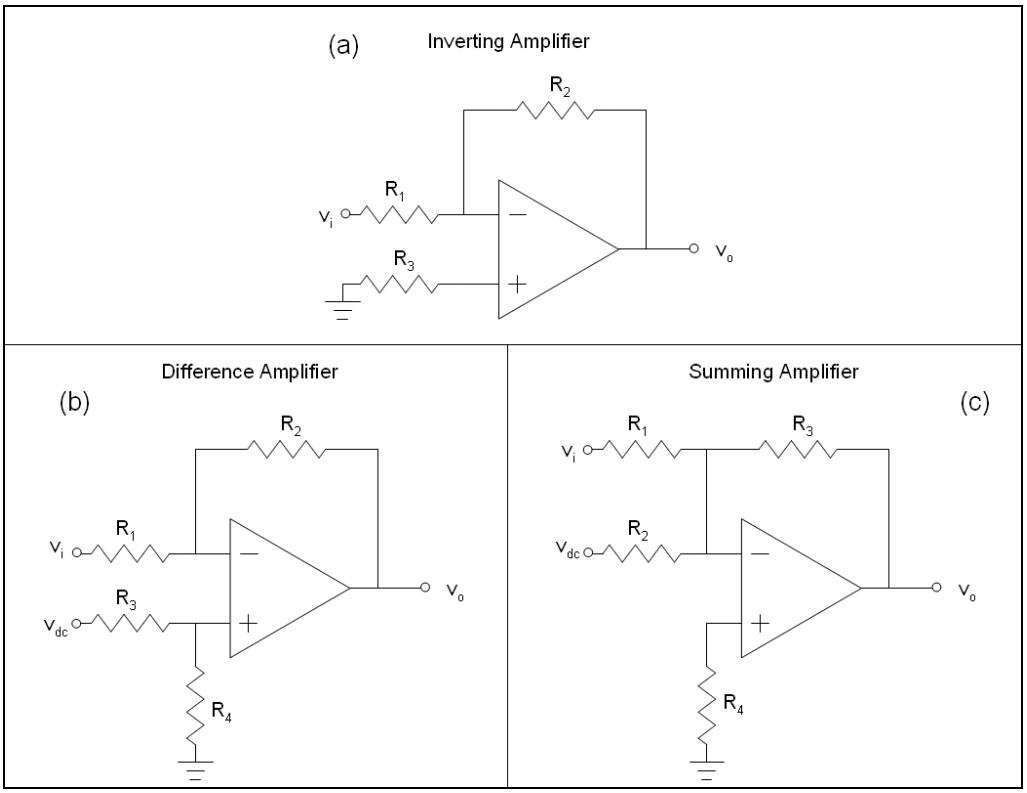

Figure 4.17 - Configurations of amplifiers used. The values of the components associated in each amplifier are listed in the table below. a) Inverting amplifier used for electron retardation window. b) Difference amplifier used for full range and ion saturation window. c) Summing amplifier used for electron retardation/saturation and electron saturation window.

The first windowing stage is the ion saturation windowing amplifier. This amplifier windows the electrometer data that provides current collection in the ion saturation regime. The next windowing stage amplifies the electron retardation region. The last two windowing stages amplify the electron saturation region; however, one stage amplifies part of the electron retardation region and part of the electron saturation region. These relationships to the windowing stages were created due to the expected current collected for the typical ionosphere. Table 4.5 provides relative data for each of the windowing stages. The densities found are assumed for a probe voltage that is 3 V greater than the plasma potential for each current collection case. This means that the values found are not for a specific plasma, but a range of acceptable densities; however, the range of applicable electron densities in the ionosphere are for only the last two stages. This is the reason why the second windowing stage is labeled the electron retardation stage. Electron temperature data is most likely to come from this stage. The positive ion density is found by the first stage in the ion saturation region. This one windowing stage captures the entire range of possible densities. Table 4.6 lists the coefficients of a line that represents the transfer function of each stage. These coefficients determine the amplifier configuration and component values. Each component value corresponds to a standard manufactured resistor value. The control and processing board contains two of these signal conditioning circuits, where there is one for each probe.

Notice that each stage has overlapping ranges except for the ion saturation window and the electron retardation window. The overlap allows for no end effects out of the linear region of the op-amp, even though the op-amp is rail-to-rail input and output. The region between the ion saturation and electron retardation window do not have an overlap because this boundary marks the floating potential of the probe. When the probe is swept from a negative voltage bias to a positive voltage bias, the probe data output goes from the ion saturation window to the electron retardation window. When this occurs, the associated probe bias marks the probe floating potential. This transition marks the floating potential by an simple logic comparison between the two windows. This can also be marked by the full range window, when the data output crosses the half-way mark, which happens to be 512 counts for a 10-bit analog-to-digital converter.

Table 4.5 - Windowing Stage Ranges

Window Stage	Input Voltage Range [V]		Current Range [A]		Density Range [m^{-3}]	
	V_{min}	V_{max}	I_{min}	I_{max}	n_{min}	n_{max}
Full	–12	12	1 p	268 μ	---	7.8×10^{12}
Ion Saturation	0	9.5	1 p	1.62 μ	---	6.3×10^{12}
e^- Retardation	–6	0	1 p	1.6 n	---	---
e^- Ret./Sat.	–9.5	–5.5	589 p	1.79 μ	1.7×10^{7}	5.2×10^{10}
e^- Saturation	–12	-9	655 n	268 μ	1.9×10^{10}	7.8×10^{12}

Table 4.6 - Line Equation and Component Values for the Windowing Amplifiers

	Full	Ion Sat.	e^- Ret.	e^- Ret./Sat.	e^- Sat.
Slope: A	–5/24	–10/19	–5/6	–5/4	–5/3
Intercept: B	2.5	5	0	–6.875	–15
Amp Type	Difference	Difference	Inverting	Summing	Summing
R_1 [Ω]	12 k	7.5 k + 11.5 k	12 k	11 k	18 k
R_2 [Ω]	1 k + 1.5 k	10 k	10 k	10 k	10 k
R_3 [Ω]	3.4 k	10 k	3.65 k + 1.8 k	13 k + 750	30 k
R_4 [Ω]	2.4 k	7.5 k + 11.5 k	---	3.6 k + 191	5.1 k + 191

There are a few practical design techniques that need to be mentioned for the signal conditioning section. To allow only a 0–5 V signal to the ADC, the op-amp for the full range stage and windowing stages are single supply op-amps that operate from +5-V. This op-amp is from Linear Technology designed as part numbers LTC2051 and LTC 2052. These two part numbers signify if it is a dual or quad configuration, respectively; therefore, if the electrometer output creates one of the windowing stages to rail, then the op-amp would rail at the supply voltage. These op-amps have very low input bias currents and offset voltages. They are also rail-to-rail input and output with low power consumption (less than 1 mA per amplifier). Another approach to prevent over-voltage was to add a shunt regulator implemented by a resistor in series and Zener diode in shunt. This increases the output impedance of the amplifier, and also adds components. The ESPRIT instrument utilized the three-resistor network pictured in Figure 4.18. This resistor networked compressed the ±15 V input to a 0–5 V output. In order for this network to be accurate, smaller resistor values were used and knowledge of the exact voltage of the +15 V supply was necessary. The smaller resistor values created higher power consumption. For these reasons, the three resistor network was not used.

The input buffer and anti-aliasing filter required ±12 V in order to process the electrometer output correctly. This op-amp is different from the windowing stages, because of this higher voltage range. The LT1498 was used for this application. This op-amp is a dual op-amp with similar specifications as the LTC2051. The major difference between the two op-amps is that the LT1498 utilizes more power (about 2 mA per amplifier), and this is the reason for using the LTC2051(2) for the windowing stages instead of the LT1498(9) for all op-amps.

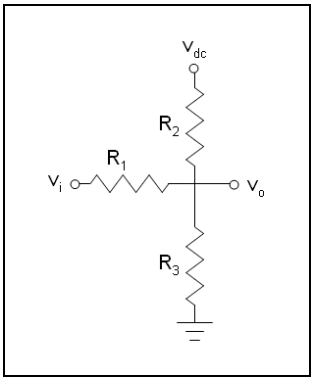

Figure 4.18 - ESPRIT resistor network.

The +5-V DC reference voltages to the summing and difference amplifiers are generated by a stable +5-V reference by Linear Technology's LT1461AIS8-5. This reference is highly accurate to within 0.04% tolerance, and has a very low drift with respect to temperature change of 3 ppm/°C. These references are used to provide the most accurate measurements with no error due to the wider variance of the +5-V bus voltage. Also, each supply input to the op-amp and reference voltages have a decoupling capacitor. These capacitors filter out any unnecessary high frequency signals.

To prevent a great effect from the input bias currents of the op-amps, resistors are added in series to the non-inverting terminals for the summing and inverting amplifiers. The value of these resistors is the equivalent resistance seen connected to the inverting terminals. Choosing the resistors in this manner creates the same voltage drop generated by the input bias currents.

The control and processing board is a four-layer board. When the signal conditioning circuitry was placed into layout, there were three different sections on the board: analog, digital, and mixed signal. The signal conditioning circuitry was placed in the analog section to provide isolation from the fast switching digital components. There were also two ground planes that were separated, and only connected at the ground input to allow a single point ground between the analog and digital components. Figure 4.24 illustrates the ground layer. The connection of the analog and digital grounds was made on the top layer. Probe 1 circuitry was placed on the top layer, and probe 2 components were placed on the bottom layer. All decoupling capacitors were placed within 0.02 in. of the supply input to each op-amp or reference voltage. The power for each op-amp was routed in the power layer.

4.5.2 Probe Bias Circuit

As mentioned previously, the probe bias is created by a digital-to-analog converter (DAC). The first step in choosing the correct DAC for this application was to determine the necessary resolution. The maximum sampling rate of the system is set to be 2080 samples per second. Since the data to be sampled is with respect to the bias voltage applied, then the step count of the DAC should at least match the sampling rate; therefore, a 12-bit DAC is sufficient.

ESPRIT utilized a 14-bit DAC; however, this resolution is not necessary. The next requirement investigated was the number of samples per second the device should be able to process, and this, too, is dictated by the sampling rate of the system. The DAC selected is the Analog Devices AD5530BR. This DAC provides an output range of –8.19 V to +8.188 V generated by the ±12 V supply and 4.096 V reference. The 4.096 V reference is the same series as the +5-V reference in the signal conditioning section; therefore, this reference is highly accurate. The communication protocol to the DAC is serial peripheral interface (SPI), which is a synchronous protocol. Three signals are sent from the microcontroller to the DAC: a clock signal, sync signal, and the data signal. Since there are two probes, there needs to be two sync lines, where one is for each DAC.

From the output of the DAC, there is a buffer that outputs to the electrometer. The reason for this buffer is to protect the DAC from any external failures. If, for some reason, the output to the electrometer is shorted or exposed to a higher voltage, then the buffer would fail first preventing any harm to the DAC. To provide a feedback reference, there is some signal conditioning that processes the DAC output to a 0–5 V range to be sampled by the microcontroller. With this loop, the probe bias can be calibrated to the instruction sent to the DAC. The op-amps utilized are the LT1499 and LTC2051 for the same reasons mentioned in the signal conditioning section. The op-amp configurations are an inverting amplifier and a difference amplifier. Figure 4.19 displays the schematic with the component values. The relationship of the output to the input for this reference feedback circuit is

$$v_o = \frac{5}{16} v_i + \frac{5}{2}. \qquad \textbf{EQ4-8}$$

This equation was derived from the necessary input to output relationships: ±8 V input and 0–5 V output. The component values in the figure are standard resistor values as before.

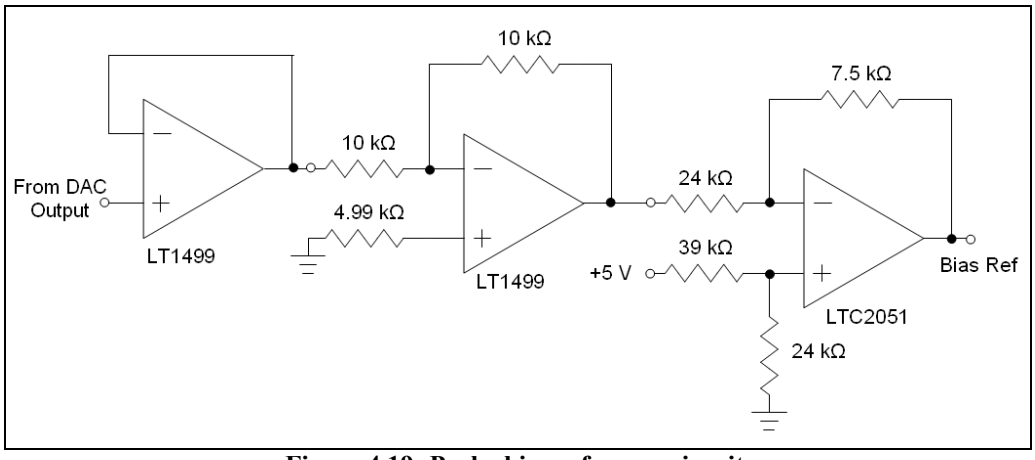

Figure 4.19 -Probe bias reference circuit.

The circuit was placed in the mixed signal area of the board, with the op-amp output closest to the electrometers. The grounding scheme for these components was on the analog ground plane; however, the DAC was kept away from the signal conditioning circuitry. The digital ground plane acts like a ridge in separating the signal conditioning section and the mixed signal section. Decoupling capacitors were used just as before to filter out any high frequency interference in the power bus. Probe 1 circuitry is on the top layer, and the probe 2 circuitry is on the bottom layer.

4.5.3 Microcontroller and Support Hardware Description

The microcontroller manages all of the processes of the instrument. The goal in choosing a suitable processor was to find one that is low cost and able to accomplish all of the needs of the mission. The Freescale MC9S12C32MFA25 was chosen. This microcontroller was chosen for all the support modules required for the design (i.e., SPI, ATD, etc.), and was utilized for the embedded microcontroller's course at Penn State taught by Professor Croskey a few years ago. The ESPRIT instrument utilized a PIC16F88 developed by Microchip. The reason for using the PIC for this mission was because: 1) this series of PIC was inexpensive, 2) the part was a SOIC, and 3) the only requirement of the microcontroller was to communicate to the DAC to create the sawtooth waveform.

The MC9S12C32MFA25 microcontroller is a 16-bit microcontroller. This part number coincides to the 32 kB of programmable flash memory and the 48-pin version. The 48-pin version is the smallest version of this microcontroller and was chosen in order to save board space and simplify the layout. This microcontroller can operate up to 40 MHz (Pierce Oscillator) and has up to 2 kbytes of RAM. The microcontroller is programmed via a single wire communication; however, it can also be programmed through the controller area network (CAN) bus as well. Table 4.7 summarizes its specifications. Every pin, except for two, is utilized in the design of the LP instrument. Thirteen pins are used for general purpose input/output (GPIO); eight pins are used for analog-to-digital conversion; two pins for asynchronous communications; four pins for serial peripheral interface, and the rest of the pins are used for the microcontroller support. First, the components necessary for the microcontroller support is discussed.

Table 4.7 - Specifications of the Microcontroller with the Values Used in Application

Specification	Value	Unit
Oscillator Frequency	25	MHz
Bus Clock	12.5	MHz
Flash Programmable Memory	32	kbytes
RAM	2	kbytes
Number of GPIO	13	---
Channels of ATD	8	---
ATD Resolution	10	bit
ATD Clock Intervals per Conv	16	clock cycles
ATD Clock Frequency	1.5625	MHz
Async COM Protocol	RS-232 or RS422	---
Async COM Baud Rate	115200	bps
SPI Resolution	8	bit
SPI Baud Rate	6.25	MHz

Crystal Oscillator

The microcontroller requires an input clock signal or oscillator in order to function correctly. The Pierce oscillator design was chosen because of the capability of higher frequencies. The Colpitts oscillator configuration can only go up to 16 MHz, while the Pierce oscillator is capable of 40 MHz. When choosing a crystal for space applications, the frequency tolerance should be small over the expected temperature range. The oscillators with the smallest

tolerance are the temperature-compensated crystal oscillators (TCXO). These oscillators may have stabilities over the range of –30 ˚C to 85 ˚C of down to 0.1 ppm. However, these oscillators are very expensive; therefore, a commercial-off-the-shelf crystal with small frequency deviations is used. The crystal chosen has the same footprint and load capacitance as the TCXO. The TCXO chosen is the Connor Winfield D53G-026.0, which has a center frequency of 26 MHz, stability of ±0.5 ppm, and load capacitance of 10 pF. This oscillator is priced at over $30 each; therefore, a commercial crystal with a similar frequency and low stability was chosen. The commercial crystal chosen was the Abracon ABM3B-25.000MHZ-10-1-U-T with a center frequency of 25 MHz, stability of ±10 ppm, and load capacitance of 10 pF. This crystal costs a little over $2 each, and is much more affordable for instrument prototype. These crystals are suitable for missions where the temperature range does not change greatly over the range of time, such as sounding rocket missions. For satellite missions, it is best to use the TCXOs. The closest commercial frequency crystal with low stability and similar load capacitance was 25 MHz; therefore, the software written has to be tweaked slightly for the greater frequency of 26 MHz for the TCXO.

To bias these crystals properly in the Pierce oscillator configuration, there are three external components required, feedback resistor and two load capacitors. The feedback resistor was chosen from the application notes of Abacron to be 1 MHz, so a 0603 package resistor is used between the crystal pins [*Abracon Corporation*, 2005]. To determine the load capacitance, any stray capacitance needs to be added to the total load capacitance. The crystal is connected to two pins on the microcontroller: EXTAL and XTAL, pins 21 and 22 respectively. From the data sheet, these two pins have a capacitance of 7 pF each bypassed to ground. If the crystal only required a load capacitance of 3.5 pF, then the two external load capacitors are not necessary. However, the necessary load capacitance is 10 pF for the selected crystal; therefore, the required capacitors need to be found. This is simply done by assuming that each load capacitor has the same value and a relationship can be found to relate to the total load capacitance

$$C_{\text{load}} = \left(\frac{1}{C_1} + \frac{1}{C_2} \right)^{-1} + C_{\text{stray}}, \text{ where} \qquad \textbf{EQ4-9}$$

$$C_1 = C_2 = C_{\text{ext}}, \text{ and}$$

$$C_{\text{ext}} = 2\left(C_{\text{load}} - C_{\text{stray}}\right). \qquad \textbf{EQ4-10}$$

Using equation **EQ4-10**, the required load capacitors each have a value of

$$C_{\text{ext}} = 13 \quad \text{pF}.$$

Figure 4.20 displays the schematic for the oscillator circuit. Using the Pierce oscillator configuration, there is one more task that needs to be done. The microcontroller requires a pull down resistor on the XCLKS pin, pin 13. This pull down resistor allows the microcontroller to function with the Pierce oscillator configuration.

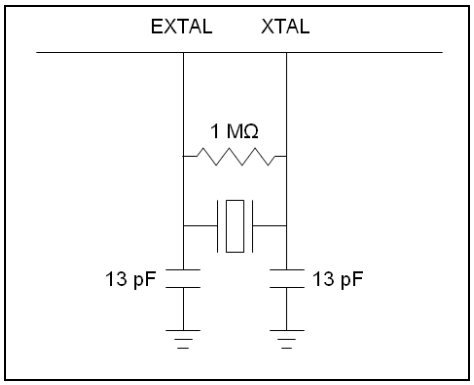

Figure 4.20 - Schematic of the oscillator.

Phase Locked Loop

The microcontroller also requires a phase locked loop (PLL) for timing purposes. The PLL filters the voltage controlled oscillator input ripple. This oscillator is the bus clock frequency (12.5 MHz), which is set at half the oscillator frequency. The phase locked loop component values and configuration is given in by the data sheet [*Freescale Semiconductor*, 2007]. The components are connected to the XFC pin, pin 19. Figure 4.21 displays the values and configuration for the components.

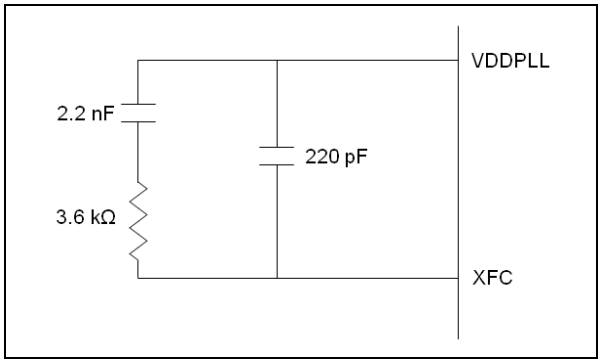

Figure 4.21 - Phase Locked Loop component values.

Power Supply

For the power supply to the microcontroller, there are four inputs that require a +5-V supply and six pins that are required to be grounded. The four inputs that require a +5-V input are: VDDR (pin 16), VDDA (pin 35), VRH (pin 36), and VDDX (pin 47). Each of these pins have bypass capacitors: one ceramic and one tantalum. The microcontroller also has an internal voltage regulator that regulates a bus of +2.5 V. There are bypass capacitors required to maintain this internal bus on pins VDD1 / VSS1 (pins 5 and 6) and VDDPLL / VSSPLL (pins 18 and 20). These capacitors are ceramic 0.1 μF and are placed between the two corresponding pins. The six pins that are grounded are VSS1 (pin 6), VSSR (pin 15), VSSPLL (pin 20), VPP (pin 23), VSSA (pin 37), and VSSX (pin 46). Table 4.8 summarizes the power supply requirements to the microcontroller.

Table 4.8 - Power Supply Pin Functions and Bypass Capacitors

Power Supply Pins	Pin No.	Voltage Supply [V]	Bypass Capacitors [µF]
VDD1	5	2.5	0.1 ceramic
VSSS1	6	GND	---
VDDR	16	5	0.1 ceramic and 10 tant
VSSR	15	GND	---
VDDPLL	18	2.5	0.1 ceramic
VSSPLL	20	GND	---
VPP	23	GND	---
VDDA	35	5	0.1 ceramic and 10 tant
VSSA	37	GND	---
VRH	36	5	0.1 ceramic and 10 tant
VDDX	47	5	0.1 ceramic and 10 tant
VSSX	46	GND	---

Programming

For programming the microcontroller, two pull-up resistors are required on the MODC/BKGD pin and RESET pin. The RESET pin is active low, and when set low, then the microcontroller will RESET to the start of the program code. The MODC/BKGD pin provides the single wire communication to the host. There are two interfaces for programming on the control and processing board. For prototyping and testing the board, there is a six-pin male header with the necessary pin-outs to interface to the development kit. For external programming from the box, the programming lines are connected to the female D-subminiature 15 connector J152.

GPIO Interfaces

The GPIO pins turn ON and OFF the different components and also determine if there is an external communication interface. The GPIO control the switches and relays to the probe clean and calibration board, the analog multiplexers, and high voltage DC/DC converter. The probe clean and calibration board is controlled by PT0, PT1, PA0, PT2, PT3, and PB4. The analog multiplexers are controlled by PT4, PT5, PT6, PT7, PM1, and PM0. The high voltage DC/DC converter is switched on by PP5. There is one digital input that enables the communication to go to the secondary line driver (see the Communication section). Table 4.9 summarizes the GPIO interfaces to the other components. All pins are set low during the initialization.

Table 4.9 - Microcontroller GPIO Pin Functions

Microcontroller Pin	Instrument Function
PT0	Probe 1 Relay 3
PT1	Probe 1 Relay 4
PT2	Probe 2 Relay 3
PT3	Probe 2 Relay 4
PT4	Probe 1 Mux pin A0
PT5	Probe 1 Mux pin A1
PT6	Probe 2 Mux pin A0
PT7	Probe 2 Mux pin A1
PB4	Probe 2 Relay 1 and 2
PE1	External COM Input
PA0	Probe 1 Relay 1 and 2
PM1	Housekeeping Mux pin A0
PM0	Housekeeping Mux pin A1
PP5	High Voltage DC/DC

Analog-to-Digital Converter

There are eight analog input channels available in the microcontroller. An internal analog multiplexer switches the eight inputs to the converter. The analog-to-digital converter (ATD) utilizes a successive approximation technique that performs a binary search for an accurate value at the input. The resolution of the ATD converter is 10-bit. This provides a resolution of about 5 mV for 0–5 V range.

In sampling the input, the ATD runs on its own clock, which is divided from the bus clock. The maximum clock rate allowable by the ATD module is 2 MHz, but the maximum frequency that can be generated by the 12.5 MHz bus clock is 1.5625 MHz. The fastest time is used in order to have the quickest measurements. In order to sample an input analog signal, the ATD first captures an initial value of the signal, where this takes two ATD clock periods. This signal is then sent through a buffer to a larger sampling capacitor at the input to the converter, and during the final sample period, the large sampling capacitor is connected to the input to provide feedback. *Almy* [2004] developed a concept of operations for the ATD in Figure 4.22.

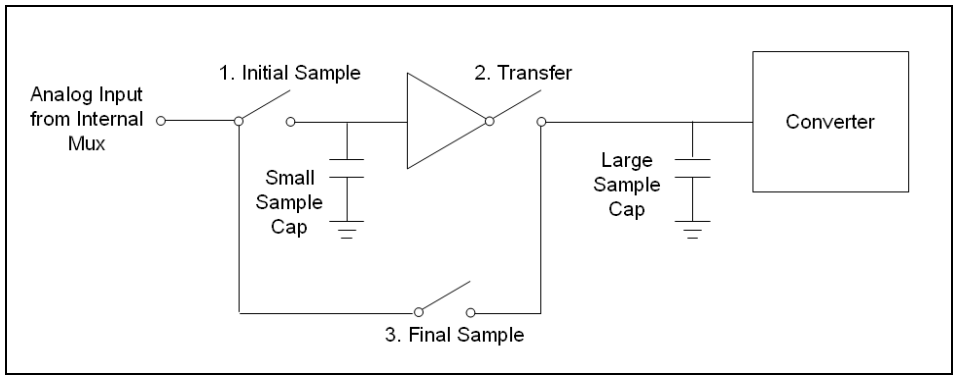

Figure 4.22 - ATD module sampling diagram [*Almy*, 2004].

To obtain one sample of the input, the ATD requires a sampling period, which ranges in duration by 2, 4, 8, or 16 clock periods. Longer sampling periods provide more accurate

solutions; however, the sampling period cannot be too long because this does not allow for high sampling rates. The sampling period chosen is 4 clock cycles with a sequence of 4 samples that are averaged together. A sequence of 4 samples means that the ATD module creates 4 unique samples of the input, but then these 4 samples are averaged together to provide one sample. Table 4.1 lists the 8 input analog channels with the corresponding pin number and signal being measured.

Table 4.10 - Analog Inputs to Microcontroller

Input Analog Channel	Microcontroller Pin No.	Measured Signal
AN00	27	Probe 1 Bias Reference
AN01	28	Probe 1 Full Range
AN02	29	Probe 1 Windowing
AN03	30	Probe 2 Bias Reference
AN04	31	Probe 2 Full Range
AN05	32	Probe 2 Windowing
AN06	33	Housekeeping Input 1
AN07	34	Housekeeping Input 2

Since there are more analog signals to be measured than the number of input analog channels available to the microcontroller, two four channel analog multiplexers are used for one channel each. Each multiplexer is for the windowing stages of each probe; therefore, if one multiplexer fails, then the other probe is not affected. The 4-channel analog multiplexer is the Analog Devices ADG704. This multiplexer requires at least two general purpose output lines in order for the signals to be switched. The device enable is an active high and is tied to the +5-V supply. The housekeeping lines are also taken through an analog multiplexer. There are seven different housekeeping lines to monitor; therefore, a multiplexer with more channels is used. The Analog Devices ADG709 is a dual 8-channel multiplexer that is connected to two inputs to the ATD. This multiplexer is controlled by two general purpose output lines as well. Table 4.9 lists the general purpose output corresponding to the multiplexer control lines.

Asynchronous Communication

The communication to the control and processing board is accomplished by the serial communications interface module (SCI). This module is known to industry as the universal asynchronous receive/transmit (UART) module. This module performs asynchronous communications, where, for the control and processing board, the two protocols implemented are RS-232 and RS-422. The two pins on the microcontroller that perform this communication are the RXD (pin 38) and TXD (pin 39) pins. These two pins are connected to line drivers that generate the necessary signals for the two protocols.

The control and processing board contains two sets of footprints for an RS-232 line driver and RS-422 line driver. There are two sets for communication to a flight computer and communication through an external interface for ground support equipment (see Figure 4.23). The communication protocol for the flight computer or ground support equipment can have different protocols. For example, the protocol to the flight computer can be RS-422 and the protocol to the ground support equipment can be RS-232. The correct parts have to be populated. The RS-232 line driver is manufactured by Analog Devices and is the ADM101E. The RS-422 line driver is also manufactured by Analog Devices, and the part number is the

ADM4856. The RS-232 line driver runs on a single +5-V supply and requires several bypass capacitors due to the on-board charge pump. RS-422 is differential; therefore, no charge pump is necessary to create the negative voltage. The RS-422 line driver does require a 120-Ω terminating resistor between the receive pins.

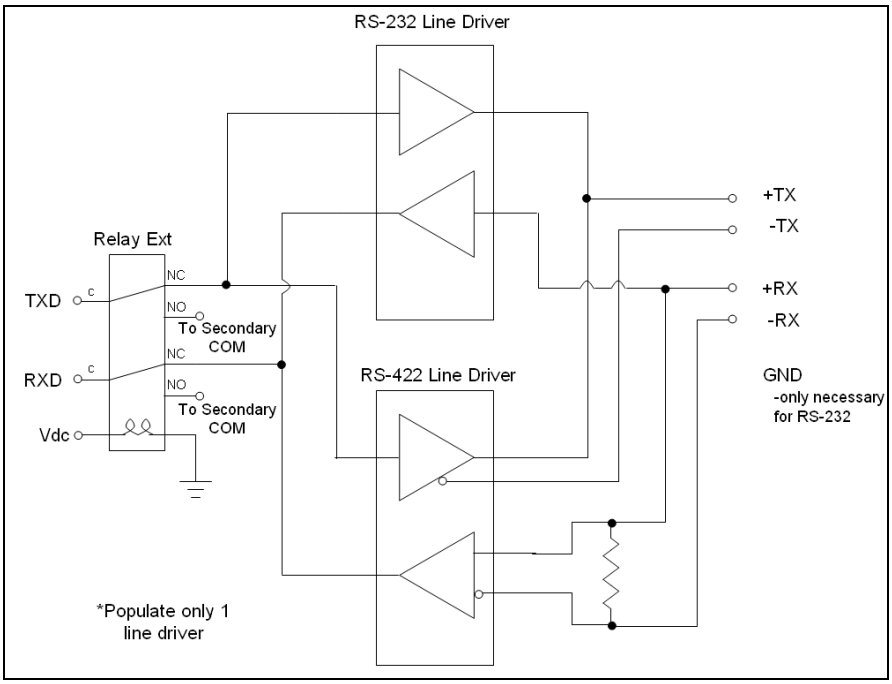

Figure 4.23 - Generalized schematic for async communication. There is a second set of line dirvers not shown in this figure for the secondary COM to the external interface. Only one line driver should be populated for each: flight computer COM and external COM.

There is only one SCI module on the microcontroller; therefore, there is a relay that switches between the flight computer communications and the ground support equipment communications. The baud rate is set for 115200 kbps with a percent error of 3.12%, which is within the range of error of typical UARTs of 5%. For the SCI module, the maximum percent error for reception is 3.75%, and the percent error for the 115200 kbps baud rate is within this range. The calculation of the specific baud rate is explained in the software section.

Serial Peripheral Interface

The serial peripheral interface (SPI) provides the communication to the two DACs to create the probe bias. SPI requires three wires for open loop communication to the DAC. The three lines are a clock signal, data signal, and sync line. These signals correspond to the SCK (pin 40), MOSI (pin 41), PM3 (pin 42), and PM4 (pin 43). The PM3 and PM4 pins correspond to the two sync lines, where one is for each DAC. The SCK and MOSI pins are connected to both DACs in parallel. The sync lines go to each DAC, and they are active low, so these lines idle high.

The goal of this communication is to provide the fastest link between the microcontroller and the DAC. The clock signal is set to be 6.25 MHz, which is the maximum signal capable of the microcontroller. The DAC can take up to a 7-MHz clock signal. A high clock rate is used in order to obtain the fastest data transfer possible to gain more processing time for the microcontroller. With the clock rate set, the polarity and phase of the clock signal need to be

defined. The DAC defines these requirements. The polarity is set such that the clock idles low, and the phase is set, where sampling occurs on the falling edge of the clock signal. The data sent to the DACs are sent as two bytes. The data format is defined by the datasheet, and the software handles this transmission. The sync line enables the specific DAC to accept the data transmission sent. The sync line is active low and is set low before data transmission.

4.5.4 Practical Design Considerations

There are several low noise design techniques employed in the development of the board. If regulated power is supplied to a board from an external regulation source, then bulk capacitors are required at the supply inputs. For the control and processing board, the power supply inputs all contain tantalum bulk bypass capacitors. These bulk capacitors prevent any power surges due to transients. The value of these bulk capacitors should be at least 10 times the sum of the total capacitance of all the bypass capacitors on the board. Since these capacitors are tantalum, the voltage rating of the capacitors has to be at least twice the operating voltage, which includes any voltage ripple.

This board has four layers with the two inner layers being ground and power layers. The board has been separated into three different sections: analog, digital, and mixed signal. This separation allows for less interference to the sensitive analog components. Figure 4.24 illustrates the two separate ground planes. The ground layer is separated into two ground planes: one for analog and the other for digital circuitry. These two ground planes are connected on the top layer at the ground supply input. The footprint of the microcontroller itself has a divided ground plane on the top layer. This footprint was taken from the suggested printed circuit board footprint from Freescale. The divisions on the divided ground plane isolate the ground pins for the different modules on the microcontroller. Figure 4.25 displays this copper area underneath the microcontroller.

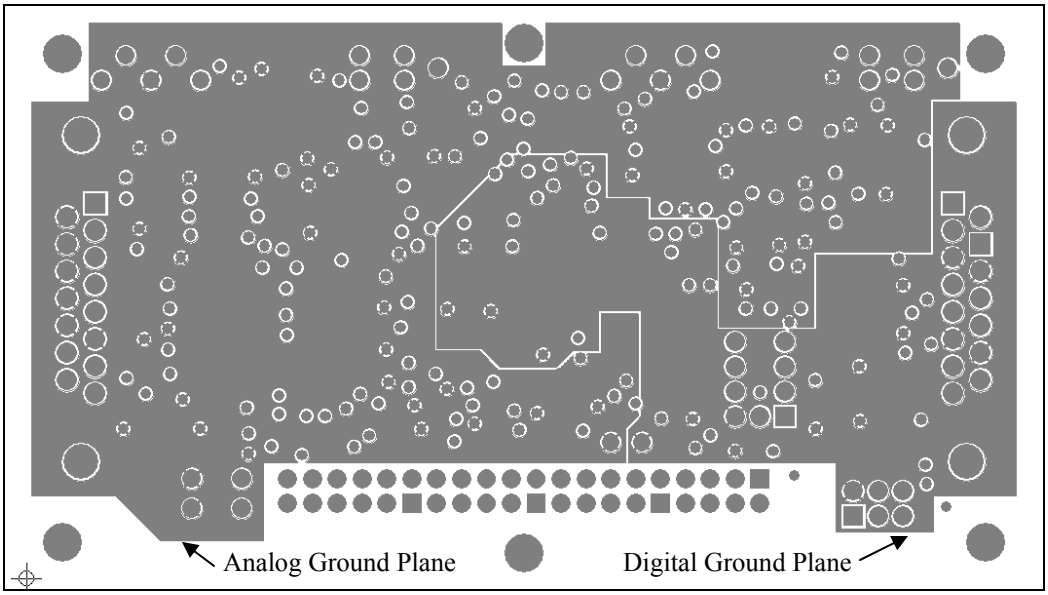

Figure 4.24 - Plot of ground plane of the control and processing board displaying the separation between the analog ground plane and the digital ground plane.

When routing the board, caution should be taken on the location of the traces. Routing the power layer should not create any loops, and the power to the digital components should not

be shared by power to the analog components. On the board, both the analog and digital power supply lines are only connected at the power supply inputs. When routing analog signals, the traces should not be placed near the fast switching digital circuitry. There are no analog traces or components underneath the microcontroller.

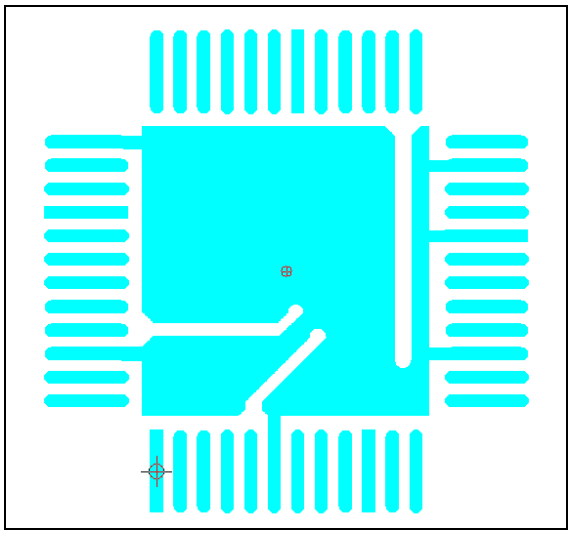

Figure 4.25 - Footprint of the microcontroller with pin 1 marked by the crosshairs.

4.5.5 Board Interfaces

There are four primary connectors to interface to the board. There are two D-subminiature (D-sub) 15-pin connectors, a six-pin male header, and a 40-pin female header. The two D-sub 15-pin connectors have different genders to avoid any confusion for external interface to the spacecraft harness. The male connector P153 in Figure 4.2 provides an external power input, analog data output, and ground support equipment enable input. This connector allows the board to be powered externally without the power regulation board. If this interface was used to power the board, then there is no high voltage bias for the probe clean operation. The analog data output is for the bias reference and full range amplifier. The ground support equipment enable requires a +5-V power supply and +12-V power supply to activate the on-board relay for external communications. The +5-V input also goes to an opto-coupler that signals the microcontroller that the communications relay is switched.

The second D-sub 15-pin connector J152 is a female connector that outputs all the digital communication lines. The RS-232 and RS-422 interfaces go through this connector. This connector also provides a programming interface with the +5-V supply line required to power on the microcontroller for programming. Since the RS-422 protocol is differential, these lines have to be twisted pair. There have been cases for loss of communication simply due to the communication lines not being twisted pair. The twisted pair lines reduce inductive crosstalk and any common mode noise. The six-pin male header is also for programming, and either interface can be used. This 6-pin header interface allows for easy prototyping and development with the microcontroller development kit.

The connector that connects the control and processing board to the power regulation board is a series of headers. There are two female headers with each connected to one of the boards. Then a male header is placed in between in order for the connection to be made between the two boards. Figure 4.6 displays this interface between the two boards. The reason for this

type of interface is to remove the possibility of any header pins getting bent or broken. This header allows the power lines and housekeeping lines to go from the power regulation board to the control and processing board. The high voltage DC/DC converter enable signal also goes through this connecter from the microcontroller to the relay on the power regulation board.

The electrometer board and probe clean and calibration board interface is done by wire connections. The wire connections connect the control and processing board to the bolt-in filters. There are 20 solder hole locations on the control and processing board for this interface. These holes are located opposite to the header. Figure 4.26 is a photograph of the top of the board with populated components.

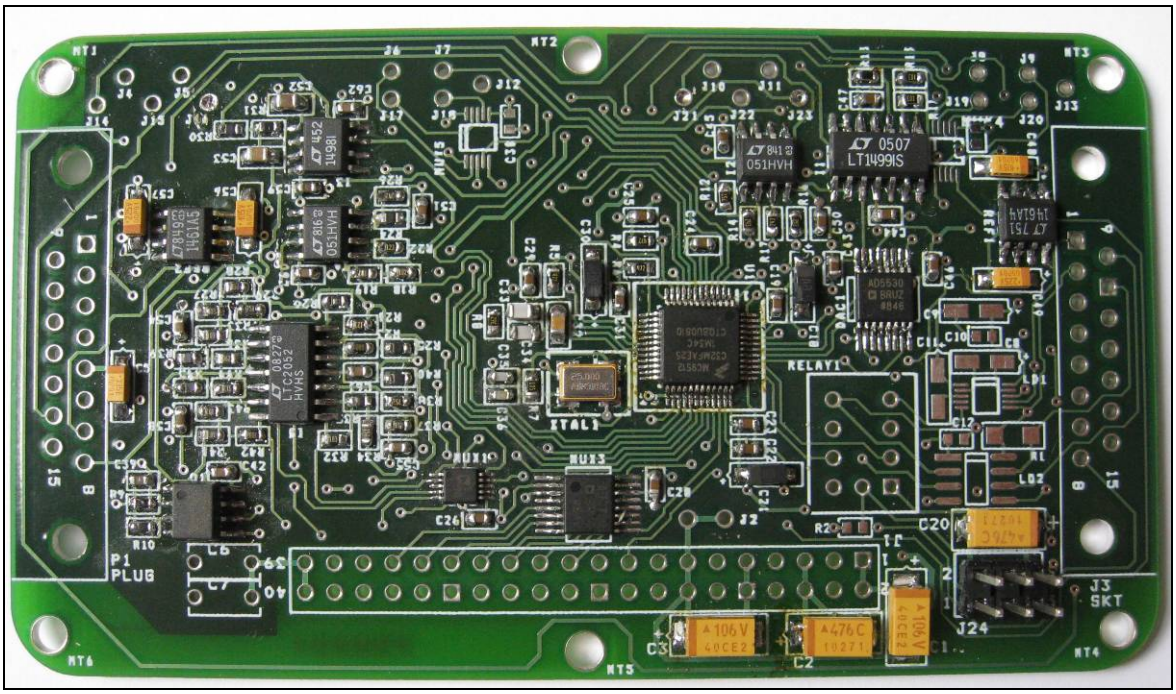

Figure 4.26 - Top view of the control and processing board.

4.6 Power Regulation Board

The power regulation board generates the necessary power inputs from a single unregulated DC source. The regulation board generates the following DC voltages: +12-V, +5-V, –12-V, and +150 V. The allowable power input range of the regulation board is from +15 V DC to +36.5 V DC. Table 4.11 lists some specifications of the power regulation board.

Table 4.11 - Maximum Ratings of the Power Regulation Board

Specification	Value
Input Voltage Range	15–36.5 V
Input Current Range	0–0.5 A
+12-V Maximum Current*	0.933 A
+150 V Maximum Current	1.6 mA

*This is the maximum current allowed for a +28 V input voltage. The maximum current for the +5-V and –12-V supplies are included in the +12-V maximum current value, since these regulators are supplied by this bus. The nominal values of current are listed in the testing section.

The board regulates the three DC bus voltages by using two switching regulators and a linear regulator. The issue with using just linear regulators is the loss in efficiency. Linear regulators use the power difference between the input and output and dissipate the power as heat. If the power requirements for the instrument are for very low power, then linear regulators are the best, since the design is simplified. With switching regulators, the power efficiency is much higher; however, there is noise that is generated from the instantaneous current rushes during switching. Filtering this noise takes a lot of engineering to remove its effects. Filters are necessary at the input and output of the switching regulators. Most designs include passive components; however, these components can be large and take up a lot of board space. An alternative solution was found in order to eliminate the switching noise. The noise is both radiated and conducted, and certain precautions need to be implemented for each case. The noise is a factor for both the input and output of the DC/DC converters.

4.6.1 Voltage Regulators

The two DC/DC converters are for the +12-V and –12-V bus. The linear regulator creates the +5-V bus using the +12-V bus. The DC/DC converters are modules from Texas Instruments that are output adjustable: the PTN78000W (+12-V output) and the PTN78000A (–12-V output). These modules are chosen for their small package, as well as the capability to adjust the output voltage. The PTN78000W also offers a wide input range of 15–36.5 V. The –12-V regulator runs off of the +12-V bus. The +5-V bus is generated by using the National Semiconductor linear regulator LM340AT-5.0. The linear regulator is used, because the regulator provides further ripple rejection from the input bus of 80 dB. Using a +5-V linear regulator after the +12-V switching regulator is more efficient than placing the +5-V linear regulator at the unregulated input just as the +12-V switching regulator. Also, only about 30 mA maximum is required for the +5-V supply. With this low of a power requirement, the trade off of efficiency for complexity is no longer valid; therefore, the +5-V linear regulator is used. The maximum requirements for each regulated bus are in Table 4.11. The detailed design of each regulator with supporting components is not explained in this thesis, because the design is taken straight from the datasheet utilizing the same components. The required programming resistors to set the voltage are found during prototype testing (see Section 6.4).

4.6.2 Filtering

Each DC/DC converter utilizes both passive and active filtering components. The passive filtering network consists of the recommended pi-filtering network in the datasheet (see Figure 4.27). The pi-filter is a low pass design with two shunt capacitors and a series ferrite bead. This passive filter is designed to remove at least 20 dB of noise power at the switching frequency of about 500 kHz. To remove the remaining ripple voltage the active filters are used. Using these filters decreases the efficiency of the power system, but this provides the benefit of less electromagnetic interference. The efficiency is still better than that of a linear regulator.

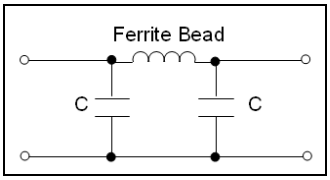

Figure 4.27 - Low-pass pi-filter.

The active filters are made by Picor, a subsidiary of Vicor, and are attached at the inputs and outputs of the DC/DC converters. The input and output filters are the QPI-3LZ and QPO-1LZ respectively. The input filter has specifications to eliminate the noise by at least 70 dB for common mode noise and 80 dB for differential mode noise for the specified switching frequency stated above. There are only three component requirements for the input filter: two shunt capacitors and an in-line inductor. The first capacitor is placed at the input across the unregulated bus and star ground reference. This capacitor has to be polarized with a value of 47 μF. The working voltage of the capacitor has to be at least twice the voltage across the terminals; therefore, finding a commercial-off-the-shelf capacitor that operates in a vacuum environment may be difficult. The capacitor selected was the Tantalex wet tantalum series by Vishay Sprague. These capacitors are hermetically sealed with a working voltage of 75 V. The second capacitor must be of the same type and is connected at the output of the QPI-3LZ. The inductor is connected between the input star ground and the instrument ground bus. In determining the inductor for this application, the resistance across the terminals is chosen to be very small. The inductor used is 5 μH with an inline resistance of 26 mΩ, which is equivalent to 19.3 in. (49.1 cm) of 22 AWG wire; therefore, this inductor meets the requirements. Sometimes the wire harness for a spacecraft is longer than this; therefore, this resistance is tolerable. The input filter also has pins that require a copper area in order to dissipate heat; therefore, during board layout two separate areas were set aside to provide enough copper area to allow the heat to be dissipated. The general schematic is in Figure 4.28.

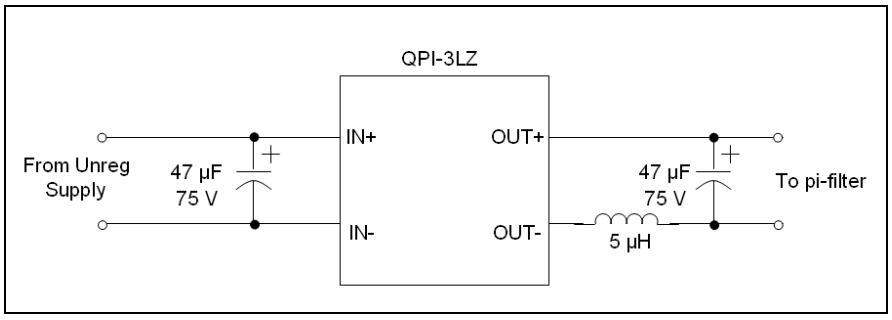

Figure 4.28 - Generalized schematic of the input active filter.

The output filter requires a little more engineering. The QPO-1LZ requires external components in order to set the desired attenuation at a certain switching frequency. These components are resistors with a specific value that corresponds to the desired operation. The output filter was set to have the maximum attenuation at the switching frequency; however, the greatest attenuation occurs with the greatest voltage drop, or head-room, across the output filter. This decreases the efficiency of the power system, but attenuates the noise greatly with at least 50-dB attenuation. The head-room was set to 0.5 V; therefore, the output of the DC/DC converter should be +12.5 V. The headroom resistor, R_{HR}, programs the output filter to set the desired headroom and, therefore, attenuation. To attain a headroom of 0.5 V, a headroom resistor of R_{HR} = 59 kΩ was used. Regarding bypass capacitors, two are required at the output and for an internal reference. The bypass capacitor for this internal reference voltage is optional, but adds further attenuation to the voltage ripple. The output capacitor is ceramic and, therefore, the working voltage of the capacitor does not need to be two times the actual voltage drop. The capacitor is formed from two 6.8 μF capacitors stacked up on each other.

The last task to complete the design is to disable the peak detect module and slope adjust module. The peak detect module determines the appropriate headroom for the associated amplitude of the voltage ripple. The maximum ripple attenuation is desired; therefore, the headroom needs to stay at a maximum. To turn off the peak detect module, a simple RC low pass filter is required at the input. The figure below displays this. The slope adjust module varies the headroom voltage due to power consumption change. The change in power consumption is not great during mission operations, and the greatest attenuation of the voltage ripple is the goal; therefore, the slope module is turned off in order to allow the greatest attenuation. A resistor value programs the slope adjust feature in the same way that the headroom resistor did. The slope adjust resistor value is R_{SA} = 100 kΩ. Figure 4.29 is a schematic for the output filter. The footprint for both the input and output filters is a land grid array (LGA); therefore, solder paste and a reflow oven are required to mount these components on a board.

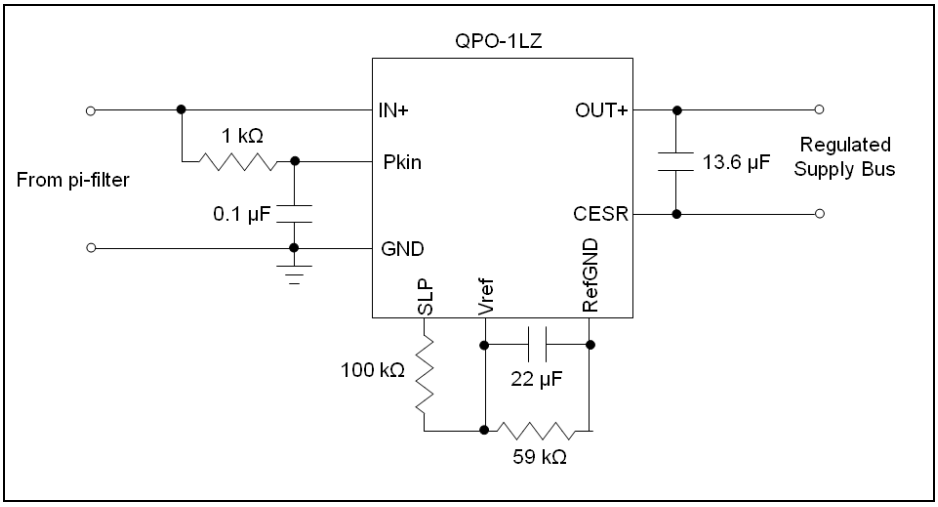

Figure 4.29 - Schematic of output active filter.

4.6.3 High Voltage Switching Regulator

The high voltage DC/DC converter is used for the probe clean phase of the mission. If a mission does not require the probe clean mission operation, then the components associated with the high voltage DC/DC converter do not need to be populated. As stated in Section 3.1, the voltage required on the probe is +150 V. The high voltage regulator chosen is the EMCO Q03-12SA because of its small package, copper housing, and non-outgassing properties. The package is the size of $0.5 \times 0.5 \times 0.5$ in. cube. This small size saves board space. The copper housing attenuates the radiated EMI. As shown in Section 4.6.5 below, the copper housing provides absorption loss and reflection loss of the radiated EMI. The non-outgassing characteristic is good for space applications, so that other components or instruments are not contaminated due to venting of the instrument. The output of the DC/DC converter is dependent on the input voltage level. There is a linear relationship between the input voltage and output voltage. The maximum voltage of the DC/DC converter is 300 V, and the maximum input voltage is 12 V; therefore, 150 V can be attained by using a 6-V input. This voltage is not available though. A designer could have chosen the 24 V version so that a 12 V input would provide a 150 V output, but doing this does cause one problem. External series resistors cannot be used for regulator protection and filtering. This is discussed later in more detail.

The DC/DC converter does operate at the full voltage of 300 V with the 12 V input. External components create the desired output voltage of 150 V. First, in high voltage designs, a resistor in shunt at the output is necessary, because if the device is turned off or switched from the load, then the output to the DC/DC converter needs to dissipate the output power. This resistor in shunt is called a bleeder resistor. The recommended value for the bleeder resistor is a resistance that only utilizes 10% of the output current capacity. For the Q03 series, the current capacity is 1.6 mA; therefore the following resistor values for the bleeder resistors are used: two 931-kΩ resistors in series. Next, to obtain the desired voltage of 150 V, a Zener shunt regulator is implemented at the output. The shunt regulator is composed of a series resistor and a 150-V Zener diode in shunt configuration. The Zener diode has to be able to handle the current. The resistor value is determined by calculating the resistance required for protection from a short circuit situation. During the testing and integration phase, if the probe were to come into contact with any of the spacecraft surface, then a short circuit would occur. Two 422-kΩ resistors are stacked in parallel in order to obtain an equivalent resistance of 211 kΩ in order to prevent any short circuit damage. In vacuum applications, arcing may occur, and these inline resistors also help prevent any damage due to current overloads. Using the values of the bleeder resistors, series resistors, and housekeeping resistors, the short circuit current would be 1.583 mA, which is 98.9% of the rated capacity. There is one last component at the output to lower output ripple, and this is a shunt capacitor to create a simple RC low pass filter. This capacitor is a 0.2-µF ceramic capacitor that provides a cutoff frequency of 3.77 Hz. This output capacitor also helps stabilize the output. The input of the Q03 requires a bypass capacitor, and a tantalum capacitor with a value of 10 µF is used. Figure 4.30 illustrates a generalized schematic for the high voltage DC/DC converter.

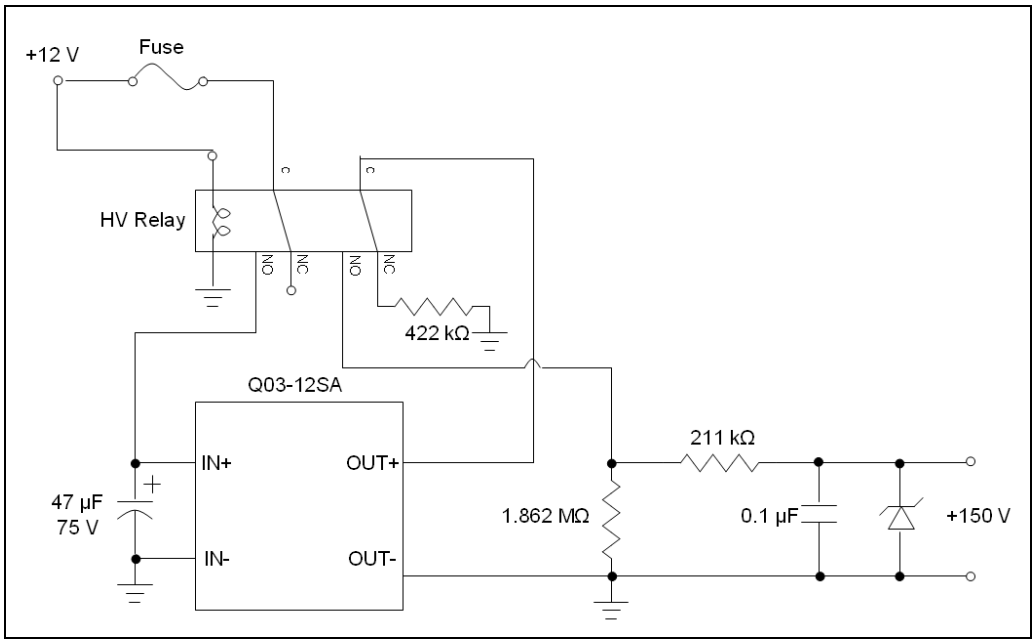

Figure 4.30 - Schematic of high voltage regulator.

There are a few other considerations necessary for a practical design. The DC/DC converter requires the ability to be turned on and off by the microcontroller and other power system protection techniques. The regulator is switched on and off by a DPDT mechanical relay

by Teledyne Relays (the 136C series – the same as the probe clean and calibration board). The relay switches on and off both the input and outputs of the regulator, leaving it isolated from the +12-V power supply and control and processing board during the off state. During the off state a bleeder resistor is connected to the NC pin. This allows the output of the regulator to discharge during the off state. An input fuse also exists prior to the relay to protect the system from any over current by the regulator. Lastly, when choosing resistors for a high voltage design, the type of resistor needs to be taken into account. The resistor can meet the requirements for the expected power dissipation, but non-ideal effects may still occur. The designer needs to be aware of the working voltage of the particular resistor. Permanent changes to the resistance may also occur if the correct resistor with the proper working voltage is not chosen. Table 4.12 summarizes the probe clean high voltage regulator specifications.

Table 4.12 - High Voltage Regulator Specifications

Specification	Value
Switch Frequency	300 kHz
Maximum Regulator Current	1.6 mA
Short Circuit Current	1.583 mA
Maximum Probe Current	0.711 mA

4.6.4 Power System Protection

All power systems should require voltage and current protection. At the input of the power regulation board, there is a Schottky barrier diode and a fast blow fuse. The Schottky barrier diode prevents any damage by putting negative voltages at the input. The fuse prevents any over current draw. The maximum continuous current the fuse is capable of is 500 mA. Diodes are also used between the +12-V output and the +5-V input, so that some of the power can be dissipated through these diodes and not entirely through the linear regulator. This reduces the temperature to the heat sink of the linear regulator.

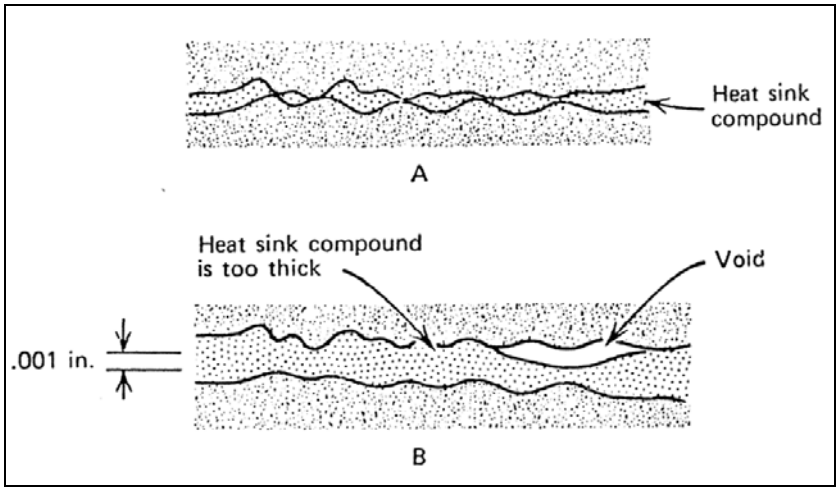

Figure 4.31 - Comparison between proper application and excessive application of the thermal compound [*Scott*, 1974].

The heat sink of the linear regulator is mounted to the side of the box in order to dissipate heat efficiently. Thermal paste and a thermal pad are used to both isolate the heat sink electrically and provide good thermal conduction. When applying the thermal paste, make sure

not too much is used, because the thermal conduction may decrease due to the development of voids in the application. Figure 4.31 illustrates the difference between proper application of the thermal compound and excessive application of the compound. The regulator is held in place by a nylon screw and nut to provide no electrical conduction of the heat sink to the box. Figure 4.32 displays a photograph of the mounted linear regulators used for ESPRIT.

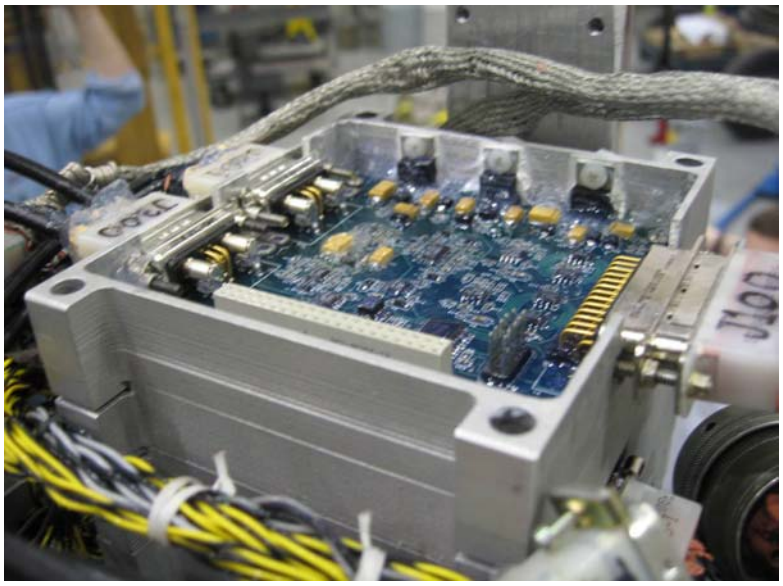

Figure 4.32 - Photograph of the power and processing board for ESPRIT. Note the mounting of the linear regulators to the box.

To prevent an over-voltage input from damaging the power system, an over-voltage crossbar can be used. This was not used though because of the non-ideal current sink. When there is an over-voltage, the Zener diodes can sink up to 1 A or greater. This would put a strain on the power supply and may disrupt other instruments connected to the same supply bus.

4.6.5 EMC Considerations

The filters mentioned in Section 4.6.2 lower the conducted EMI. To further lower the total EMI effects, the radiated EMI needs to be taken into account. This is where board routing design and shielding need to be investigated. The ground layer is separated by different copper areas corresponding to each regulation circuitry and then tied to the central point that goes through the inductor to the star reference. Figure 4.33 illustrates the ground layer. The traces between the ground plane and the single point ground are thin in order to create a higher impedance to improve the isolation. Other routing considerations include no routing of power lines adjacent to each other in order to reduce crosstalk.

To mitigate the effect of the radiated EMI, component shielding is necessary. The high voltage DC/DC converter already comes with copper shielding; therefore, this component does not need to have any additional shielding. The other two switching regulators require a small box encasing them. The encasing is 5-sided and composed of copper, and there is a ground plane on the top layer that further encloses the switching regulators on the 6th side. The emitted radio waves penetrate and attenuate into the shielding metal.

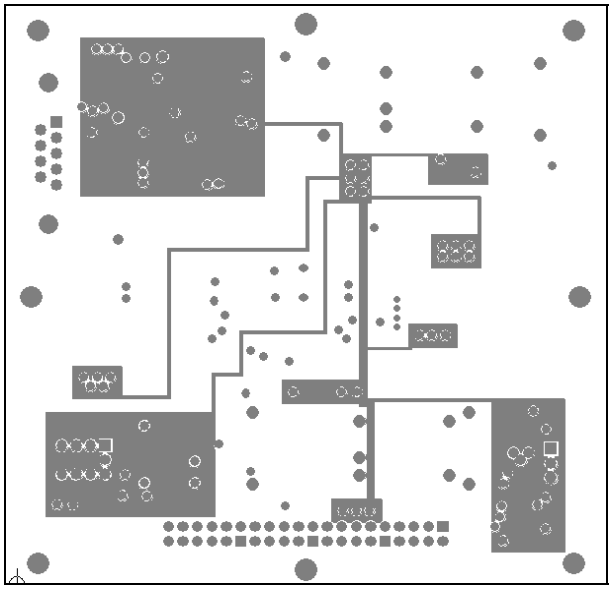

Figure 4.33 - Ground layer of the power regulation board.

The skin depth, δ, is a parameter for the radio wave penetration into a conductor. The skin depth is the depth of penetration at which the radio wave amplitude decreases to $1/e$ (37%) of the incident amplitude. The skin depth parameter for a conductor has the following relationship

$$\delta = \sqrt{\frac{1}{\pi f \mu \sigma}}, \qquad \textbf{EQ4-11}$$

where f is the radio wave frequency, μ is the permeability, and σ is the conductivity. For a copper material in mils, the skin depth is

$$\delta = \frac{2.6}{\sqrt{f_{\mathrm{MHz}}}}, \qquad \textbf{EQ4-12}$$

and for a copper material in cm,

$$\delta = \frac{0.0066}{\sqrt{f_{\mathrm{MHz}}}}. \qquad \textbf{EQ4-13}$$

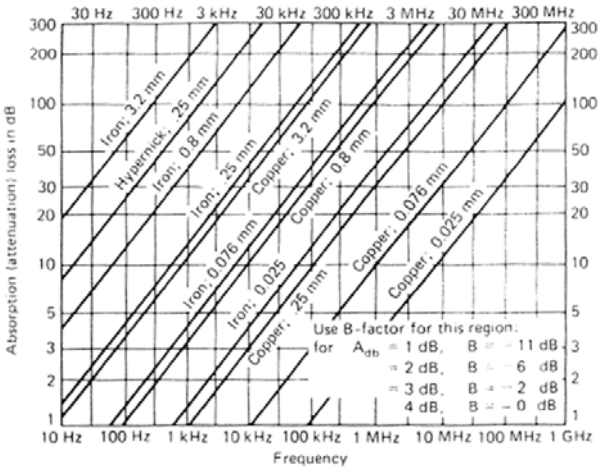

Figure 4.34 - Graph displaying the absorption loss versus frequency for various thicknesses [*Violette et al.*, 1987].

The skin depth alone does not explain the emitted radio wave characteristics. As mentioned previously, there are two types of attenuation associated with radiated EMI: absorption and reflection. Absorption loss is attenuation while the radio wave is within the conductive medium. *Violette et al.* [1987] determined a quantitative relationship for the absorption loss

$$A_{\text{dB}} = 8.686t\sqrt{\pi f\mu\sigma}\,, \qquad \textbf{EQ4-14}$$

where t is the thickness [*Violette et al.*, 1987]. Figure 4.34 displays the absorption loss for three metals utilizing the equation above. The relationship demonstrates that, with an increase in thickness, then there is greater absorption loss; however, the encasing should not be too thick, because this increases mass and complexity to fabricate.

The second type of attenuation is reflection loss. This is the loss of the radio wave associated to the reflection at two different boundaries. Electromagnetic boundary conditions apply, and an expression for reflection loss can be easily derived from Maxwell's equations

$$R_{\text{dB}} = 20\log_{10}\left[\left(\frac{Z_m}{4Z_w}\right)\left(1+\frac{Z_w}{Z_m}\right)\right], \qquad \textbf{EQ4-15}$$

where Z_m is the metal impedance and Z_w is the radio wave impedance at the interface [*Violette et al.*, 1987]. This expression is further simplified to

$$R_{\text{dB}} = 108.1 - 10\log_{10}\left(\frac{\mu_r f_{\text{MHz}}}{\sigma_r}\right) \qquad \textbf{EQ4-16}$$

for the far field, and for the near field

$$R_{\text{dB}} = 56.6 - 10\log_{10}\left(\frac{\mu_r f_{\text{MHz}}}{\sigma_r \eta}\right), \qquad \textbf{EQ4-17}$$

where σ_r is the relative conductivity to copper, μ_r is the relative permeability to copper, and η is the free space intrinsic impedance. Figure 4.35 displays the reflection loss for the same three metals. The values found in this figure are only valid for a thickness greater than three times the skin depth, $t > 3\delta$. The reason for this is due to multiple reflections at the wall-to-free space interface upon exiting the wall. If the thickness is too small, then the third reflection and every

odd reflection add to the transmission radio wave. *Violette et al.* [1987] determined an approximation for the multiple reflections

$$B_{\mathrm{dB}} = 20\log_{10}\left(1 - e^{2t\sqrt{\pi f\mu\sigma}}e^{2jt\sqrt{\pi f\mu\sigma}}\right). \qquad \textbf{EQ4-18}$$

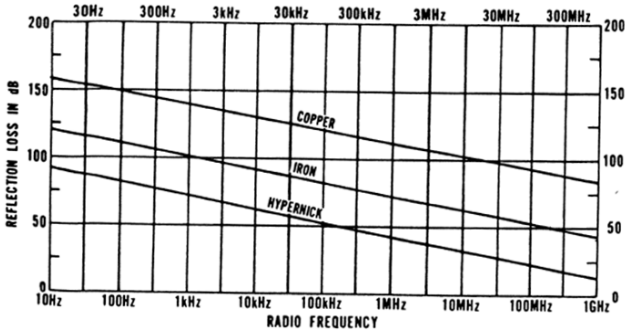

Figure 4.35 - Reflection loss as a function of radio frequency [*Violette et al.*, 1987].

The wall should be thick enough to disregard these multiple reflections; therefore, by having a wall thickness of at least three times the skin depth, this term can be neglected.

With the requirement for the thickness of the enclosure to be at least three times the skin depth, $t > 3\delta$, the enclosure dimensions can be determined. The skin depth for copper at the switching frequency of 500 kHz was found to be

$$\delta = 3.677 \ \ \mathrm{mils} = 0.003677 \ \ \mathrm{in.},$$

hence,

$$3\delta = 11 \ \ \mathrm{mils}.$$

Some DC/DC converters have lower switching frequencies, typically 100 kHz, and the minimum required thickness for these converters would have to be

$$3\delta_{100\,\mathrm{kHz}} = 25 \ \ \mathrm{mils}.$$

A thickness of 1/32 in. (0.8 mm) was chosen for this reason. With this thickness chosen, there is an absorption loss of at least 50 dB and reflection loss of at least 120 dB. The total loss is

$$L = A_{\mathrm{dB}} + R_{\mathrm{dB}},$$

which gives

$$L = 170 \ \ \mathrm{dB}.$$

This design greatly reduces the radiated EMI. The reflection loss alone probably would suffice in any design. The thickness for any enclosure needs to be at least three times the skin depth.

4.6.6 Housekeeping

The housekeeping circuitry monitors the voltages, current, and temperature of the power regulation board. The voltages monitored are: the input unregulated supply, the +12-V supply, the +5-V supply, the –12-V supply, and the +150-V supply. There is only one current monitor and temperature monitor, where the current monitor is for the input unregulated supply, and the temperature monitor is for the +5-V linear regulator. These seven monitors are sent to the analog multiplexer on the control and processing board to be sampled by the ADC.

The voltage monitors utilize similar op-amp configurations as the signal conditioning circuitry. Table 4.13 lists the specifications of the voltage monitors. A couple of the voltage monitors are just voltage dividers with a buffer, where R_1 is the series component of the voltage divider, and R_2 is the shunt component. The +12-V voltage supply has both a voltage divider

stage and a difference amplifier stage. The reason for this is to lower the voltage such that the input voltage seen at the second op-amps terminals is within the 0–5 V range.

Table 4.13 - Summary of Voltage Monitoring Circuits

	Bus Voltage	**+12-V Bus**	**+5-V Bus**	–12-V **Bus**	**+150 V Bus**
Input V_{min} [V]	10	9.5	0	–14.5	0
Input V_{max} [V]	40	14.5	10	–9.5	305
Slope: A	–1/6	–1	1/2	–1	1/61
Intercept: B	5/3	14.5	0	–9.5	0
Amp Type	Diff.	V. Div / Diff.	V Div.	Summing	V. Div.
R_1 [Ω]	12 k	(2 k + 1.8 k)/ 1 k	2 k	2 k	3 × 2 M
R_2 [Ω]	2 k	1k / (2.4 k + 2.4 k)	2 k	2 k + 1.8 k	100 k
R_3 [Ω]	14 k	--- / 2 k	---	2 k + 1.8 k	---
R_4 [Ω]	5.6 k	--- / 2 k	---	2 k	---

The current monitor utilizes a Hall-effect sensor to measure the current. The sensor is the Sentron CSA-1V-SO, which is a surface mount SOIC-8. For small current applications (I < 1 A), multiple traces need to be routed underneath this component in order for the magnetic field to be large enough to measure. Figure 4.36 illustrates the necessary routing for the current sensor. Five traces 12 mils thick were routed underneath the current sensor. The thickness of the traces depends on the amount of current that goes through the trace. The appropriate trace width can be found in a reference table. These reference tables are available from any printed circuit board manufacturer. For a trace width that is 12 mils thick for a 1 oz. copper weight, the maximum amount of current is 1.01 A. The trace width should not be too small either, because this gives rise to a higher resistance and a voltage drop across the length of the trace. The output of the current sensor is differential, and the output is sent to an instrumentation amplifier that is similar to the instrumentation amplifier in the electrometer, the Analog Devices AD623BR. The CSA-1V has the following relationship for the differential voltage output to the current,

$$V_{\text{diff}} = (35 \text{ mV/A})(\#\text{ of traces})I, \qquad \textbf{EQ4-19}$$

hence,

$$V_{\text{diff}} = (175)I \text{ mV}. \qquad \textbf{EQ4-20}$$

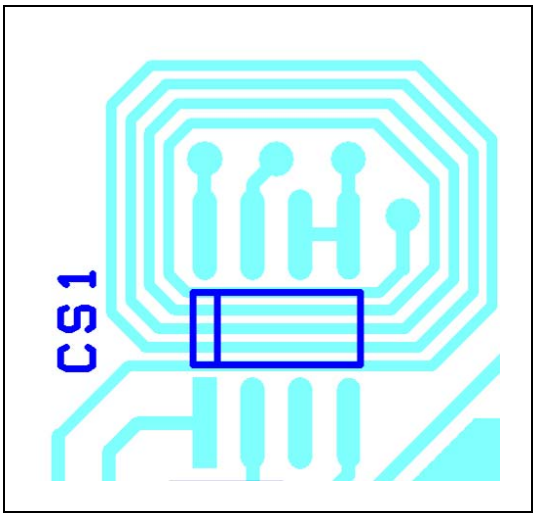

Figure 4.36 - The routing required for the current sensor.

With the knowledge of the voltage relationship, the gain for the instrumentation amp is determined. The gain of the AD623BR is limited to

$$G_{\max} = \max\begin{Bmatrix} 2(V_+ - 0.7 - V_{CM})/V_{diff} \\ 2(V_{CM} - V_- + 0.59)/V_{diff} \end{Bmatrix}, \qquad \textbf{EQ4-21}$$

where V_+ is the positive voltage supply to the amp, V_- is the negative supply or ground, and V_{CM} is the common mode voltage. Whichever expression provides the smallest value is labeled as the maximum gain. The AD623BR operates at the single supply voltage of +5-V. The common mode voltage is defined by the common mode voltage output of the CSA-1V, which is V_{CM} = 2.5 V. The maximum expected differential voltage is found by using the maximum current expected. The maximum input current expected for the power regulation board is set to 0.5 A, since the maximum rating for the fuse is this value. The differential voltage is V_{diff} = 87.5 mV. With these values known, the maximum gain of the amplifier can be found as

$$G_{\max} = \max\begin{Bmatrix} 41.1429 \\ 70.6286 \end{Bmatrix},$$

hence,

$$G_{\max} = 41.1429 \quad \text{V/V}.$$

The gain that can be set with standard resistor values is G = 40.00156 V/V, with the gain resistors 1.13 kΩ + 1.43 kΩ. These resistors are placed in series and put between the two gain programming pins of the AD623BR. The maximum output of the instrumentation amplifier is

$$V_{in-amp} = V_{diff} G_{\max} = (0.0875)(40.00156),$$

or

$$V_{in-amp} = 3.5 \quad \text{V max.}$$

The output of this instrumentation amplifier is further windowed by a non-inverting amplifier to obtain better resolution across a 0–5 V window. The windowing process has been explained previously, and the amplifier relationships are summarized in Table 4.14. With the added windowing stage, the bus current to voltage output is

$$I = \frac{V_{\text{out}}}{10}. \qquad \textbf{EQ4-22}$$

There is one more problem associated with the current sensor. In determining the current, there is some noise that appears at 100 kHz. To mitigate this effect, a simple RC low-pass filter is implemented at the output of the AD623BR. The in-line resistance should be the equivalent resistance seen at the inverting terminal of the windowing amplifier. A shunt capacitor of 0.1 μF was chosen to provide a cutoff frequency of 1.175 kHz.

Table 4.14 - Current Sensor Specifications

Specification	Value	Unit
Min. Current	0	A
Max Current	0.5	A
Slope: A	1/10	---
Intercept: B	0	---
In-amp Gain	40	V/V
In-amp Gain Resistor Value	1.13 k + 1.43 k	Ω
Windowing Amp Type	Non-inverting	---
R_1	14 k	Ω
R_2	3 k + 3 k	Ω
R_3	604 + 750	Ω

The temperature sensor monitors the temperature of the +5-V linear regulator. This is the component that dissipates the most power in the form of heat. The sensor is from Analog Devices and is the TMP36. The sensor is a three terminal device that has two pins for the power supply of +5-V and ground. The third pin is a voltage output that relates to the temperature. The TMP36 provides a linear output that relates directly to temperature. For each 10-mV change in the output voltage is a change in 1 °C. The reference point for the device is a 0.75-V output at a temperature of 25 °C. The maximum range of the device is –40 °C to +125 °C, which corresponds to a voltage output range of 0.1 V to 1.75 V. A gain of G = 5/2 is used in a non-inverting amplifier to spread the range of data output from 0.25 V to 4.375 V. Table 4.15 summarizes the temperature monitor specifications. With this amplifier, the temperature relationship becomes

$$T = 40V_{\text{out}} - 50 \ ^{\text{o}}\text{C}. \qquad \textbf{EQ4-23}$$

To mount the temperature sensor on the linear regulator, a metal tab is first attached to the temperature sensor with the Loctite thermally conductive adhesive 383. This adhesive is different than the thermal paste used for mounting the heat sink. The thermal paste does not have any adhering properties. The reason for this is the ability to remove the board from the box in case it has to be replaced. Once the temperature sensor has adhered to the aluminum tab, then the aluminum tab is adhered to the linear regulator with the 383. Lastly, the wiring to the sensor is done with Teflon coated wires and shrink tubing.

Table 4.15 - Specifications for Temperature Sensor

Specification	Value	Unit
Min. Temperature	–40	°C
Max. Temperature	125	°C
Slope: A	5/2	---
Intercept: B	0	---
Amp Type	Non-Inverting	---
R_1	2 k	Ω
R_2	3 k	Ω
R_3	1.2 k	Ω

4.7 Spacecraft Constraints

With the instrument explained in detail, there are several spacecraft design factors that need to be taken into consideration. First, the probe needs to be oriented perpendicular to the velocity vector. This ensures proper current collection for all bias regimes. For a satellite mission, if the probe axis is placed in the ram then only the electron density and temperature measurements can be determined. The thermal velocity for ions is much slower than that of the electrons, and there is incorrect data in the ion saturation region. The equation derived for the ion current collection was for a cylindrical probe that was perpendicular to the velocity vector. If the probe was placed in the wake, then no valid probe data can be determined, because the plasma is disturbed by the spacecraft.

When the probe collects current, there has to be a return current to the plasma. This is provided by the exposed conducting surface area of the spacecraft. If the current return area is not large enough, then the spacecraft tends to charge up. This excess charging may inhibit the used of the Langmuir probe. The minimum required exposed spacecraft surface area is 100 times the surface area of the probe; however, the recommended surface area should be at least 10,000 times greater than the area of the probe [*Jursa*, 1985]. For some satellite missions, the thermal design requires the use of coatings on the spacecraft surface. These coatings should be conductive. If the spacecraft is covered entirely by solar cells, and there is not enough exposed surface area due to this, then two solutions are possible. To mitigate this effect, glass planes are placed over the solar cells, and a transparent conductive coating is applied over the glass in order to increase the conducting surface area [*Brace*, 1998]. The other option is to only operate the probe in the ion saturation and electron retardation regions. With this option, the probe should not be operated in the electron saturation region. The total probe surface area including the guards was found to be 1.595 in.^{2} (10.2925 cm^2). With this probe surface area, the minimum required spacecraft exposed surface area is

$$A_{\min} = 160 \ \text{in.}^2$$

for one probe. If two probes are used, then the minimum surface area is twice this value.

Spacecraft charging could occur not only by the insufficient return area, but also by any exposed voltages, such as the solar cell interconnects. Solar cell interconnects have high voltages that, if left untreated, could charge up the spacecraft. *Brace* [1998] noted two possible solutions: tie the positive end of the solar panel to ground or coat the tabs in silicone. Connecting the positive terminal of the solar panel to ground allows only negative voltages at the interconnects. The spacecraft will not charge because the currents associated with positive ion collection are on the order of pico-amps to nano-amps, which is much smaller than the current

collected in the electron saturation region of tens of micro-amps. The second solution is a much simpler implementation. The solar cell interconnect tabs can be coated by a thin layer of silicone. The silicone used has to be able to handle the wide temperature ranges experienced in space. The Hotel Payload 2 and ESPRIT missions utilized a thin silicone coat to cover exposed terminals for strain gauges. This silicone was used in the nosecone of ESPRIT, which experienced high temperatures due to friction in the lower atmosphere. The silicone is the M-Coat C from Vishay Micro-Measurements. This silicone is capable of experiencing temperatures in the range of –60 °C to +260 °C for long term exposure. Short term exposure has a slightly greater range of –60 °C to +290 °C. The silicone is easy to apply; there are no requirements for baking, because the silicone cures at room temperature.

5 Flight Software

The flight software provides the instructions to perform all of the instrument processes. The Freescale Metroworks Codewarrior IDE aided in the development of the flight software. The software handles all the instrument processes mentioned in the previous two chapters. The program for the flight instrument utilized assembly machine code. The code was originally written in C; however, the compiler generated many machine instructions that were not necessary, which degraded the processing speed. The result of the degraded processing speed was that the sampling rate was cut down to about 100 samples per second for two probes in order for the interrupts and system processes to function properly. With the code written efficiently in assembly, the maximum sample rate achieved was 1040 samples per second for a two probe system or 2080 samples per second for a single probe system. The limiting factor becomes the communication protocol between the instrument and the flight computer. This is discussed in Section 5.4.3 below.

5.1 Software Structure

The high level software structure includes instrument initialization, electrometer calibration, housekeeping sent, and the main loop operation. Figure 5.1 displays the software algorithm. Each of the boxes has a subroutine associated with its function. In C programming, a subroutine is called a function. The initialization subroutine sets the starting value for each variable and also initializes each module: SCI, SPI, ATD, GPIO, and Timer. After the initialization subroutine, the electrometers are calibrated and the resulting data is sent.

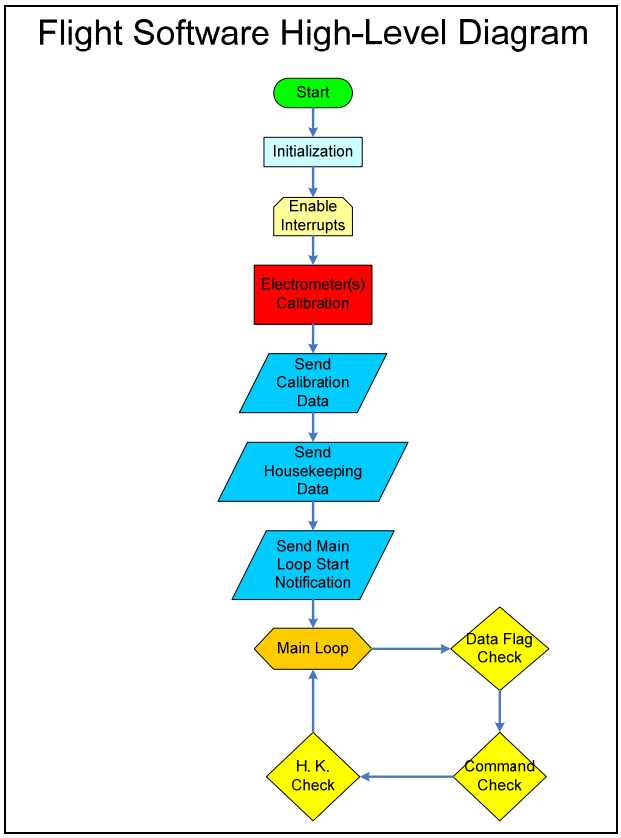

Figure 5.1 - High level flight software algorithm.

Housekeeping data is then taken and sent to the flight computer as well. Next, a notification is sent to the flight computer to signify that the instrument is entering into the main loop. This notification is also used to synchronize the data logging, because for high data sampling rates sync words cannot be sent after each transmission. In the main loop, there are three data flag checks. The change in the status of the data flags is driven by two interrupts: a timing interrupt and a data reception interrupt. The timing interrupt is dependent on the sampling rate and sweep rate. The data reception interrupt is activated by any reception of bytes by the SCI. These subroutines are explained in detail in the following sections.

5.2 Initialization

The first step in initialization is defining values for all the variables. Table 5.1 lists the variables that need to be defined by the user. With these variables defined, the software operates according to the user's desired mission requirements. There are also constraints on the values of the variables listed in the table. As stated previously, the maximum number of samples is 2080 samples per second. This requirement is derived from the sample rate and the baud rate of the communications to the flight computer. One sample consists of three bytes (the significance of these bytes is explained later in Section 5.4). If the sample rate increases, then the time duration required to send data increases. The maximum baud rate for asynchronous communication with this microcontroller through RS-232 or RS-422 is 115200 bps. Next, the sampling rate constraint is derived. For a sample rate of 1040 samples per second in two probe operation in adaptive sweep mode, the time allowed for 1 sample is 0.9615 ms, and the instrument has to send 6 bytes in this time period (3 bytes for each probe sample). The time required to send this data is 0.5208 ms, and this time duration is already more than half the time period allotted between samples. There is 0.4407 ms left to collect the data through the ATD module, send probe bias data through SPI, and any data processing. Derived from the ATD sampling constraints and initialization parameter, the sampling of the ATD takes 0.2458 ms; the time for SPI communications is negligible, comparatively, at 5.92 μs. With all these times defined, the total time required for the SCI, ATD, and SPI is 0.77252 ms, which leaves 0.18898 ms for data processing. This is how the sampling rate constraint is found.

Table 5.1- Initialization Variables Required to be Set by User

Variable	Relationship	Typical Value	Minimum Value	Maximum Value
BAUD	SCI Baud Rate	0x07 (115200)	0x07 (115200)	0x1BBE (110)
SYNC1	Sync Byte 1	0x4C ('L')	0x00	0xFF
SYNC2	Sync Byte 2	0x50 ('P')	0x00	0xFF
SAMP	Sampling Rate	0x0410 (1040)	0x0271 (625)	0x0410 (1040)
TIME_INT	Timer Interval	Clock/SAMP	0x2EF3	---
P1_BIAS_START	Start Value	0x031E (–5)	0x0000 (–8.192)	0x0FFF (+8.188)
P1_BIAS_END	End Value	0x0CE2 (+5)	0x0000 (–8.192)	0x0FFF (+8.188)
P2_BIAS_START	Start Value	0x031E (–5)	0x0000 (–8.192)	0x0FFF (+8.188)
P2_BIAS_END	End Value	0x0CE2 (+5)	0x0000 (–8.192)	0x0FFF (+8.188)

Continuing with the initialization subroutine, the various modules of the microcontroller are setup. The first module to be initialized is the SCI module. For the SCI module there are three registers that require values to be written to them. Two of the registers are control registers

for the module. This module controls the RXD and TXD pins (pins 38 and 39). The first control register, SCICR1, controls the data format of the transmitted byte. The data format is set at 8 bits of data with 1 start bit, 1 stop bit, and no parity bit (8-N-1). The second control register dedicates the RXD and TXD pins to the SCI module as well as interrupt control. The receive interrupt is set, and the transmit interrupt is cleared. The transmit interrupt is set only when data needs to be transferred. The interrupt subroutine handles these requests. The last register to be set is the baud rate. The baud rate is set by two registers: SCIBDH and SCIBDL. To set the desired baud rate, the data to be entered into the registers is

$$D = \frac{\text{Bus Clock}}{16(\text{Baud Rate})}.$$

The number found needs to be a whole number, and the result should be rounded. The user needs to be cautious of not selecting a baud rate that is greater than 3.75% error, where the percent error is found by

$$\%\ \text{error} = \frac{|\text{Theoretical} - \text{Calculated}|}{\text{Theoretical}} \times 100\%.$$

Table 5.2 lists the values set for the three SCI registers in hexadecimal.

Table 5.2 - SCI Module Registers

Register	Value
SCIBDL	BAUD
SCICR1	0x00
SCICR2	0x2C

The next module to be initialized is the SPI module, which communicates to the DACs to provide the probe bias. This module also has three registers to initialize. The first control register, SPICR1, enables the SPI module and defines the data format in transmission. The specific data format requirements are derived from the specifications of the DAC, the AD5530. The DAC requires two bytes to transfer and an idle low polarity and even phase. The second control register, SPICR2, defines the function of the SS' pin and the MISO pin. These two pins correspond to the PM3 and PM2 GPIO pins, respectively. Since there are two DACs, a single sync line by use of the SS′ pin cannot be used. The PM3 and PM2 pins act as GPIO for the sync lines to the two DACs. These pins have to be configured such that there is no master input, and this is done with SPICR2. The last register to be set is for the baud rate, SPIBR. To minimize time, the maximum baud rate allowable is used. The baud rate for the SPI module is found by

$$\text{Baud Rate} = \frac{\text{Bus Clock}}{(\text{SPPR}+1)2^{(\text{SPR}+1)}},$$

where SPPR and SPR are three bits each in the baud rate register. The maximum baud rate is found by having SPPR and SPR as zero. This produces a clock rate of 6.25 MHz. The maximum clock rate for the DAC is 7 MHz; therefore, this baud rate meets all requirements. Table 5.3 lists the values of the three SPI registers.

Table 5.3 - SPI Module Registers

Register	Value
SPICR1	0x54
SPICR2	0x09
SPIBR	0x00

The ATD module is the next module to be initialized. The ATD module requires three registers to be written to as well. The first register to be set is the second control register, ATDCTL2, which powers up the ATD module. The next register to initialize is the third control register, ATDCTL3, and this register sets up the number of sample conversions per sequence. As stated previously, the ATD module creates 4 separate conversions in one sequence that are averaged together in order to obtain 1 sample. The last register is control register 4, ATDCTL4, which sets up the resolution, conversion time, and ATD clock. The ATD clock rate is calculated by

$$\text{ATD Clock} = \frac{\text{Bus Clock}}{2(\text{PRS}+1)},$$

where PRS is a 5-bit pre-scaler to the bus clock. A requirement for the ATD clock is that the ATD clock cannot be greater than 2 MHz. The resolution is set to the greatest resolution available, 10-bit; the conversion time is made to be 4 ATD clock cycles, and the ATD clock is set to the maximum possible bus clock, which is 1.5625 MHz. Table 5.4 lists the necessary values for these three registers in order to meet the specifications above.

Table 5.4 - ATD Module Registers

Register	Value
ATDCTL2	0x80
ATDCTL3	0x20
ATDCTL4	0x23

The GPIO is initialized next, for which 13 pins are set to output and 1 pin for input. The GPIO are set for either input or output by writing to the data direction registers. A 1 signifies an output and a 0 signifies an input. There is one data direction register for each port, and there are 6 ports that require initialization. The GPIO that are initialized are listed in Table 4.9. Table 5.5 lists the data direction registers that need to be set. After initialization, all output ports are set to logic 0 except for the SPI sync pins. These two pins, PM3 and PM2, are set high, because these pins function as an active low for SPI communication.

Table 5.5 - GPIO Registers

Port	Data Direction Register	Value
T	0xFF	0x00
B	B4 = 1	0
E	B1 = 0	---
A	B0 = 1	0
M	B0:3 = 1	PTM0:1 = 0 and PTM2:3 = 1
P	B5 = 1	0

The last module that needs to be initialized is the timer module. The timer channel 0 is used for generating timing interrupts. These interrupts regulate the data sampling and probe bias. The timer channels are under the output compare function. The output compare functions can be used to generate square and astable waveforms or for software delays. In the case of the instrument, the timer channel 0 is used for a software delay. There are five registers that need to be set and two flags that need to be cleared. The first register to be written to is the first control register, TSCR1, which enables the timer module. Next, the output compare channel 0 is activated by writing to the TIOS register. The next register is the interrupt enable register, TIE. After setting up this register, the second control register, TSCR2, is written to set the clock to increment the timer register, TCNT. To obtain the greatest resolution in time, the smallest clock period is used, and this means that the clock used is the bus clock. There is no equation to set the clock period as in the other modules of the microcontroller. The table with the predefined clock periods are in the microcontroller datasheet [*Freescale Semiconductor*, 2007]. The final register to set is the timer input/output compare register 0, TC0. This register defines the specific time duration until the interrupt occurs. The interrupt occurs when the timer register, TCNT, is equal to the timer input/output compare register 0, TC0. In the initialization subroutine, the TC0 register is set to be the interval time defined by the sampling rate and sweep rate. Table 5.6 lists the necessary registers that need to be written with their values. Figure 5.2 displays the processes involved in the initialization subroutine.

Table 5.6 - Timer Module Registers

Register	Value
TIOS	0x01
TSCR1	0x80
TIE	0x01
TSCR2	0x00
TC0	TIME_INT

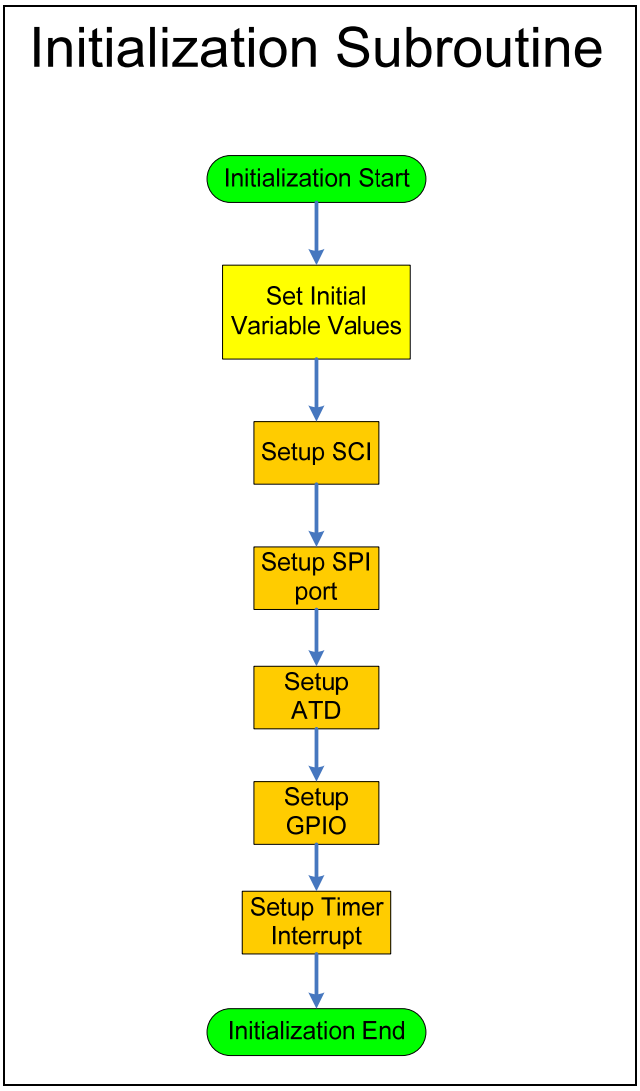

Figure 5.2 - Initialization subroutine flowchart.

5.3 Interrupt Service Routines

There are two interrupts in the program that control the processes of the instrument. The two interrupts are the timer interrupt and the SCI interrupt. First, the interrupt vector has to be assigned to the specific interrupt subroutine. This allows the microcontroller to associate the interrupt subroutine with the proper interrupt request. These interrupt requests are in a vector table that lists the interrupts according to priority. The addresses of the interrupt vectors are in Table 5.7. Higher interrupt vector address number have higher priority; therefore, the timer interrupt has higher priority than the SCI interrupt.

Table 5.7 - Interrupt Vectors

ISR Name	Vector
Entry	0xFFFE
OC0ISR	0xFFEE
SCIISR	0xFFD6

The timer interrupt service routine only contains simple processes, such as arithmetic or compare instructions. Interrupt service routine processes should have as little as possible processing instructions to prevent any latency. The timer interrupt service routine sets a flag called DATAFLAG, which monitors if a timing interrupt has begun. In the main loop, there is a compare statement to monitor DATAFLAG. Each time DATAFLAG is set, a jump to the data collection subroutine is made; otherwise, the microcontroller skips this and continues in the main loop. After setting this flag, the output compare interrupt flag, TFLG1, is cleared by writing a 1 to the appropriate bit. For channel 0, this bit is B0. After flag is set, then the TC0 register should be reset to the appropriate time interval. Figure 5.3 displays a flowchart for the timer interrupt service routine.

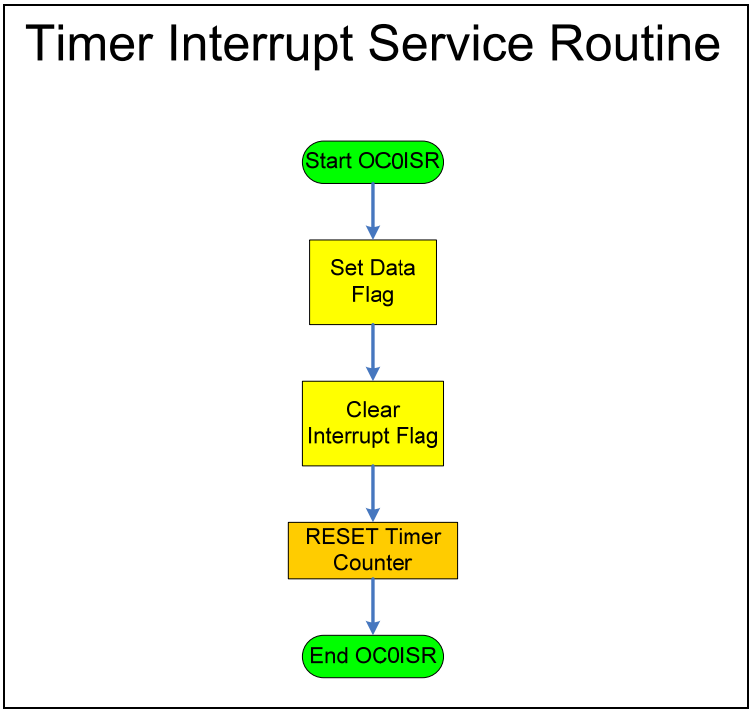

Figure 5.3 - Timer interrupt service routine.

The second interrupt service routine (ISR) is for the SCI module. The ISR handles two types of SCI interrupts: receive and transmit. In the initialization subroutine, the SCI module is set for receive interrupts. The ISR reads the SCI status register, SCISR1, to determine if there is a transmit interrupt or a receive interrupt. The transmit interrupts only when data needs to be sent by the program. For receive interrupts, the interrupt vector is cleared only when the input buffer is empty; therefore, until the input buffer is empty, the ISR is called continuously. To provide synchronization, the ISR checks for the two sync bytes 'L' and 'P'. Once these bytes are found, then the command byte is next (see Section 5.5). If the two sync bytes 'L' and 'P' are not sent in this exact order, then the ISR ignores these bytes until a successful read of the two sync bytes. After the command byte is found, the program continues in the main loop to handle this new command. Next, for data transmit, the TX interrupt bit needs to be set in the second SCI control register, SCICR2. This bit is bit 7, B7. Once this bit is set in software, then the SCI module transmits the bytes in the output buffer until all bytes are transferred. When all the bytes

in the output buffer have been sent, then the TX interrupt bit, SCICR2:B7, is cleared. Figure 5.4 illustrates the flowchart for the SCI interrupt service routine.

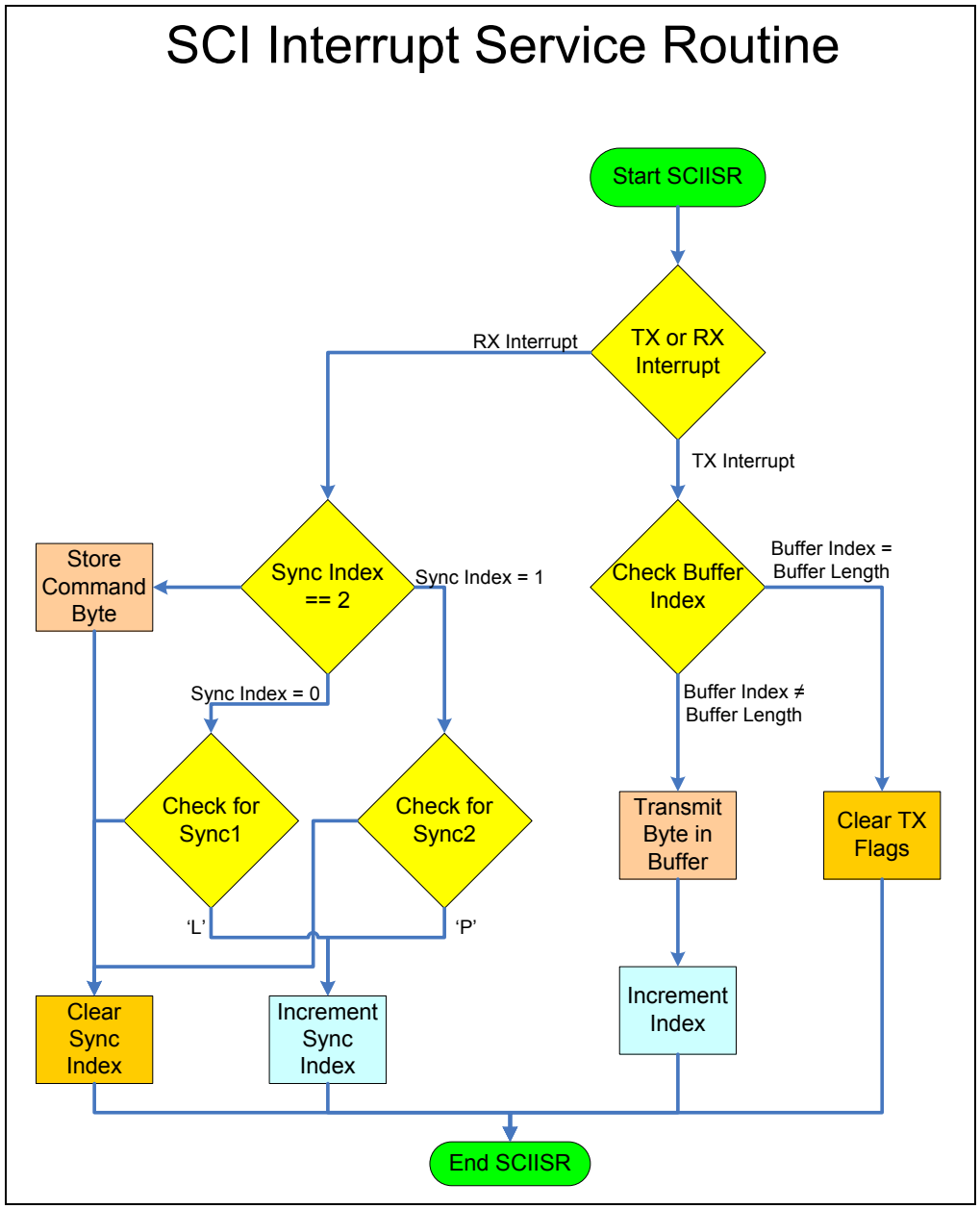

Figure 5.4 - Asynchronous communications interrupt service routine.

5.4 Data Collection Subroutine

The data collection subroutine is the primary code that samples the ATD ports, sets the desired probe bias, and sends the data out via the SCI. Figure 5.5 displays the high level algorithm for the data collection subroutine. The data collection subroutine runs when bit 0 of DATAFLAG is set by the timer interrupt. After the flag is set, the data collection subroutine starts by checking DATAFLAG bit 1. This bit signifies if the microcontroller is running the subroutine for the first time. If this subroutine is executed for the first time, then the microcontroller skips the data sampling and goes to the probe bias first. The probe bias is set by

using the SPI module communication to the DAC. Next, DATAFLAG is checked again, and if it is the first sweep, then the data output by the SCI module is skipped. Before the subroutine ends, the DATAFLAG:B0 is cleared, and the microcontroller returns to the main loop.

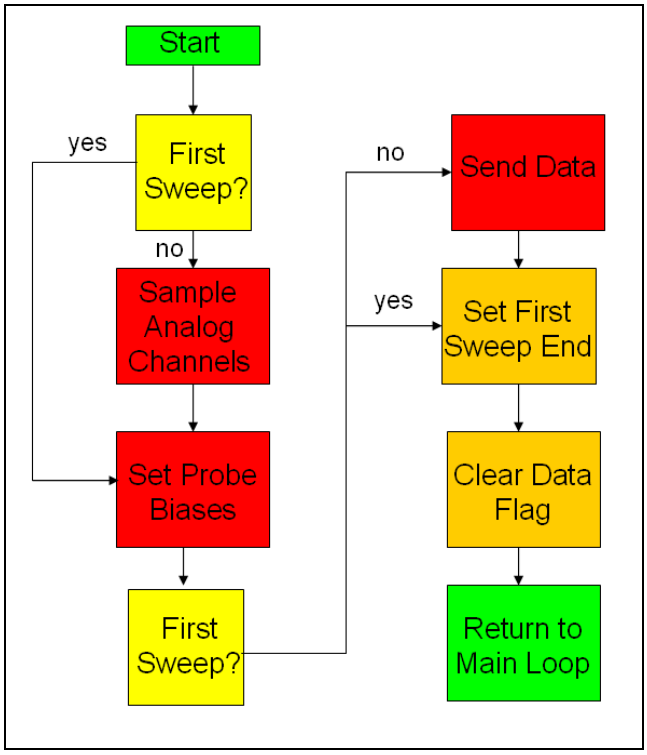

Figure 5.5 - High level algorithm for the data collection subroutine.

5.4.1 ATD Sampling

The data sampling subroutine executes after a change in the probe bias at the following timer interrupt. This allows for the maximum time between timer interrupts to allow any data output change from the signal conditioning circuit to settle. Figure 5.5 illustrates the order of when data sampling commences among the probe bias subroutine and data output subroutine. For each sample, four conversions are created and stored in the ATD data registers. These four conversions are then averaged together to provide one sample; therefore, one sample is an average of four measurements. The probe bias reference and the full windowing output are first sampled for each probe. Next, a windowing subroutine checks to see which window output to sample from the full windowing data. Table 5.8 lists the divisions for the full windowing data corresponding to the appropriate windowing stage to sample. In the windowing subroutine, there are two bytes generated that provide information for the type of windowing output sampled and the data associated to that windowing output. The byte associated to the type of windowing output is an indexing reference. Table 5.8 lists the index number and the related windowing output sampled. If the full window data is outside the range of the four windowing stages, then the full data is used.

Table 5.8 - Windowing Divisions

Windowing Stage	Index	Full Window Range
Ion Saturation	1	108–512
Electron Retardation	2	513–757
Electron Ret./Sat.	3	758–906
Electron Saturation	4	907–1023
Full Range	5	0–107

This is only the case for the ion saturation range, but it would take a density greater than the ionospheric plasma to be in this range. After these two bytes are set, there is a subroutine to check for the floating potential. An easy method to check for the floating potential is to monitor the indexing for the windowing stages. Once the index number goes from a 1 to a 2, the current probe bias marks the floating potential. This means that the data output moves from the ion saturation window to the electron retardation window. This floating potential value is used in the adaptive sweep mode to bias the probe ±5 V around this value. In the acquisition sweep, the first floating potential value is set to be 0 V. After this sweep, the floating potential is adjusted accordingly. The complete sampling subroutine is in Figure 5.6a, and Figure 5.6b illustrates the floating potential subroutine.

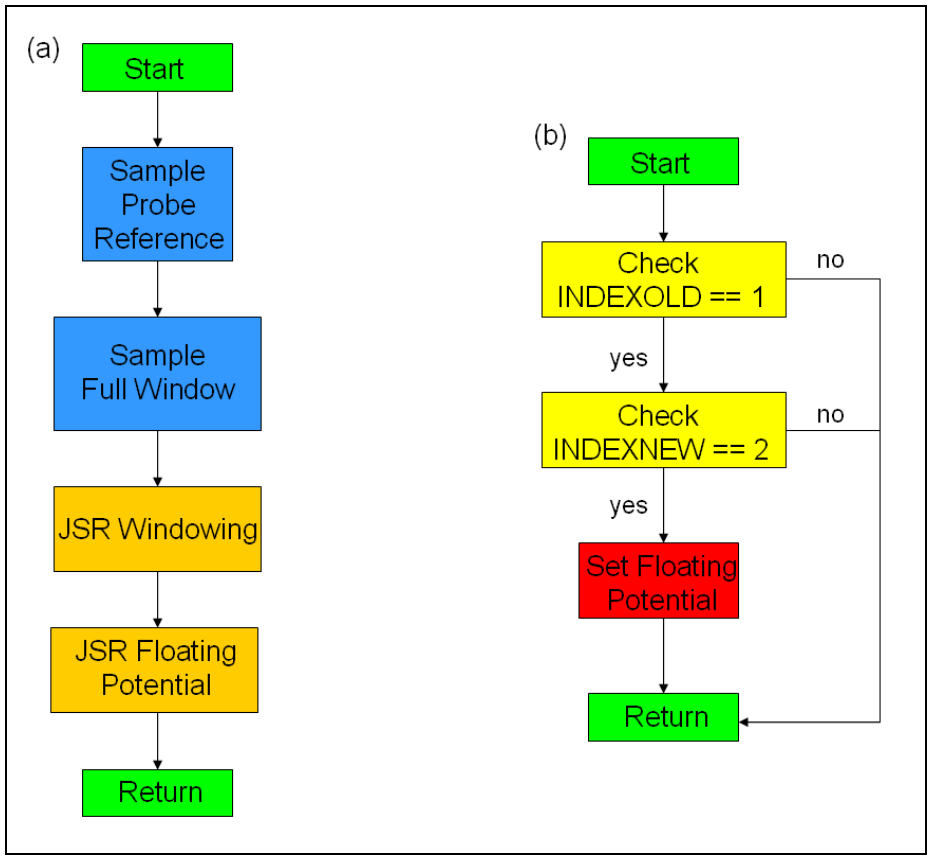

Figure 5.6 - a) Sampling algorithm. b) Finding the floating potential.

5.4.2 Probe Bias

The probe bias depends on the mode of operation. In a typical two probe operation, one probe is usually swept biased and the second probe is fixed biased; however, if the mission requires both probes to be swept or if probe 2 needs to be swept, then this can be done as well. The swept biased probe can follow any of the three mission operation modes discussed in Chapter 3. The fixed biased probe can be biased to be in the electron saturation region or the ion saturation region depending on the mission requirements. For any swept bias mode, there are three parts to generate the sawtooth waveform. During initialization, there are four count words and a step size byte that correspond to the generation of the sawtooth waveform. Three of the count variables list the number of counts per the three regions of the sawtooth waveform. The three regions of the sawtooth waveform are the two constant bias sections at the extrema and the linear region. The number of counts corresponds to the number of samples. The step size variable is for the linear region of the sawtooth waveform. The step size is added to the previous swept bias value after each timer interrupt to generate a linear region with respect to time. Table 5.9 lists the count variable values and step size value for a sawtooth waveform at a 1-Hz sweep rate. The count variables are solved in the program given the sample rate and sweep rate. For the fixed biased probe, the probe bias is also set at each timer interrupt, even though the probe bias is constant. The reason for this is to prevent any drift that may occur.

Table 5.9 - Count Variables for a 1-Hz Sawtooth Waveform

Count Variables	Value
COUNT1	140
COUNT2	972
COUNT3	1040

With the probe bias logistics stated, the implementation of the probe bias software can now be discussed. As mentioned previously, the probe bias is set by use of the SPI module. The data that needs to be transferred to the DAC is 1 word or 2 bytes. The DAC requires the 12-bit data to be at the center of the word, meaning that there are two “don’t care” bits on either end of the sent data. Figure 5.7 illustrates the required data format. Since the data needs to be shifted by two bits to the left, this corresponds to multiplying by 4; however, in assembly language there is an instruction to shift the bits in a word (called LSLD or LSRD), which only takes one clock cycle each to execute.

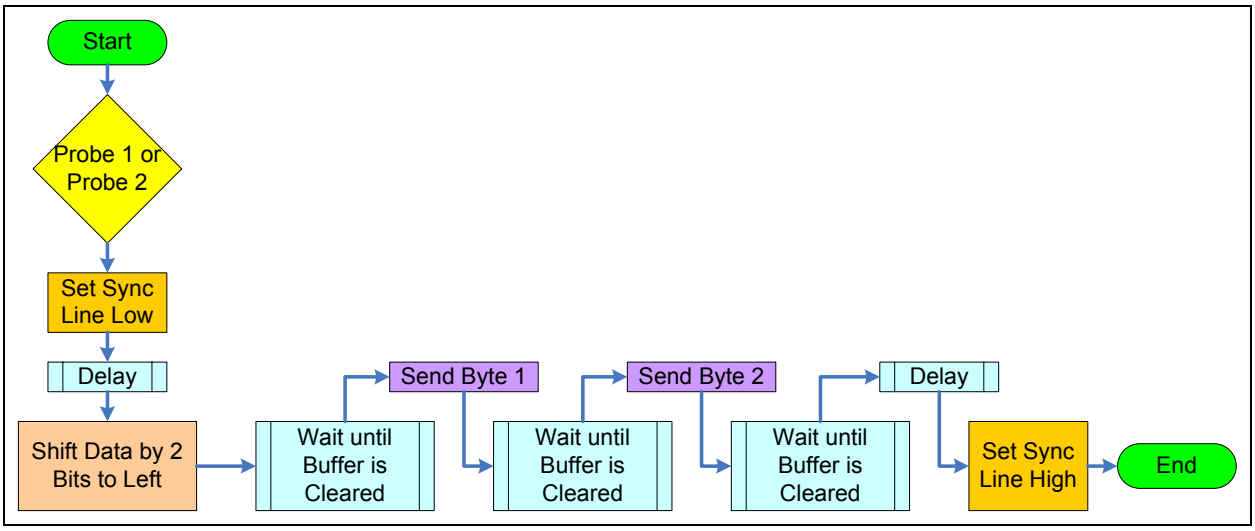

Figure 5.7 - Probe bias routine.

Multiplying and exchanging data registers takes three clock cycles for multiplying and one clock cycle to exchange data registers (exchanging data registers is required, because when two 16-bit numbers are multiplied, the result goes into index register Y, where as data to be sent out needs to be in accumulator D). This gives a total of four clock cycles necessary for the multiplication method, instead of two for the logical shifts. Next, in the toggle of the sync lines, a delay is necessary between the sync line change and the data transmission. Figure 5.7 displays this required delay. The required delay is at least 0.75 µs, and this accomplished by 10 NOP statements, which gives a total time delay of 0.8 µs. This delay is needed before data transmission and after data transmission. Prior to any transmission of data to the DACs, the SPI status register needs to be checked for any current data transmission in progress. If the SPI module is transmitting, then the microcontroller waits until the transmission is complete. With these factors taken into account, the microcontroller is able to communicate to the DAC to set the probe bias.

5.4.3 Data Transmission

After the new probe bias is set, the data collected from sampling are sent. The data transmission does not occur for the first data step after instrument turns ON, since there are no data to transmit. Before sending the raw data, the data have to be compressed in order to save time. The data to be transmitted are: the probe bias reference, the windowing index, and the windowing output data. The probe bias reference and windowing output data are initially stored as two bytes each and the windowing index as one byte. The ATD module only provides 10-bit conversion, and the window index only goes to 5; therefore, there are some unused bits, and the 5 bytes can be compressed to 3 bytes. The 5 bytes are compressed to the 3 bytes according to Figure 5.8. BYTE 1 contains the MSBs of the probe bias reference, and BYTE 3 contains the LSBs of the windowing data. BYTE 2 includes the two LSBs of the probe bias reference, the three bits of the windowing index, and the two MSBs of the windowing data. This cuts the data transmission time down in order for there to be enough time to perform the other microcontroller processes. For two probe operation, this creates 6 bytes to transfer per sample of each probe.

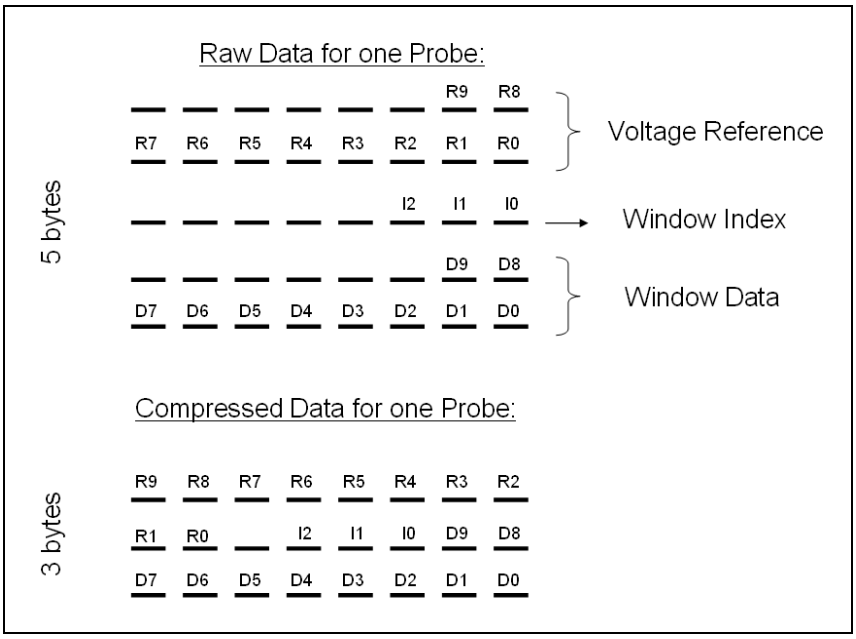

Figure 5.8 - Data compression scheme.

5.5 Other Operational Modes

The operational modes, other than the data collection mode, are the probe clean mode, electrometer calibration mode, and housekeeping mode. Each of these modes are activated by external communication via the SCI receive interrupt. Once a valid command has been received, then the microcontroller clears the timer interrupt. Next, the appropriate subroutine corresponding to the command executes. The probe clean mode is the only subroutine with a loop. To exit the probe clean mode, a command can be sent to the instrument to end the mode and re-initialize the program, or the power can be cycled to the instrument in order to reset. The other two modes execute only once, and then return to the data collection mode.

5.5.1 Probe Clean

In the probe clean mode, the probe is biased with a high voltage. There is a relay that connects the +12-V supply to the input of the EMCO DC/DC converter. This relay is switched on by the microcontroller via pin PP5. The relay is active high; therefore, during initialization, the pin is set low. To change mode into the probe clean mode, the correct command byte has to be sent to the instrument. First, the correct sync bytes have to be sent ('L' and 'P'), and then the command byte is sent. The command byte for the probe clean mode is 'A' or 0x41 in hexadecimal. When this command byte has been received, first the time interrupt is disabled, and then the high voltage DC/DC converter is turned on. During this probe clean period, another time interrupt is generated, but this time the time interval is once every minute. The time interrupt is for sending housekeeping data throughout the duration of the probe clean phase. To exit the probe clean mode, the power to the instrument can be cycled, or another command can be sent. If the command 'D' (0x44) is sent, then the program returns to the data collection mode. If a command for electrometer calibration or housekeeping is sent, then the microcontroller executes this command and returns to data collection mode.

5.5.2 Electrometer Calibration

The electrometer calibration mode measures the output of the electrometer for various input currents. The command to execute the electrometer calibration mode is 'B' (0x42), and similar to the probe clean command, the two sync bytes ('L' and 'P') need to be sent prior to the command byte. The currents are created by biasing the electrometer with a voltage and connecting the input of the electrometer to the high resistance. This creates a current corresponding to the resistance value. There are four resistors that provide four reference currents for calibration. Table 4.9 lists the general purpose outputs of the microcontroller used to switch the relays. When switching the relays, at least a 2-ms delay is necessary before measurements are made due to the contact bounce during switching. After all the measurements have been made, the data are sent out in an uncompressed format. This format differs from the compressed data format in the data collection mode. The data format is the same as the raw data format prior to compression in the data collection mode. The top section (raw data section) of Figure 5.8 displays the format for each data sample taken for the housekeeping in the order of the data that is sent out.

5.5.3 Housekeeping

The housekeeping subroutine sends out the data output from the housekeeping circuits. Table 4.13 to Table 4.15 list the different types of housekeeping for the power regulation board, and Table 4.9 lists the specific pins used to control the analog multiplexer for switching the inputs to the ATD module. If the power regulation board is not used, then there is no housekeeping for any of the power buses. The command for sending housekeeping data is 'C' (0x43). Again, the two sync bytes have to be sent prior to the command byte. Only one sample of each housekeeping monitor is sent. Housekeeping data are sent continuously in the probe clean mode once every minute. The data format for the samples is the same raw data format of the electrometer calibration. The order of bytes sent corresponds to the order of the housekeeping monitors.

6 Instrument Testing

There are three different levels of testing the instrument. The first level is at the board level, where there are functionality tests for all components of each board. For the second level, the boards are tested in a relevant environment. The final level of testing is a full instrument test with a plasma source. Only functionality tests have been completed with the instrument thus far.

6.1 Functionality Tests

Each board is tested for all necessary inputs or outputs. There are four boards to test that have been discussed in detail in the instrument design chapter (Chapter 4).

6.1.1 Electrometer Testing

The electrometer design was tested during ESPRIT. The same design is used for the new instrument. Figure 6.1 displays an example of calibration data for the electrometer. This figure displays data for when current flows from the electrometer, i.e., when a +5-V bias is given to the electrometer with a high resistance resistor placed at the input. The electrometer is also calibrated with a –5 V bias input, which causes the current to flow in the opposite direction, i.e., into the electrometer. With these two biases, the electrometer is calibrated for all regions of the *I–V* curve. Ideally, the calibration data contain an inverse relationship on either side of the electrometer output; however, the feedback diodes of the D-PAD1 do not have exactly the same dimensions and characteristics. The different characteristics cause different voltage drops across the diode even with the same magnitude of current. For this reason, the electrometer is calibrated for both current collection cases.

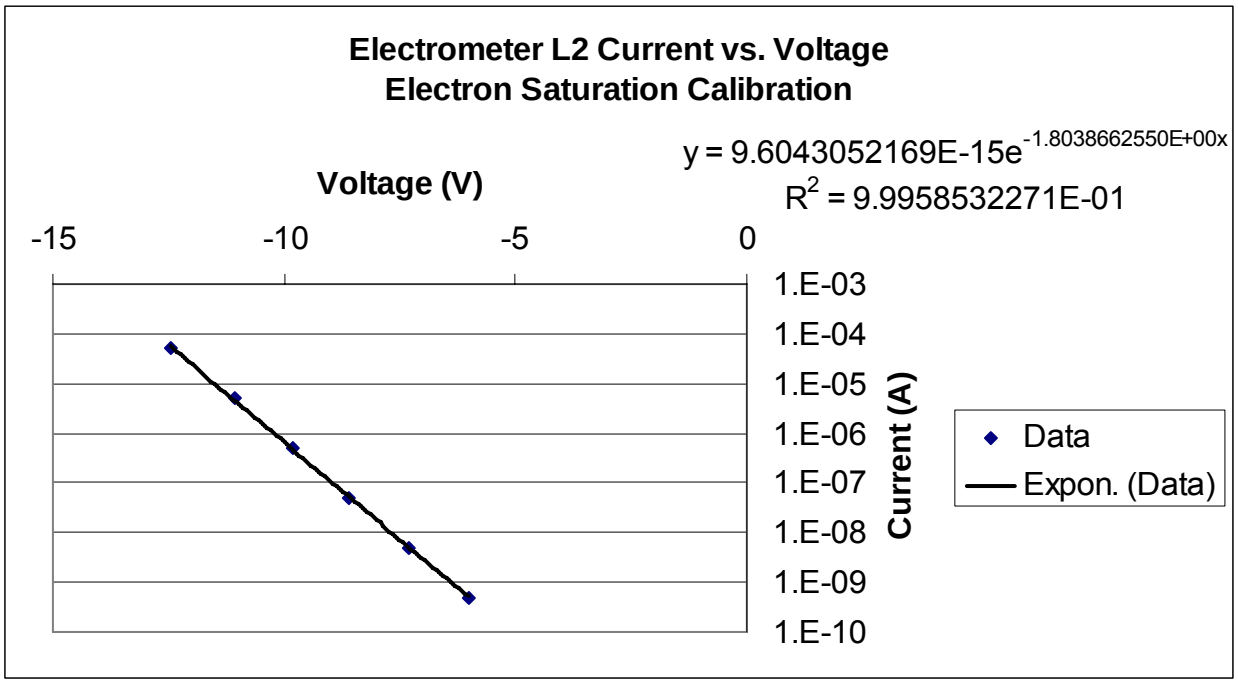

Figure 6.1 - Calibration data from one of the ESPRIT electrometers.

When calibrating the electrometer, the circuit board needs to be enclosed in a conductive box to prevent any EMI from disturbing the measurements. The bolt-in RFI filters, as mentioned

in Chapter 4, assist in shielding the electrometer from undesired effects. When calibrating, the box of the electrometer needs to be grounded, because as was discovered once during testing, when the box of the electrometer is not grounded, the lowest measurable current is in the micro-amps. With the box properly shielded, measurements are capable well below this. Professor Croskey developed a calibration method that includes a decade box and a larger box within which to place the entire device under test. Figure 6.2 displays this box.

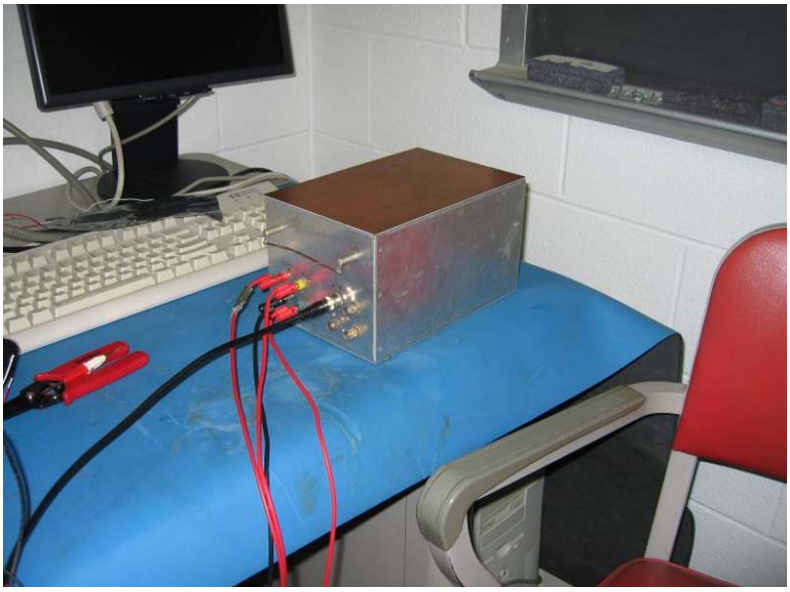

Figure 6.2 - Enclosure used to calibrate the electrometers.

6.1.2 Calibration Board

To fully test the calibration board, the electrometer is calibrated with the calibration board, and the results are compared to the calibration with the decade box. In order to test the calibration board, both the electrometer and the calibration board have to be placed within an enclosure, and bolt-in RFI filters are used for the calibration I/O as well.

6.1.3 Control and Processing Board

There are four separate tests to verify the functionality of the control and processing board. Each section under test was tested separately with one section populated at a time. The first section tested was the signal conditioning circuitry. The input of each set of signal conditioning circuitry varies, while the outputs are checked. Four different voltages are selected for the voltage input, such that each voltage provides an output within the range of the windowing stages. Table 6.1 lists an example for the input voltages used with their corresponding output voltage for each windowing stage.

Table 6.1 - Example of Signal Conditioning Output

Input Voltages [V] (Electrometer Output)	5	–2.5	–7	–11
Full Output [V]	1.458	3.021	3.958	4.792
Ion Saturation Output [V]	2.368	5	5	5
Electron Retardation Window [V]	0	2.083	5	5
Electron Ret./Sat. Window [V]	0	0	1.875	5
Electron Saturation Window [V]	0	0	0	3.333

The next section populated and tested was the microcontroller and supporting circuitry. The supporting circuitry include the oscillator section, bypass capacitors, programming pull-up resistors, and programming header. Next, the microcontroller was programmed with the flight software. The first part of the test was to see if this is possible. The next test was to measure the bus clock of the microcontroller, which is half of the oscillator frequency. This was done by monitoring the PE4 pin on the microcontroller with an oscilloscope. This pin outputs the bus clock frequency by default.

The probe bias circuitry was populated next. Depending on the program loaded onto the microcontroller, the expected result should appear at the electrometer bias input terminals. For the program in Appendix A, probe 1 is biased by a sawtooth waveform in the adaptive sweep mode, and probe 2 is biased with a DC voltage. Figure 6.3 displays the sawtooth waveform on an oscilloscope. The bias voltages also appear at the analog inputs to the microcontroller as the voltage bias inputs. These measurements are scaled down to fit within a 0–5 V range.

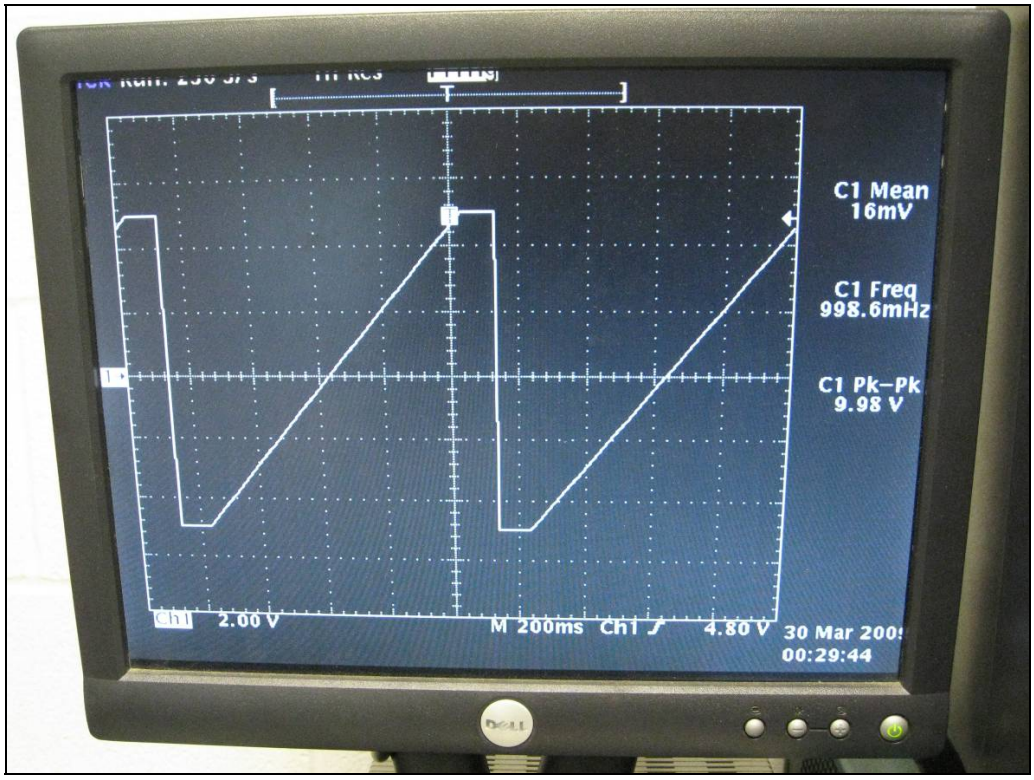

Figure 6.3 - Output from the oscilloscope displaying the sawtooth waveform.

The final section tested on the board was the asynchronous communications section. The relay and appropriate line drivers were populated. There were two parts to testing this section. There is one test for the flight computer communications and another test for the external ground support equipment communications. To test the communications, the external testing computer monitors the data output from the instrument.

6.1.4 Power Regulation Board

Similar to the testing of the control and processing board, the power regulation board contains five different tests. The first step in populating the board is to place the four land grid array active filters on the board by using solder paste and the reflow oven. The first test is to

calibrate the current sensor. The current sensor requires calibration, because the measurement error of the CSA-1V and the gain of the instrumentation amp and windowing stage is large, which may give a slight error. Currents are simulated by varying the power supply current limit across the input and output traces, while monitoring the current monitor output. Figure 6.4 displays an example of the current sensor calibration. The other housekeeping monitors were tested in a similar manner.

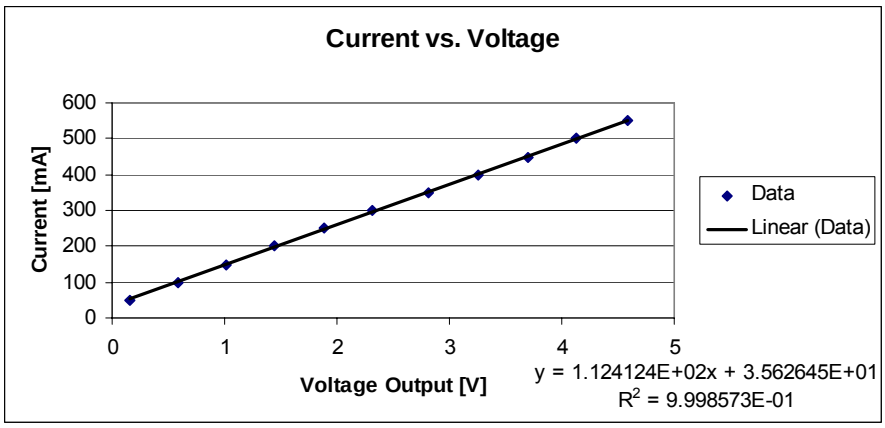

Figure 6.4 - Calibration of the current sensor.

Next, the +12-V, +5-V, and –12-V regulation parts are populated and tested. The switching frequency has been monitored for four cases: DC/DC converter alone, only with passive filters, with passive and active filters without the –12-V connected, and with passive and active filters with the –12-V connected. Figure 6.5 to Figure 6.12 display each of these cases. There are two cases with the –12-V connected or not connected due to noise introduced from the –12-V supply. The DC/DC converters have to be shielded as well, because the radiated EMI added about 10 dBm to the bus supplies. To calculate the RMS voltage, the power needs to be converted to watts, then divided by the load resistance of the spectrum analyzer (R = 50 Ω). The square root of this value is next found. This is the RMS voltage is found by

$$V_{\text{RMS}} = \sqrt{\frac{P[\text{W}]}{R}}.$$

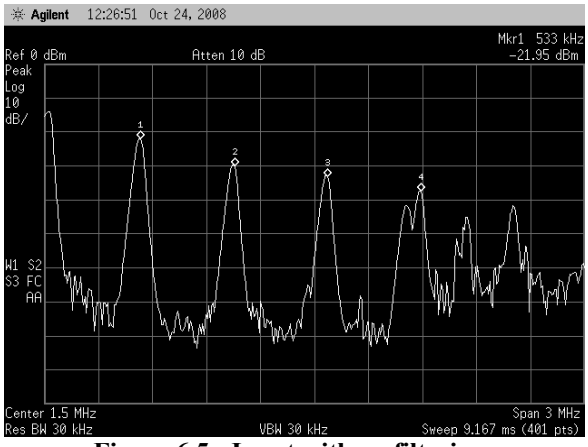

Figure 6.5 - Input with no filtering.

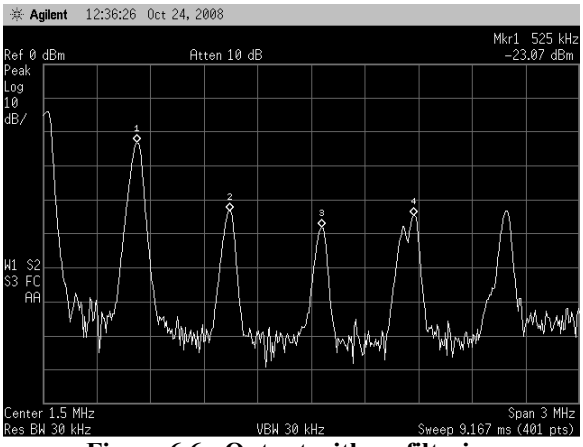

Figure 6.6 - Output with no filtering

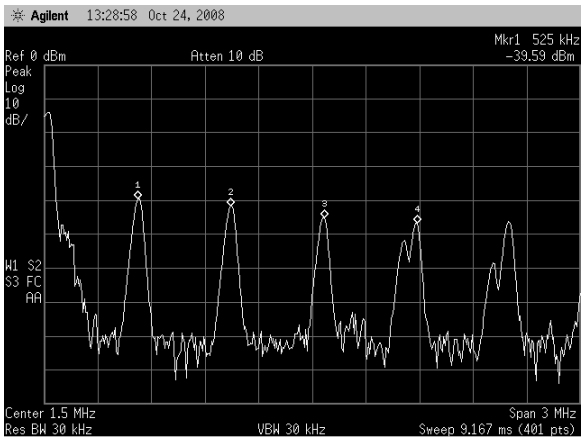

Figure 6.7 - Input with passive filtering.

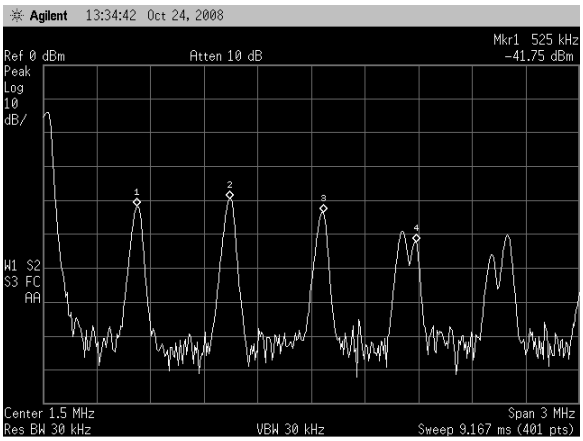

Figure 6.8 - Output with passive filtering.

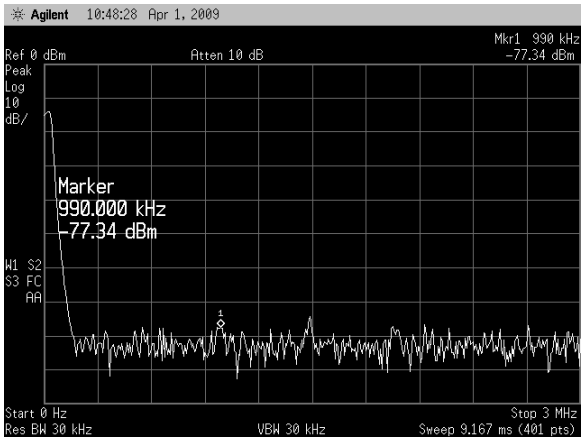

Figure 6.9 - Input with active filtering no –12-V.

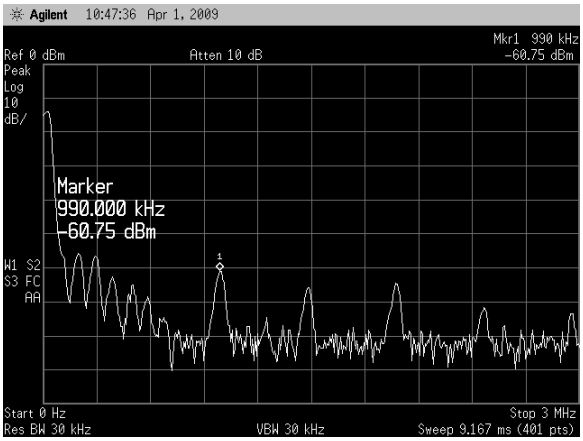

Figure 6.10 - Output with active filtering no –12-V.

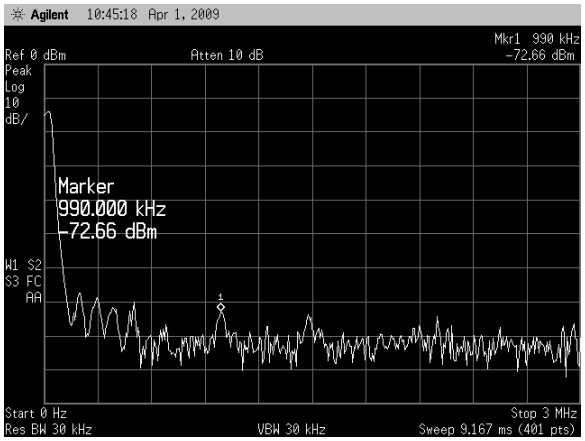

Figure 6.11 - Input filtering with –12-V.

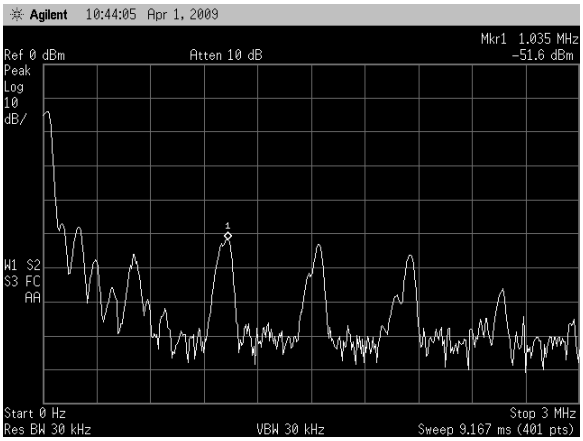

Figure 6.12 - Output filter with –12-V.

The resulting RMS voltages and associated powers are provided in Table 6.2 for each case. The input noise power decreased significantly from the original value of –21.95 dBm to –72.66 dBm. The associated RMS voltage is slightly greater than 52.1 μV. Therefore, very little power is conducted into the unregulated supply bus. Another interesting feature of the input

filters is the power supply rejection. There was some ripple due to the external DC power supply (see Figure 6.13) that gets filtered out due to the input filters. The power associated to the ripple of the power supply was originally –38 dBm, and this was reduced to the noise floor of –70 dBm to –80 dBm.

Table 6.2 - Power Line Ripple

Case	Maximum Peak [dBm]	RMS Voltage [mV]	Frequency [kHz]
Input – No Filter	–21.95	17.9	533
Output – No Filter	–23.07	15.7	525
Input – Passive Filter	–39.59	2.34	525
Output – Passive Filter	–39.54	2.36	990
Input – Active Filter & No –12-V	–77.34	0.0304	990
Output – Active Filter & No –12-V	–60.75	0.205	990
Input – Active Filter with –12-V	–72.66	0.0521	990
Output – Active Filter with –12-V	–51.60	0.588	1035

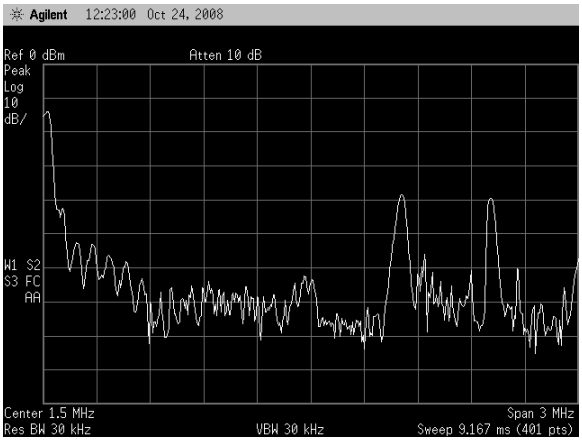

Figure 6.13 - Power supply noise.

For the output filters, the noise is significantly reduced from the unfiltered values. The noise of the output supply was originally –23.07 dBm, and the filters reduce this down to –51.6 dBm. The resulting RMS voltage is about 588 μV. This is still extremely low for the supply bus to the other boards of the instrument.

The efficiency is reduced, though, by utilizing these filters. The efficiency of the DC/DC converters gets reduced to about 70% with the filters. The expected efficiency without the filters was 83%; however, the decision was made to be slightly less than ideal in efficiency and have more ripple rejection. The efficiency is still greater than the efficiency of a linear regulator. For a +28-V unregulated supply bus, the efficiency of a linear regulator would be about 43%. The DC/DC converter with the filters is 1.5 times more efficient than a linear regulator.

The last section to test is the high voltage DC/DC converter. All parts are populated and the output voltage is measured. The expected voltage was within the range of error of the Zener

diode. The measured output was 151-V open circuit. Testing is done for the simulated current case as well; therefore, the lowest calibration resistance resistor is used to simulate this current. The current simulated was about 15 μA with the 10 MΩ resistor. The output of the DC/DC converter remained at about 150 V.

6.2 Environmental Testing

After the functionality of the electronics has been tested, the electronics needs to be tested in a relevant environment. For this test, the boards are all interfaced together in the appropriate circuit boxes. Before this test, the control and processing board and the power regulation board need to be conformal coated. The conformal coat used is the Dow Corning 1-2577. The electrometer and calibration board are not coated due to the possibility of leakage currents with the conformal coating. Once the conformal coating has set on these two boards, the electronics are tested in a relevant environment. A vacuum chamber with a thermo-cycle is used for this part of the test. The worst case cold and worst case hot scenarios are tested as well as cycling between the thermal extrema.

The pressure of the vacuum chamber follows the minimum expected pressure during flight. The minimum pressure is found by using the ideal gas law (or equation of state)

$$P = nkT,$$

where P is the pressure in Pascal, n is the neutral density, k is the Boltzmann constant, and T is the neutral temperature. The neutral density is used, because the density of the neutral particles is much greater than the plasma density. Figure 6.14 illustrates the pressure profile as a function of altitude. The minimum pressure exists at the highest altitude, as was to be expected. The vacuum chamber has to be capable of handling these types of pressures.

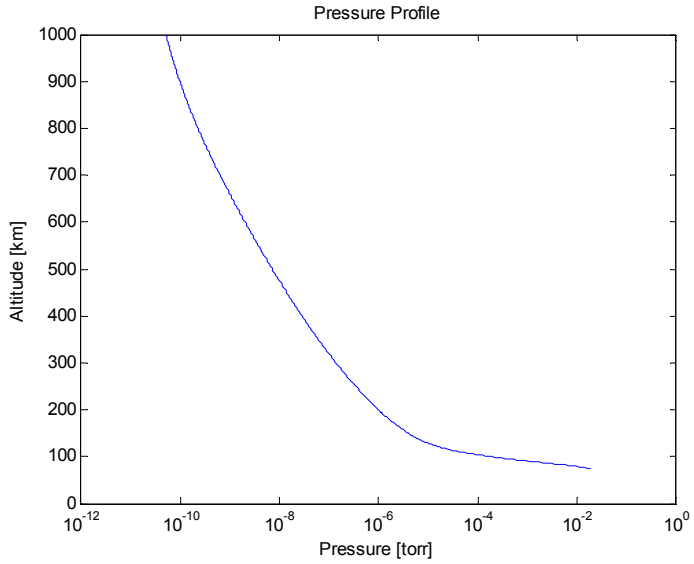

Figure 6.14 - Pressure profile as a function of altitude.

The temperature changes experienced during a mission are due to exposure to the Sun, solar reflection due to Earth albedo, black body radiation from the Earth, and eclipse by the Earth. The spacecraft thermal design techniques should keep the instrument within the thermal envelope of operation regardless of the previous stimuli. Table 6.3 lists the instrument storage temperature and operating temperature with the associated margins. The storage and operating

temperatures reflect the minimum range of all the components on the board. For the maximum device rated operating temperature and the storage temperature, the crystal has the smallest range. The specified operating temperature range is 0 °C to 70 °C, and the specified storage temperature range is –40 °C to +85 °C. A margin of 10% is set for the operating temperature, and a margin of 15% is set for the storage temperature for the instrument.

Table 6.3 - Instrument Temperature Range

	Range [°C]	Margin
Operating Temperature	7 to 63	10%
Storage Temperature	–21.25 to 66.25	15%

6.3 Plasma Environment Testing

The ideal plasma environment test for the instrument is to test aboard a sounding rocket flight; however, this may be an expensive route to just test a Langmuir probe instrument. A less expensive method is to test in a vacuum chamber with a low energy plasma source. The probe is positioned such that the sheath developed is entirely immersed within the bulk plasma. The return current for the probe also needs to be established. The electronic boxes need to have an electrical connection to the walls and remain grounded. The density and temperature of the plasma needs to follow the profile of the expected ionospheric plasma. The extreme cases as well as a typical case are to be tested.

7 Conclusions

This Langmuir probe instrument meets the requirements to operate in the space environment. Careful consideration in the design of each element is necessary for successful operation. For the probe design, the photoelectric effect, surface patchiness, chemical interactions, electric field fringing, and the geomagnetic field all need to be taken into account. To remain in the orbital-motion-limited regime, the probe has to have a radius less than a Debye length. Lastly, for the probe, surface contamination mitigation is a key issue for the proper interpretation of the plasma environment. Necessary precautions need to be taken in order for the probe surface to be clean. The probe clean methods include alcohol cleaning before flight, removal of probe until flight, and high voltage bias.

The electrometer is very susceptible to electromagnetic interference. The electrometer needs to be in its own enclosed box, and if the calibration board is used, this board is to be placed in the same box. All inputs and outputs to this box require bolt-in filters. The DC supply voltages need to be clean as well with the smallest ripple attainable. Shielding of the electrometer input for all interfaces eliminates any crosstalk.

In providing the probe with a swept bias, the bias is an upramp sweep, has two resting periods at the extrema, and should not have a very large range. With surface contamination, the probe provides valid ion density measurements. The upramp sweep allows electron temperature measurements still to be valid. The two resting periods at the extrema provide constant bias regions for ion density and electron density measurements. The sweep range is small in order for the ground reference of the payload not to change.

For the MC9S12C32 microprocessor, the most efficient code is programmed in assembly. The flight software was first written in C; however, the compiler created extra unnecessary instructions in the assembly machine code that slowed the program flow. The software functions were so slow that the necessary processes were not completed between timer interrupts. The data sampling rate is limited by the communication protocol. The RS-232/422 protocol has a maximum baud rate of 115200 bps, which allows a maximum sampling rate of 1040 samples per second for a two probe system. For faster sampling rates, other protocols should be used.

There are three spacecraft constraints mentioned in the design section. For the cylindrical probe design given, the probe axis is required to be orthogonal to the velocity vector of the spacecraft. There is a minimum probe surface area to spacecraft surface area ratio of 1:100. The minimum spacecraft surface area keeps the spacecraft from charging and the ground reference from changing. Lastly, there should not be any exposed voltages on the spacecraft. This may also lead to spacecraft charging. If the spacecraft charges to voltages greater than the sweep range, then the instrument can only function in the ion saturation region.

In conclusion, the Langmuir probe instrument designed and tested in this thesis can be used for sounding rocket missions and low earth orbit satellite missions. The design has been kept as simple as possible to keep the cost low, while performing all the necessary processes to meet the requirements. This instrument in combination with other science instruments may solve unknown features of ionophseric science yet to be determined.

REFERENCES

Abracon Corporation, "Quartz Crystals," Application Notes, Rancho Santa Margarita, CA, 2005.

Allen, J. E., R. L. F. Boyd, and P. Reynolds, "The Collection of Positive Ions by a Probe Immersed in a Plasma," *Proceedings of the Physical Society, Section B*, Vol. 70, pp. 297–304, 1957.

Almy, Tom, Designing with Microcontrollers – The 68HCS12, 2004.

Amatucci, W. E., M. E. Koepke, T. E. Sheridan, M. J. Alport, and J. J. Carroll, "Self-Cleaning Langmuir Probe," *Review of Scientific Instruments*, Vol. 64, 1993.

Ang, L. K., "Simple Derivation of Quantum Scaling in Child–Langmuir Law," *IEEE Transactions on Plasma Science*, pp. 410-412, 2004.

Balanis, Constantine A., Advanced Engineering Electromagnetics, Wiley, John & Sons, Inc., Hoboken, NJ, 1989.

Balitza, Dieter K., *International Reference Ionosphere*, NASA Goddard Space Flight Center, Greenbelt, Maryland, Version IRI-2007, [http://omniweb.gsfc. nasa.gov/vitmo/iri_vitmo.html], accessed on 02/16/2009.

Benilov, Mikhail S., "Boundary Conditions for the Child–Langmuir Sheath Model," *IEEE Transactions on Plasma Science*, Vol. 28, pp. 2207–2213, 2000.

Benilov, Mikhail S., "Method of Matched Asymptotic Expansions Versus Intuitive Approaches: Calculation of Space-Charge Sheaths," *IEEE Transactions on Plasma Science*, Vol. 31, pp. 678–690, 2003.

Bettinger, Richard T. and Evan H. Walker, "Relationship for Plasma Sheaths about Langmuir Probes," *The Physics of Fluids*, Vol. 8, pp. 748–751, 1965.

Brace, L., "Langmuir Probe Measurements in the Ionosphere," in Measurement Techniques in Space Plasmas: Particles, American Geophysical Union, Washington, DC, 1998.

Chen, Francis F., Introduction to Plasma Physics and Controlled Fusion, Spring Science and Business Media, LLC, New York, NY, 2nd Edition, 2006.

Conroy, L., 18th ESA Symposium on European Rocket and Balloon Programmes and Related Research. ESA Communication Production Office, ESTEC, Noordwijk, The Netherlands, 2007.

Cully, C. M., R. E. Ergun, and A. I. Eriksson, "Electrostatic Structure around Spacecraft in Tenuous Plasmas," *Journal of Geophysical Research*, Vol. 112, 2007.

Escobar, A. C., S. G. Bilén, and C. R. Philbrick, "Preliminary Langmuir Probe Analysis from ESPRIT," 18th ESA symposium on European Rocket and Balloon Programmes and Related Research, ESA Communication Production Office, ESTEC, Noordwijk, The Netherlands, 2007.

Freescale Semiconductor, "MC9S12C Family Reference Manual," Freescale Semiconductor Literature Distribution Center, Denver, CO, Ver. 1.23, 2007.

Friedrich, M., and K. M. Tokar, "An Empirical Model of the Nonauroral D Region," Radio Science, Vol. 27, pp. 945, 1992.

Garrett, Henry B. and Albert C. Whittlesey, "Spacecraft Charging, An Update," *IEEE Transactions on Plasma Science*, Vol. 28, 2000.

Goodall, C. V. and D. Smith, "A Comparison of the Methods of Determining Electron Densities in Afterglow Plasmas from Langmuir Probe Characteristics," *Plasma Physics*, Vol. 10, pp. 249–261, 1968.

Hedin, A. E., *Mass Spectrometer Incoherent Scatter Model*, NASA Goddard Space Flight Center, Greenbelt, Maryland, Version MSIS-E-90, [http://omniweb. gsfc.nasa.gov/vitmo/msis_vitmo.html], accessed on 02/16/2009.

Holback, B., Å. Jacksén, L. Åhlén, S. Jansson, A. Eriksson, J. Wahlund, T. Carozzi, and J. Bergman, "LINDA – The Astrid-2 Langmuir Probe Instrument," *Annales Geophysicae*, Vol. 19, pp. 601–610, 2001.

Horowitz, Paul and Winfield Hill, The Art of Electronics, Cambridge University Press, Cambridge, United Kingdom, 2nd Edition, 1989.

Hunsucker, R. D. and J. K. Hargreaves, The High-Latitude Ionosphere and its Effects on Radio Propagation, Cambridge University Press, Cambridge, United Kingdom, 2003.

Johnson, R. M. and T. L. Killeen, The Upper Mesophere and Lower Thermosphere: A Review of Experiment and Theory, American Geophysical Union, Washington, DC, 1995.

Jursa, Adolph S., Handbook of Geophysics and Space Environment, Air Force Geophysics Laboratory, US Air Force, National Technical Information Service, Springfield, Virginia, 1985.

Langmuir, Irving, "The Effect of Space Charge and Residual Gases on Thermionic Currents in High Vacuum," *Physical Review*, Vol. 2, pp. 450–486, 1913.

Langmuir, Irving, "The Interaction of Electron and Positive Ion Space Charges in Cathode Sheaths," *Physical Review*, Vol. 33, pp. 954–989, 1929.

Langmuir, Irving and Katherine Blodgett, "Currents Limited by Space Charge between Coaxial Cylinders," *Physical Review*, Vol. 22, pp. 347–356, 1923.

Langmuir, Irving and Katherine Blodgett, "Currents Limited by Space Charge between Concentric Spheres," *Physical Review*, Vol. 24, pp. 49–59, 1924.

Lieberman, Michael A. and Allan J. Lichtenberg, Principles of Plasma Discharges and Materials Processing, John Wiley & Sons, Inc., Hoboken, N.J., 2nd Edition, 2005.

Macmillan, Susan and Stefan Maus, *International Geomagnetic Reference Ionosphere*, NASA Goddard Space Flight Center, Greenbelt, Maryland, Version IGRF-10, [http:// omniweb.gsfc.nasa.gov/vitmo/igrf_vitmo.html], accessed on 02/16/2009.

Magnus, F. and J. Gudmundsson, "Digital Smoothing of the Langmuir Probe I-V Characteristic." *Review of Scientific Instruments*, Vol. 79, 2008.

Malhotra, Akshay, John D. Matthews, and Julio Urbina, "Effect of Meteor Ionization on Sporadic-E Observed at Jicamarca," *Geophysical Research Letters*, Vol. 35, L15106, doi:10.1029/2008GL034661, 2008.

Mott–Smith, H. M. and I. Langmuir, "The Theory of Collectors in Gaseous Discharges," *Physical Review*, Vol. 28, pp. 727–763, 1926.

Neamen, Donald A., Electronic Circuit Analysis and Design, McGraw–Hill Companies, Inc., New York, NY, 2nd Edition, 2001.

Oksuz, L., "Analytical Solution of Space Charge Limited Current for Spherical and Cylindrical Objects," *Applied Physics Letters*, Vol. 88, 2006.

Pfaff, Robert F., Joseph E. Borovsky, and David T. Young, Measurement Techniques in Space Plasmas: Fields, American Geophysical Union, Washington, DC, 1998.

Pfaff, Robert F., Joseph E. Borovsky, and David T. Young, Measurement Techniques in Space Plasmas: Particles, American Geophysical Union, Washington, DC, 1998.

Piel, A., M. Hirt, and C. Steigies, "Plasma Diagnostics with Langmuir Probes in the Equatorial Ionosphere: I. The Influence of Surface Contamination," *Journal of Physics D: Applied Physics*, Vol. 34, 2001.

Riemann, K. U., "The Bohm Criterion and Sheath Formation," *Journal of Physics D: Applied Physics*, Vol. 24, pp. 493–518, 1991.

Rutherford, J. A. and D. A. Vroom, "The Reaction of Atomic Oxygen with Several Atmospheric Ions," *The Journal of Chemical Physics*, Vol. 61, 1974.

Schunk, Robert W. and Andrew F. Nagy, Ionospheres: Physics, Plasma Physics, and Chemistry, Cambridge University Press, Cambridge, United Kingdom, 2004.

Scott, Allan W., Cooling of Electronic Equipment, Wiley, John & Sons, Inc., Hoboken, NJ, 1974.

Sedra, Adel S. and Kenneth C. Smith, Microelectronic Circuits, Oxford University Press, Inc., New York, NY, 4th Edition, 1998.

Space Weather Prediction Center, "Solar Cycle 24 Sunspot Number Prediction," National Oceanic and Atmospheric Administration, U.S. Department of Commerce, [http://www.swpc.noaa.gov/SolarCycle/], accessed on 02/16/2009.

Sutherland, Orson, Adrian Ankiewicz, and Rod Boswell, "Generalization of the Langmuir–Blodgett Laws for a Nonzero Potential Gradient," *Physics of Plasmas*, Vol. 12, 2005.

Swenson, Charles M., Don Thompson, and Chad Fish, "The Floating Potential Measurement Unit," *American Institute of Aeronautics and Astronautics Paper*, 41st Aerospace Sciences Meeting and Exhibit, 2003.

Tascione, Thomas F., Introduction to the Space Environment, Krieger Publishing Company, Malabar, FL, 2nd Edition, 1994.

Tribble, Alan C., The Space Environment, Princeton University Press, Princeton, NJ, 2nd Edition, 2003.

Violette, J. L., D. R. White, and M. F. Violette, Electromagnetic Compatibility Handbook, Van Nostrand Reinhold Company, Inc., New York, NY, 1987.

Wallace, John M. and Peter V. Hobbs, Atmospheric Science, Elsevier Inc., Oxford, United Kingdom, 2nd Edition, 2006.

Wang, Shiang–Bau and Amy Wendt, "Sheath Thickness Evaluation for Collisionless or Weakly Collisional Bounded Plasmas," *IEEE Transactions on Plasma Science*, Vol. 27, pp. 1358–1365, 1999.

APPENDIX: FLIGHT SOFTWARE

The flight software was first written in C, and then in assembly. The reason for the change was the C compiler created extra instructions in assembly that were not necessary, which required extra clock cycles to complete the same functions. Therefore, the assembly code was written in order to make the program flow more efficient. Below is an example of the code for a two probe system with probe one that utilizes the adaptive swept bias mode, and probe two utilizes the fixed biased mode. The adaptive swept bias is swept –5-V to +5-V for the acquisition sweep then ±5 V around the floating potential, and the fixed biased voltage is set at +5-V. The communication baud rate is set at 115200 bps, and the sampling rate is set at 1040 samples / second per probe. Each sample follows the compressed data format explained in the software chapter (Chapter 5).

```
;*************************************************************
;* File:    LP_program                                       *
;*                                                           *
;* Purpose:  To provide a program to control the probe bias,*
;*           data sampling, communications, and mission ops *
;* Created by:     Adam Escobar                              *
;* Revision History:    (mm/dd/yy)                           *
;*      03/24/09     Created file                           *
;*************************************************************

    XDEF          Entry
    ABSENTRY      Entry

    INCLUDE 'mc9s12c32.inc'

;Setup Interrupt Vectors to Interrupt Service Routines
    ORG $FFFE
    FDB Entry
    ORG $FFEE
    FDB OC0ISR
    ORG $FFD6
    FDB SCIISR

;*************************************************************
        ORG $800
;SCI Variables
BAUD          RMB   1
OUTINDEX      RMB   1
OUTLENGTH     RMB   1
OUTBUFF       DS   25
SYNC_COUNT    RMB   1
SYNC1         RMB   1
SYNC2         RMB   1
COMMAND       RMB   1
XCOUNT        RMB   2
;Samping Rate
SAMP          RMB   2
;Data Flags Byte
;   B0 = main data flag
;   B1 = Turn ON Latch
DATAFLAG      RMB   1
```

```
;Timing Variables
TIME_INT      RMB   2
;Probe Bias Variables
BIASFLAG      RMB   1
BIAS_DATA1    RMB   2
P1_BIAS_START RMB   2
P1_BIAS_END   RMB   2
BIAS_DATA2    RMB   2
BIAS_COUNT    RMB   2
COUNT1        RMB   2
COUNT2        RMB   2
COUNT3        RMB   2
STEPSIZE      RMB   2
;ATD Variables
AVG           RMB   2
CHANNEL       RMB   1
REFINPUT1     RMB   2
REFINPUT2     RMB   2
FULLINPUT1    RMB   2
FULLINPUT2    RMB   2
WININDEX1     RMB   1
WININPUT1     RMB   2
WININDEX2     RMB   1
WININPUT2     RMB   2
;Data Processing Variables
INDEXOLD      RMB   1
FLOAT_POT     RMB   2
POS_FPOT      RMB   2
NEG_FPOT      RMB   2
;Data Compression Variables
BYTE1         RMB   1
BYTE2         RMB   1
BYTE3         RMB   1

;*********************************************************
       ORG $4000
Entry:
       LDS #$0900        ;Initialize Stack Pointer

           ;Initialize all Ports and Modules
           BSR   INIT

           ;Enable Interrupts
                  CLI

       ;Electrometer Calibration
       JSR   ELECT_CAL

       ;Send Housekeeping
       JSR   HKEEPING

       ;Send Start Messege
       CLRA
       CLRB
       LDAB  SYNC1
       LDX   #OUTBUFF
       STAB  X
```

```
       INX
       LDAB  SYNC2
       STAB  X
       INX
       MOVB  #$59, X                ;'Y'
       INX
       MOVB  #$41, X      ;'A'
       INX
       MOVB  #$59, X      ;'Y'
       LDAA  #$05
       STAA  OUTLENGTH
       BSET  SCICR2, #$80

       BRA   MAINLOOP

       ;Go to DATA_COLL Subroutine
DATJMP JSR   DATA_COLL
       BRA   MAINLOOP

       ;Go to COMMAND_CHECK Subroutine
COMJMP JSR   COMMAND_CHECK
       BRA   MAINLOOP

MAINLOOP
       ;Check if DATAFLAG is set
       BRSET DATAFLAG, #%00000001, DATJMP

       ;Check for Commands
       LDAA  COMMAND
       CMPA  #$00
       BNE  COMJMP

       BRA   MAINLOOP

END
;***********************************************************

;****************************
;Subroutines
;****************************
;Initialize all Ports and Modules
INIT   ;Store Initial Values for Variables
       CLRA
       CLRB
       ;SCI Baud Rate
       LDAA  #$07
       STAA  BAUD          ;Set baud rate to 115200 kbps
       LDAA  #$00
       STAA  OUTINDEX
       STAA  OUTLENGTH
       STAA  SYNC_COUNT
       STAA  COMMAND
       LDAA  #$4C
       STAA  SYNC1         ;Set sync bytes as 'L' and 'P'
       LDAA  #$50
       STAA  SYNC2
       ;Sampling Rate
```

```
LDD   #$0410
STD   SAMP          ;Samping Rate = 1040 samples/sec
;Time Interrupt Number of Counts
LDD   #$2EF3
STD   TIME_INT      ;TIME_INT = 12.5e6 / SAMP
;Set the Data Flag
CLRA
STAA  DATAFLAG
STAA  BIASFLAG
;Probe Bias Variables
LDD   #$031E
STD   P1_BIAS_START ;Set start of probe bias to be -5 V
STD   BIAS_DATA1
LDD   #$0CE2
STD   P1_BIAS_END   ;Set end of probe bias to be +5-V
STD   BIAS_DATA2    ;Set probe bias 2 to be +5-V
LDD   #$0000
STD   BIAS_COUNT    ;Set count of samples/steps to 0
;Find Number of Steps with Respect to Sampling Rate
CLRA
CLRB
XGDX
LDD   SAMP
LDX   #$000A
IDIV                                          ;Divide by 10
XGDX
STD   COUNT1        ;# of steps for first 10% low section
CLRA
CLRB
XGDX
LDD   SAMP
LSLD
LSLD
LSLD                                          ;Multiply by 8
LDX   #$000A
IDIV                                          ;Divide by 10
CLRA
CLRB
LDD   COUNT1
LEAX  D,X
XGDX
STD   COUNT2        ;# of steps for 80% linear section + COUNT1
LDD   SAMP
STD   COUNT3        ;# of steps = SAMP
;Step Size Calculation
LDD   P1_BIAS_END
SUBD  P1_BIAS_START
XGDY
LDD   SAMP
LSLD
LSLD
LSLD                                          ;Multiply by 8
LDX   #$000A
IDIV                                          ;Divide by 10
XGDY
IDIV
XGDX
```

```
       STD   STEPSIZE
       ;Data Processing Variables
       LDD   #$0000
       STD   FLOAT_POT
       STD   POS_FPOT
       STD   NEG_FPOT

       ;Initialize the SCI module
       MOVB  #$00, SCIBDH
           LDAA  BAUD
           STAA  SCIBDL
           MOVB  #$00, SCICR1     ;8-N-1
           MOVB  #$2C, SCICR2     ;Enable RX interrupt, TX pin, and RX pin
           ;Initialize the SPI module
           MOVB  #$54, SPICR1      ;SPI enable, Master, SCK idle low, falling
edge sample, MSB first
           MOVB  #$09, SPICR2     ;Turn off Slave input
           MOVB  #$00, SPIBR      ;Baud rate = 6.25 MHz
           ;Initialize the ATD module
       MOVB  #$80, ATDCTL2    ;Normal ATD functions
       MOVB  #$20, ATDCTL3    ;Sets 4 conversions in 1 sequence
       MOVB   #$23,  ATDCTL4       ;10-bit  resolution,  4  clock  periods  per
sequence, 1.5625 MHz clock
           ;Initialize GPIO
           MOVB  #$FF, DDRT       ;All port T pins to output
           MOVB  #$00, PTT        ;Sets all port T outputs to low
           BSET  DDRB, #%00010000 ;PB4 set to output
           BCLR  PORTB, #%00010000;PB4 set low
           BCLR  DDRE, #$01       ;Port E0 is set as input
           BSET  DDRA, #$01       ;Port A0 is set as output
           BCLR  PORTA, #$00      ;PA0 set low
           BSET    DDRM, #%00001111 ;Set PTM0:3 as output
           BSET  PTM, #%00001100  ;Set PTM3 and PTM2 as high (For SPI)
           BCLR  PTM, #%00000011  ;Set PTM1 and PTM0 as low
           BSET  DDRP, #%00100000 ;PP5 is set as output
           BCLR  PTP, #%00100000  ;PP5 is set high
           ;Initialize  output  compare  timer  (turn  OFF  for  probe  bias,
electrometer cal, and H.K.)
           BSET  TIOS, #%00000001   ;turn on output compare 0
           BSET  TSCR1, #%10000000  ;timer system enable
           BSET  TIE, #%00000001    ;enable OC0 interrupts
           MOVB  #$00, TSCR2        ;Pre-scaler set to e-clock/1
           BSET  TFLG1, #%00000001  ;reset the initial flag
           BSET  TFLG2, #%10000000  ;clear interrupt flag
           LDD   #$0000                                    ;Initial value
           STD   TC0                                            ;in      the
TOC0 register
           RTS

;*******************************************************
SAMP_PORT
       LDAA  #$80
       ADDA  CHANNEL            ;Set channel to sample
       STAA  ATDCTL5
       CLRA
       CLRB
       BRCLR ATDSTAT0, #$80, *  ;Wait for sequence to complete
```

```
        CLRA
        CLRB
        LDD   ATDDR0
        ADDD  ATDDR1
        ADDD  ATDDR2
        ADDD  ATDDR3
        LSRD
        LSRD                    ;Average the four measurements
        ADCB  #$00
        ADCA  #$00              ;Round the result
        STD   AVG
        RTS

;*******************************************************
DAC_OUT
        LDAA  BIASFLAG
        CMPA  #$02
        BEQ   PROBE2
PROBE1  BCLR  PTM, #%00001000  ;Set sync 1 low
        NOP
        NOP
        NOP
        NOP
        NOP
        NOP
        NOP
        NOP
        LDD   BIAS_DATA1
        LSLD
        LSLD
        BRCLR SPISR, #$20, *   ;Make sure SPI buffer is cleared
        STAA  SPIDR            ;Send first byte
        BRCLR SPISR, #$20, *   ;Make sure SPI buffer is cleared
        STAB  SPIDR            ;Send second byte
        BRCLR SPISR, #$20, *   ;Make sure SPI buffer is cleared
        NOP
        NOP
        NOP
        NOP
        NOP
        NOP
        NOP
        NOP
        NOP
        BSET  PTM, #%00001000  ;Set syncy 1 high
        BRA   DACEND
PROBE2  BCLR  PTM, #%00000100  ;Set sync 2 low
        NOP
        NOP
        NOP
        NOP
        NOP
        NOP
        NOP
        NOP
        LDD   BIAS_DATA2
```

```
       LSLD
       LSLD
       BRCLR SPISR, #$20, *   ;Make sure SPI buffer is cleared
       STAA  SPIDR            ;Send first byte
       BRCLR SPISR, #$20, *   ;Make sure SPI buffer is cleared
       STAB  SPIDR            ;Send second byte
       BRCLR SPISR, #$20, *   ;Make sure SPI buffer is cleared
       NOP
       NOP
       NOP
       NOP
       NOP
       NOP
       NOP
       NOP
       NOP
       BSET  PTM, #%00000100  ;Set syncy 2 high
DACEND RTS

;*******************************************************
WINDOWING
       LDAA  BIASFLAG
       CMPA  #$02
       LBEQ  WP2
WP1    LDD   FULLINPUT1
       CPD   #$006B           ;Compare to 107 - out of windowing range
       LBLE  FULL1
       CPD   #$0200           ;Compare to 512 - in ion sat. range
       BLE   ION1
       CPD   #$02F5           ;Compare to 757 - in e- ret range
       BLE   E_RET1
       CPD   #$038A           ;Compare to 906 - in e- ret/e- sat range
       BLE   E_RS1
       BRA   E_SAT1           ;Else branch to electron saturation region
ION1   BCLR  PTT, #%00010000
       BCLR  PTT, #%00100000
       LDAA  #$01
       STAA  WININDEX1
       LDAA  #$02
       STAA  CHANNEL
       JSR   SAMP_PORT
       LDD   AVG
       STD   WININPUT1
       LBRA  WINEND
E_RET1 BSET  PTT, #%00010000
       BCLR  PTT, #%00100000
       LDAA  #$02
       STAA  WININDEX1
       LDAA  #$02
       STAA  CHANNEL
       JSR   SAMP_PORT
       LDD   AVG
       STD   WININPUT1
       LBRA  WINEND
E_RS1  BCLR  PTT, #%00010000
       BSET  PTT, #%00100000
```

```
        LDAA  #$03
        STAA  WININDEX1
        LDAA  #$02
        STAA  CHANNEL
        JSR   SAMP_PORT
        LDD   AVG
        STD   WININPUT1
        LBRA  WINEND
E_SAT1  BSET  PTT, #%00010000
        BSET  PTT, #%00100000
        LDAA  #$04
        STAA  WININDEX1
        LDAA  #$02
        STAA  CHANNEL
        JSR   SAMP_PORT
        LDD   AVG
        STD   WININPUT1
        LBRA  WINEND
FULL1   STD   WININPUT1
        LDAA  #$05
        STAA  WININDEX1
        LBRA  WINEND
WP2     LDD   FULLINPUT2
        CPD   #$006B            ;Compare to 107 - out of windowing range
        LBLE  FULL2
        CPD   #$0200            ;Compare to 512 - in ion sat. range
        BLE   ION2
        CPD   #$02F5            ;Compare to 757 - in e- ret range
        BLE   E_RET2
        CPD   #$038A            ;Compare to 906 - in e- ret/e- sat range
        BLE   E_RS2
        BRA   E_SAT2            ;Else branch to electron saturation region
ION2    BCLR  PTT, #%01000000
        BCLR  PTT, #%10000000
        LDAA  #$01
        STAA  WININDEX2
        LDAA  #$05
        STAA  CHANNEL
        JSR   SAMP_PORT
        LDD   AVG
        STD   WININPUT2
        BRA   WINEND
E_RET2  BSET  PTT, #%01000000
        BCLR  PTT, #%10000000
        LDAA  #$02
        STAA  WININDEX2
        LDAA  #$05
        STAA  CHANNEL
        JSR   SAMP_PORT
        LDD   AVG
        STD   WININPUT2
        BRA   WINEND
E_RS2   BSET  PTT, #%01000000       ;Switched to BSET due to hardware error
        BSET  PTT, #%10000000
        LDAA  #$03
        STAA  WININDEX2
        LDAA  #$05
```

```
        STAA  CHANNEL
        JSR   SAMP_PORT
        LDD   AVG
        STD   WININPUT2
        BRA   WINEND
E_SAT2  BCLR  PTT, #%01000000    ;Switched to BCLR due to hardware error
        BSET  PTT, #%10000000
        LDAA  #$04
        STAA  WININDEX2
        LDAA  #$05
        STAA  CHANNEL
        JSR   SAMP_PORT
        LDD   AVG
        STD   WININPUT2
        BRA   WINEND
FULL2   STD   WININPUT2
        LDAA  #$05
        STAA  WININDEX2
        BRA   WINEND
WINEND  RTS

;*********************************************************
FPOT_CHK
        LDAA  INDEXOLD
        CMPA  #$01
        BNE   FP_END
        LDAA  WININDEX1
        CMPA  #$02
        BNE   FP_END
        LDD   BIAS_DATA1
        STD   FLOAT_POT
        CPD   #$0800
        BLE   N_FPOT
        SUBD  #$0800
        STD   POS_FPOT
        LDD   #$0000
        STD   NEG_FPOT
        BRA   FP_END
N_FPOT  LDD   #$0800
        SUBD  FLOAT_POT
        STD   NEG_FPOT
        LDD   #$0000
        STD   POS_FPOT
FP_END  RTS

;*********************************************************
DATA_COLL
        LDAA  DATAFLAG
        ANDA  #%00000010
        CMPA  #%00000010       ;Determine if first data collection
        BNE   P_BIAS
P_DATA  LDAA  #$00
        STAA  CHANNEL
        JSR   SAMP_PORT
        LDD   AVG
        STD   REFINPUT1
        LDAA  #$01
```

```
        STAA  CHANNEL
        JSR   SAMP_PORT
        LDD   AVG
        STD   FULLINPUT1
        LDAA  #$01
        STAA  BIASFLAG
        JSR   WINDOWING
        JSR   FPOT_CHK
        LDAA  WININDEX1
        STAA  INDEXOLD
        LDAA  #$03
        STAA  CHANNEL
        JSR   SAMP_PORT
        LDD   AVG
        STD   REFINPUT2
        LDAA  #$04
        STAA  CHANNEL
        JSR   SAMP_PORT
        LDD   AVG
        STD   FULLINPUT2
        LDAA  #$02
        STAA  BIASFLAG
        JSR   WINDOWING
P_BIAS  LDD   BIAS_COUNT
        CPD   COUNT1
        BLE   BIAS1
        CPD   COUNT2
        BLE   BIAS2
        CPD   COUNT3
        BLT   BIAS3A
        BEQ   BIAS3B
BIAS1   LDAA  #$01
        STAA  BIASFLAG
        LDD   FLOAT_POT
        CPD   #$0800
        BLE   NPADD1
        LDD   P1_BIAS_START
        ADDD  POS_FPOT
        STD   BIAS_DATA1
        BRA   B1_OUT
NPADD1  LDD   P1_BIAS_START
        SUBD  NEG_FPOT
        STD   BIAS_DATA1
B1_OUT  JSR   DAC_OUT
        LDD   BIAS_COUNT
        ADDD  #$01
        STD   BIAS_COUNT
        BRA   D_END
BIAS2   LDAA  #$01
        STAA  BIASFLAG
        LDD   BIAS_DATA1
        ADDD  STEPSIZE
        STD   BIAS_DATA1
        JSR   DAC_OUT
        LDD   BIAS_COUNT
        ADDD  #$01
        STD   BIAS_COUNT
```

```
       CPD   COUNT2
       BNE   D_END
       LDD   BIAS_DATA1
       ADDD  STEPSIZE
       ADDD  #$0001
       STD   BIAS_DATA1
       BRA   D_END
BIAS3A LDAA  #$01
       STAA  BIASFLAG
       JSR   DAC_OUT
       LDD   BIAS_COUNT
       ADDD  #$01
       STD   BIAS_COUNT
       BRA   D_END
BIAS3B LDD   #$00
       STD   BIAS_COUNT
       LDAA  #$01
       STAA  BIASFLAG
       JSR   DAC_OUT
D_END  LDAA  #$02
       STAA  BIASFLAG
       JSR   DAC_OUT
       LDAA  DATAFLAG
       ANDA  #%00000010
       CMPA  #%00000010
       BNE   D_END2
       JSR   SEND_DAT
D_END2 BSET  DATAFLAG, #%00000010       ;Set first sweep bit
       BCLR  DATAFLAG, #%00000001
       RTS

;*******************************************************
;Data sent as 3 bytes per probe sample
;No SYNC bytes - only sync to first TURN ON
SEND_DAT
       ;Compress Probe 1 data
       LDD   REFINPUT1
       LSLD                                    ;Less  clock  cycles  to  use
LSLD
       LSLD             ;instead of LDY,EMUL, and XGDY
       LSLD
       LSLD
       LSLD
       LSLD
       STAA  BYTE1                ;BYTE1 is 8-bits MSBs of REFINPUT1
       STAB  BYTE2                ;Start  BYTE2  with  2-bits  of  LSBs  of
REFINPUT1
       LDAA  WININDEX1
       LSLA
       LSLA
       ADDA  BYTE2
       STAA  BYTE2                ;Add BYTE2 with WININDEX1
       LDD   WININPUT1
       STAB  BYTE3
       ADDA  BYTE2
       STAA  BYTE2                ;BYTE2  with  WININDEX1  and  2-bits  of  MSB
of WININPUT1
```

```
       ;Place first 3 bytes into OUTBUFF
       CLRA
       LDAB  BYTE1
       LDX   #OUTBUFF
       STAB  X
       INX
       LDAB  BYTE2
       STAB  X
       INX
       LDAB  BYTE3
       STAB  X

       ;Compress Probe 2 data
       LDD   REFINPUT2
       LSLD
       LSLD
       LSLD
       LSLD
       LSLD
       LSLD
       STAA  BYTE1                 ;BYTE1 is 8-bits MSBs of REFINPUT2
       STAB  BYTE2                 ;Start  BYTE2  with  2-bits  of  LSBs  of
REFINPUT2
       LDAA  WININDEX2
       LSLA
       LSLA
       ADDA  BYTE2
       STAA  BYTE2                 ;Add BYTE2 with WININDEX2
       LDD   WININPUT2
       STAB  BYTE3
       ADDA  BYTE2
       STAA  BYTE2                 ;BYTE2  with  WININDEX2  and  2-bits  of  MSB
of WININPUT2

       ;Place last 3 bytes into OUTBUFF
       CLRA
       LDAB  BYTE1
       INX
       STAB  X
       INX
       LDAB  BYTE2
       STAB  X
       INX
       LDAB  BYTE3
       STAB  X

       ;Set length and TX interrupt
       LDAA  #$06
       STAA  OUTLENGTH
       BSET  SCICR2, #$80
       RTS

;*******************************************************
;Turn OFF timing interrupt and reset variables
TIME_OFF
       CLRA
```

```
       CLRB
       STAA  TSCR1
       STAA  TIOS
       STAA  TIE
       STD   TC0
       RTS

;*********************************************************
COMMAND_CHECK
       JSR   TIME_OFF
       BCLR  DATAFLAG, #%00000010     ;Clear first sweep flag
CCST   LDAA  COMMAND
       ANDA  #$41          ;AND to 'A' and compare
       CMPA  #$41
       BEQ   PC_JSR
       LDAA  COMMAND
       ANDA  #$42          ;AND to 'B' and compare
       CMPA  #$42
       BEQ   EC_JSR
       LDAA  COMMAND
       ANDA  #$43                      ;AND to 'C' and compare
       CMPA  #$43
       BEQ   HK_JSR
       BRA   CCEND
PC_JSR JSR   PCLEAN
       BRA   CCEND
EC_JSR JSR   ELECT_CAL
       BRA   CCEND2
HK_JSR JSR   HKEEPING
       BRA   CCEND2
CCEND  LDAA  COMMAND
       ANDA  #$44                      ;AND to 'D' and compare
       CMPA  #$44
       BNE   CCST
CCEND2 LDAA  #$00
       STAA  COMMAND
       JSR   INIT          ;Reinitialize
       RTS

;*********************************************************
PCLEAN CLRA
       CLRB
       BSET  PTP, #%00100000
PCLOOP LDAB  COMMAND
       ANDB  #$41
       CMPB  #$41
       BNE   PC_END
       BRA   PCLOOP
PC_END BCLR  PTP, #%00100000
       RTS

;*********************************************************
ELECT_CAL
       ;Electrometer 1 Calibration
       LDD   P1_BIAS_END
       STD   BIAS_DATA1        ;Set Electrometer to +5-V
       ;Place Sync words into outbuff
```

```
        CLRA
        CLRB
        LDAB  SYNC1
        LDX   #OUTBUFF
        STAB  X
        INX
        LDAB  SYNC2
        STAB  X
        INX
        STX   XCOUNT
        LDAA  #$02
        STAA  OUTLENGTH

E1      LDAA  #$00
        STAA  CHANNEL
        JSR   SAMP_PORT     ;Sample reference
        LDD   AVG
        STD   REFINPUT1
        ;Store Reference 1 into Outbuff
        LDX   XCOUNT
        LDD   REFINPUT1
        STAA  X
        INX
        STAB  X
        INX
        LDAA  OUTLENGTH
        ADDA  #$02
        STAA  OUTLENGTH
        STX   XCOUNT

        ;Switch Primary Relays
        ;Find data for Resistor 1 = 10 Mohm
        BSET  PORTA, #%00000001
        LDAA  #$01
        STAA  CHANNEL
        JSR   SAMP_PORT
        LDD   AVG
        STD   FULLINPUT1
        LDAA  #$01
        STAA  BIASFLAG
        JSR   WINDOWING
        JSR   ELECT_OUT1    ;Place Data into outbuff

        ;Find data for Resistor 2 = 100 Mohm
        BSET  PTT, #%00000010
        LDAA  #$01
        STAA  CHANNEL
        JSR   SAMP_PORT
        LDD   AVG
        STD   FULLINPUT1
        LDAA  #$01
        STAA  BIASFLAG
        JSR   WINDOWING
        JSR   ELECT_OUT1

        ;Find data for Resistor 3 = 1 Gohm
        BCLR  PTT, #%00000010
```

```
        BSET  PTT, #%00000001
        LDAA  #$01
        STAA  CHANNEL
        JSR   SAMP_PORT
        LDD   AVG
        STD   FULLINPUT1
        LDAA  #$01
        STAA  BIASFLAG
        JSR   WINDOWING
        JSR   ELECT_OUT1

        ;Find data for Resitor 4 = 10 Gohm
        BSET  PTT, #%00000010
        LDAA  #$01
        STAA  CHANNEL
        JSR   SAMP_PORT
        LDD   AVG
        STD   FULLINPUT1
        LDAA  #$01
        STAA  BIASFLAG
        JSR   WINDOWING
        JSR   ELECT_OUT1

        ;Reset Relays
        BCLR  PORTA, #%0000001
        BCLR  PTT, #%00000011

        ;Send Data Out
        BSET  SCICR2, #$80

        ;Check for -5 V Bias
        LDD   BIAS_DATA1
        CPD   P1_BIAS_START
        BNE   FLIP1
        BRA   E2_A
FLIP1   LDD   P1_BIAS_START
        STD   BIAS_DATA1
        LDX   #OUTBUFF
        STX   XCOUNT
        LBRA  E1

        ;Electrometer 2 Calibration
E2_A    LDD   P1_BIAS_END
        STD   BIAS_DATA2        ;Set Electrometer to +5-V

E2      LDAA  #$03
        STAA  CHANNEL
        JSR   SAMP_PORT     ;Sample reference
        LDD   AVG
        STD   REFINPUT2
        ;Store Reference 2 into Outbuff
        LDX   #OUTBUFF
        LDD   REFINPUT2
        STAA  X
        INX
        STAB  X
        INX
```

```
LDAA  OUTLENGTH
ADDA  #$02
STAA  OUTLENGTH
STX   XCOUNT

;Switch Primary Relays
;Find data for Resistor 1 = 10 Mohm
BSET  PORTB, #%00010000
LDAA  #$04
STAA  CHANNEL
JSR   SAMP_PORT
LDD   AVG
STD   FULLINPUT1
LDAA  #$02
STAA  BIASFLAG
JSR   WINDOWING
JSR   ELECT_OUT2    ;Place Data into outbuff

;Find data for Resistor 2 = 100 Mohm
BSET  PTT, #%00001000
LDAA  #$04
STAA  CHANNEL
JSR   SAMP_PORT
LDD   AVG
STD   FULLINPUT1
LDAA  #$02
STAA  BIASFLAG
JSR   WINDOWING
JSR   ELECT_OUT2

;Find data for Resistor 3 = 1 Gohm
BCLR  PTT, #%00001000
BSET  PTT, #%00000100
LDAA  #$04
STAA  CHANNEL
JSR   SAMP_PORT
LDD   AVG
STD   FULLINPUT1
LDAA  #$02
STAA  BIASFLAG
JSR   WINDOWING
JSR   ELECT_OUT2

;Find data for Resitor 4 = 10 Gohm
BSET  PTT, #%00001000
LDAA  #$04
STAA  CHANNEL
JSR   SAMP_PORT
LDD   AVG
STD   FULLINPUT1
LDAA  #$02
STAA  BIASFLAG
JSR   WINDOWING
JSR   ELECT_OUT2

;Reset Relays
BCLR  PORTB, #%00010000
```

```
       BCLR  PTT, #%00001100

       ;Send Data Out
       BSET  SCICR2, #$80

       ;Check for -5 V Bias
       LDD   BIAS_DATA2
       CPD   P1_BIAS_START
       BNE   FLIP2
       BRA   E_END
FLIP2  LDD   P1_BIAS_START
       STD   BIAS_DATA2
       LBRA  E2
E_END  RTS

ELECT_OUT1
       LDX   XCOUNT
       LDAA  WININDEX1
       STAA  X
       INX
       LDD   WININPUT1
       STAA  X
       INX
       STAB  X
       INX
       LDAA  OUTLENGTH
       ADDA  #$05
       STAA  OUTLENGTH
       STX   XCOUNT
       RTS

ELECT_OUT2
       LDX   XCOUNT
       LDAA  WININDEX2
       STAA  X
       INX
       LDD   WININPUT2
       STAA  X
       INX
       STAB  X
       INX
       LDAA  OUTLENGTH
       ADDA  #$05
       STAA  OUTLENGTH
       STX   XCOUNT
       RTS

;*******************************************************
HKEEPING
       ;Store Sync bytes into output buffer
       CLRA
       CLRB
       LDAB  SYNC1
       LDX   #OUTBUFF
       STAB  X
       INX
       LDAB  SYNC2
```

```
        STAB  X
        INX
        STX   XCOUNT
        LDAA  #$02
        STAA  OUTLENGTH

        ;Adjust Analog MUX to S1:  +5-V Bus
        BCLR  PTM, #%00000011
        LDAA  #$07
        STAA  CHANNEL
        JSR   SAMP_PORT
        LDD   AVG
        LDX   XCOUNT
        STAA  X
        INX
        STAB  X
        INX
        LDAA  OUTLENGTH
        ADDA  #$02
        STAA  OUTLENGTH
        STX   XCOUNT

        ;Adjust Analog Mux to S2:  Bus Current and +5-V Temp
        BSET  PTM, #%00000010
        BSR   HK_OUT

        ;Adjust Analog Mux to S3:  Bus Voltage and +12-V Bus
        BCLR  PTM, #%00000010
        BSET  PTM, #%00000001
        BSR   HK_OUT

        ;Adjust Analog Mux to S4:  HV_Voltage and -12 V Bus
        BSET  PTM, #%00000011
        BSR   HK_OUT

        ;Send Data out
        BSET  SCICR2, #$80
        RTS

HK_OUT  LDAA  #$06
        STAA  CHANNEL
        JSR   SAMP_PORT
        LDD   AVG
        LDX   XCOUNT
        STAA  X
        INX
        STAB  X
        INX
        LDAA  OUTLENGTH
        ADDA  #$02
        STAA  OUTLENGTH
        STX   XCOUNT
        LDAA  #$07
        STAA  CHANNEL
        JSR   SAMP_PORT
        LDD   AVG
        LDX   XCOUNT
```

```
       STAA  X
       INX
       STAB  X
       INX
       LDAA  OUTLENGTH
       ADDA  #$02
       STAA  OUTLENGTH
       STX   XCOUNT
       RTS

;*******************************************************
;****************************
;Interrupt Service Routines
;****************************
;Timing Interrupt Service Routine
OC0ISR BSET  DATAFLAG, #%00000001
       BSET  TFLG1, #%00000001  ;reset the interrupt flag
       LDD   TC0
       ADDD  TIME_INT           ;time interval = offset*pre-scaler/e-clock
       STD   TC0
       RTI

;*******************************************************
;SCI Interrupt Service Routine
SCIISR CLRA
       LDAA  SCISR1             ;SCI transmit check
       ANDA  #$80
       CMPA  #$80
       BNE   SCIRD
             LDAA  OUTLENGTH
             CMPA  OUTINDEX
       BEQ   CLRTX
       CLRA
       CLRB
       LDD   #OUTBUFF
       ADDD  OUTINDEX
       XGDX
       MOVB  X, SCIDRL          ;Send out data
       LDAA  OUTINDEX
       INCA
       STAA  OUTINDEX
       BRA   SCIEND
CLRTX  LDAA  #$00
       STAA  OUTLENGTH
       STAA  OUTINDEX
       BCLR  SCICR2, #$80
       BRA   SCIEND
SCIRD  LDAA  SCISR1             ;SCI receive check
       ANDA  #%00100000
       CMPA  #%00100000
       BNE   SCIEND
       LDAA  SYNC_COUNT
       CMPA  #$02
       BNE   SCICK2
       LDAA  SCIDRL
       STAA  COMMAND                                  ;Store Command byte
       LDAA  #$00
```

```
       STAA  SYNC_COUNT
       BRA   SCIEND
SCICK2 LDAA  SYNC_COUNT         ;Check for 'P'
       CMPA  #$01
       BNE   SCICK1
       LDAB  SCIDRL
       CMPB  SYNC2
       BNE   SCIEND
       INCA
       STAA  SYNC_COUNT
       BRA   SCIEND
SCICK1 LDAA  SCIDRL             ;Check for 'L'
       CMPA  SYNC1
       BNE   SCIEND
       LDAA  SYNC_COUNT
       INCA
       STAA  SYNC_COUNT
SCIEND RTI
;***************************
```